Evaluating precipitation simulations from a land-atmosphere coupling model

By

Yuqi Zhang
M.S., China University of Geosciences (Beijing), 2015
B.S., China University of Geosciences (Beijing), 2012

Submitted to the graduate degree program in Department of Civil, Environmental, and Architectural Engineering and the Graduate Faculty of the University of Kansas in partial fulfillment of the requirements for the degree of Doctor of Philosophy.

Chair: Joshua Roundy

Admin Husic

Bryan Young

Nathaniel Brunsell

Joseph Santanello

Date Defended: 17 May 2022

The dissertation committee for Yuqi Zhang certifies that this is the
approved version of the following dissertation:

Evaluating precipitation simulations from a land-atmosphere coupling model

Chair: Joshua Roundy

Date Approved: May 27, 2022

Abstract

Nowadays climate models are widely used for weather forecasting. With the increased computational capacity, the simulated resolution of climate models has been enhanced from tens of kilometers in Global Climate Models (GCMs) to less than 10 km in Regional Climate Models (RCMs). The increased resolution has the potential for improved model skill due to capturing more heterogeneity within the system. However, this potential increase in skill is not guaranteed and thus there is a need for further model evaluation studies to provide a better understanding of model configuration and corresponding performance, especially for resolutions in the grey zone (1-10 km grid resolution). Among all variables in climate model simulation, precipitation is one of the most important and also the most difficult variable to predict due to the complexity of land-atmosphere (L-A) interactions. To better understand how well precipitation is simulated and the role of L-A interaction in climate models simulations, three research studies are carried out using the NASA Unified Weather Research and Forecast (NU-WRF) model. First, the impact of model resolution (4 km, 12 km and 24 km) and the use of cumulus parameterization are evaluated in terms of the prediction of precipitation frequency, bias and the spatial patterns. Results shows the cumulus parameterization has more impact than increasing model resolution on precipitation forecast. At the 4 km resolution, the model without cumulus parametrization better captures the spatial patterns in the precipitation forecast. These findings are then used to select the optimal model configuration which is used in the remaining two studies. The second study identifies and evaluates the different drivers of precipitation during the 2018 warm season drought (May-Sep) in the Central Plain. Contributions of different precipitation drivers with and without the impact of Mesoscale Convective Systems (MCSs) and Low Level Jets (LLJs) are analyzed in order to understand the roles of local and non-local precipitation during drought evolution. The lack of MCSs is found to be the dominant driver during the drought, and the LLJ is found to have indirect weaker impact to precipitation with a lag time of up to two days. The last study then quantifies and analyzes the role of local soil moisture feedback during drought through an additional model run with switched initial soil moisture between a relatively wet and dry region to provide insights and understanding of L-A interactions. Results show a 2% change in lifted cloud fraction caused by a soil moisture change less than 0.05 m^3 m^{-3} and LLJ can enhance L-A interactions to promote precipitation formation. Overall, this study provides a comprehensive evaluation of the skill in precipitation forecast of the NU-WRF model and provides insights into the implication of MCS, LLJ, the L-A interaction during local and non-local influenced atmospheric environment and identified model deficiencies. Addressing these deficiencies could improve future precipitation forecasts in the Central Great Plains.

Acknowledgments

I would firstly thank my supervisor, Dr. Joshua Roundy, who gave me the chance to study at KU and provide continuous support during my 6-year PhD journey. Under his guidance, I not only learned academic knowledge but also gained better understanding of how to do research, how to deal with different problems and the importance of independent and critical thinking. As an international student, I really appreciate his patient communication and tolerance which helped me get through the difficult time of adapting to a new environment and culture. In addition, I am grateful for his financial support and providing me with the opportunity to work as a teaching assistant and gain teaching experience. Throughout my time at KU, he helped me realize the important qualities of a successful researcher, a student and teacher. All of these experiences have helped me achieve my career goals. I enjoyed working with him and the open communication atmosphere we had, and I hope we will have a chance to collaborate in the future.

I would also like to thank other people in my committee – Dr. Admin Husic, Dr. Bryan Young, Dr. Nathaniel Brunsell and Dr. Joseph Santanello, for reviewing my work with patience and for providing constructive comments. A special thanks to Dr. Joseph Santanello who helped build collaboration with Hydrological Sciences Laboratory of NASA Goddard Space Flight Center and providing support on the NU-WRF model and their CONUS simulation data used in this dissertation.

Last but most importantly, I would like to thank my family and friends who have given me strong spiritual support. Thanks to my parents who always respect my thoughts and try their best to support me. Thanks for their warning, guidance and suggestions when I got lost concerning my life and future. Thanks to my friends Dan Wang, Bingqian Jiang, Haiyun Zheng and Atefeh

Hosseini, who patiently listen to my worries and cheer me up and provide a release from pressure and anxiety and encourage me to overcome difficulties when I am depressed.

Table of Contents

List of Figures

List of Tables

Chapter 1: Introduction

Climate and weather directly influence human life and are important research topics especially in the 21st century due to increasing populations and global warming. Because of the increased greenhouse gas emissions induced by human activity, global warming has become a serious problem affecting the global water cycle. Both intensity and frequency of heavy precipitation have been found to increase under climate change over many land areas globally (Seneviratne et al. 2021) and drought may become less predictable over the western U.S due to increasing snowmelt in the future (Livneh and Badger 2020). The impact of climate change has increased the need to understand atmospheric dynamics and its interaction with the land and oceans to have better predictions which can be used by decision makers. However, due to the chaotic nature of atmosphere, weather forecast currently only provide skillful results about a week ahead and there is still large room to reduce uncertainties in model forecast (Li and Robertson 2015; Zhang et al. 2019). Compared to temperature, precipitation is less predictable in model simulations (Tian et al. 2017b). The current lower predictability of precipitation is one of the main drives of this study with the aim to evaluate precipitation simulation in a coupled land-atmosphere (L-A) model and identify deficiencies.

The model used in this study is the NASA-Unified Weather Research and Forecasting (NU-WRF, Peters-Lidard et al. 2015) model which is a revised framework based on NCAR Advanced Research WRF (ARW) model (Skamarock et al. 2008) with additional Goddard Chemistry Aerosols Radiation Transport model (GOCART), the Goddard Satellite Data Simulator Unit (G-SDSU) and a few NASA derived radiation and microphysics schemes. NU-WRF enables coupling with the Land Information System (LIS, Kumar et al., 2006) which has different land surface models enabling different representations of the land surface within WRF. The NU-WRF model is unique in that it has these additional functions. The NU-WRF model was first released in 2011, but there are limited studies using the NU-WRF model, which leaves a need for testing and understanding the model performance and its limitations. In this study, the Goddard microphysics scheme and radiation scheme are used, providing a unique opportunity for understanding the embedded physical mechanics as well as the limitations and deficiencies of the NU-WRF model in precipitation forecast in addition to other aspects (configurations) already present in the WRF model.

To have a comprehensive evaluation of the precipitation in the model, this study is separated into three studies. The first study explores and analyzes the impact of model resolution and the use of cumulus parameterization on precipitation predictions and identifies the optimal model configuration which will be used in the remaining studies (chapter 2). Next, the precipitation is then separated into 4 types considering the impact of Low Level Jet (LLJ) and Mesoscale Convective System (MCS). These different precipitation types are representative of local and non-local caused precipitation, and are analyzed within in the model to identify model deficiency in representing the different environments (chapter 3). This study is carried out over a drought period to analyze the role of different precipitation regimes and the role of soil moisture and its contribution to precipitation during drought development. Normally the L-A interactions are difficult to analyze due to the complexity of the atmospheric environment, but the separation of different precipitation types can help to tease out non-local impacts. This methodology is the basis of the last study which aims to understanding the role of L-A interactions in precipitation predictions in the model (chapter 4). The remaining sections in this chapter provide further background information needed to provide context and frame this study within the existing literature.

1.1 Model Configuration Impacts on Precipitation Forecast

With the increasing need to understand and simulate weather and climate at regional scales, downscaling Global Climate Models (GCMs) has become an important topic. Both types of downscaling methods: statistical downscaling and dynamic downscaling have their own advantages and drawbacks (Maraun et al. 2010). Based on the premise that there is an underlying relationship with predictor and predictand, statistical downscaling provides a way to predict unknown variables such as precipitation with relatively low computational demand. The downside to statistical downscaling is that it relies on the assumption that the observed statistical relationships will be the same in the future as it was in the past. On the contrary, dynamic downscaling is based on physical mechanism which simulates the interactions between the land and atmosphere and has the potential to change the relationship between the predictor and predictand based on changes in the modeling processes. Yet, dynamical downscaling is more computational and time-intensive which precludes it from use in many long-term climate studies. However, the increase in high performance computation resources in recent years has enabled high-resolution models (<4 km) to better resolve physical processes (e.g. topographic effects, local circulation, cloud formation, etc.). Despite this, there is still a great need to evaluate the utility and uncertainty in dynamic downscaling.

Previous studies (De Sales and Xue 2011; Misra et al. 2013; Torma et al. 2015) showed improved skill from using dynamical downscaling with Regional Climate Models (RCMs) as compared to GCMs or reanalysis data. There are also several programs such as Coordinated Regional Climate Downscaling Experiment (CORDEX) (Giorgi et al. 2009) and North American Regional Climate Change Assessment Program (NARCCAP; Mearns and Team, 2009) that aim to investigate local scale physical processes and provide finer RCM simulations. Under these programs, the research indicates better prediction in precipitation extremes for specific climate regions from the RCMs than their coarser counterparts or their driving GCMs, especially in complex orographic regions (Elguindi and Grundstein 2013; Prein et al. 2016; Park et al. 2016). This research also found better prediction of extreme precipitation than mean precipitation, which indicates an added value from finer resolution RCM due to more accurate representation of topography and surface conditions. However, these RCM simulations are still fairly coarse at a 50 km spatial resolution.

From a theoretical perspective, higher model skill is expected with increasing model resolution due to a more complete representation of the land surface heterogeneity. Nevertheless, this may not be true for all situations. For instance, Prein et al. (2016) found improved precipitation in higher resolution RCMs than their coarser resolution counterparts, especially in mountainous regions, whereas other research shows the improvements are limited (Mass et al. 2002; Li et al. 2014; Lee et al. 2017). Mass et al. (2002) found the improved model skill with increasing resolution is significant at coarser (above 10 km) modeling simulations but less visible in finer (below 10 km) simulations. Similarly, results from Tripathi and Dominguez (2013) showed that finer resolution models (10 km) improved prediction of individual storms in summer in the southwestern US but showed little improvement for the winter months. It is clear that model improvement due to increasing resolution varies by model, location and season.

Past grey-zone (1-10 km grid-resolution) studies (Wootten et al. 2016; Prein et al. 2015) have shown that both models with and without cumulus parameterization can produce comparative precipitation. Cumulus parameterization is used to compensate the sub-grid convective processes not resolved at coarse grid-scale simulations. This compensation is expected to be turned off at fine resolutions due to the model's ability to resolve sub-grid processes and some assumptions of the cumulus schemes becoming invalid. However, models may not fully resolve the convection in the grey-zone. For instance, Yu and Lee (2010) found an effectively resolved resolution of 3 km in the PSU/NCAR (Pennsylvania State University / National Center for Atmospheric Research) mesoscale model (known as MM5) for a convection band event and comparable convection structure in models with and without a modified Kain–Fritsch (KF) cumulus scheme at a 6 km resolution. In addition, modified schemes introducing scale-dependency into the convection dynamic processes (e.g. sub-grid mass updraft, dynamic adjustment time scale, entrainment process etc.) and extending the use of cumulus schemes into various resolutions are ongoing research topics (Zheng et al. 2016). These cumulus schemes are called scale-aware schemes (e.g. Grell-Freitas scheme, Multi-Scale Kain-Fritsch, newer Tiedtke etc.) and are found to largely improve original schemes (e.g. reduce excessive precipitation wet bias and present better diurnal cycle) and provide comparative precipitation as models without a cumulus scheme at grey scales (Zheng et al. 2016; Gao et al. 2017; Jeworrek et al. 2019). In this study, the Grell-3 scheme is used as the chosen deep cumulus scheme which is not a strict scale-aware scheme, but it can be applied on fine resolution models (<10 km) allowing subsidence spreading (Skamarock et al. 2008). Because this scheme is still widely used, it is important to check and quantify the advantages of using the cumulus scheme in the grey zone resolution.

There are some recent projects focusing on dynamic downscaling impact in these intermediate resolutions, such as the intra-center downscaling project conducted by NASA (Ferraro et al. 2017) to test the NASA Unified Weather Research and Forecast (NU-WRF) model (Peters-Lidard et al. 2015) employing three resolution runs at 4 km, 12 km and 24 km and a downscaling project conducted by NCAR (Liu et al. 2017) with WRF runs at 4km for two 13-year simulations. However, the NCAR project only focused on 4-km simulations and the NASA project only used cumulus parameterization for all NU-WRF runs, including the 4km simulation. There are studies from the NASA project demonstrating some forecast skill in precipitation (Iguchi et al. 2017; Tian et al. 2017a; Loikith et al. 2018; Kim et al. 2018), but these evaluations are mainly relying on a traditional grid-to-grid comparison framework.

Grid-to-grid comparison (e.g. Pearson correlation, RMSE, contingency table, skill scores), which is analogous to point-to-point verification, is a traditional verification method widely used in model evaluation due to its simplicity. It assumes that the model forecast perfectly match the observations in their spatial and temporal extent. With a fine resolution model, a grid value can be compared to its grid counterpart or to gauge data which locates inside the grid. However, due to the spatial heterogeneity and the inaccuracy and uncertainty from model simulations (e.g. initial conditions, boundary forcing and parameterization of internal model), the forecast spatial distribution could be very different from observation. The low spatial tolerance in grid-to-grid metrics may produce low skill and misleading results (Gilleland et al. 2009). Thus, a more complete evaluation method that allows for small spatial and temporal displacements between the model and the observations is necessary for a comprehensive evaluation, especially for fine resolution models.

Gilleland et al. (2009) summarized four commonly used types of spatial verification methods in model simulation: neighborhood, scale separation, feature (object)-based and field deformation. These four methods have their own advantages that stress different interests and should be carefully chosen for different evaluation purposes. The neighborhood method (e.g. Fractions Skill Score) is used to evaluate properties of a spatial-smoothed field similar to grid-to-grid metrics. It allows for some spatial error but fails to reveal the spatial structure in the field. The scale separation method decomposes the field into multi-scale features and is useful for scale-dependent evaluations. Field deformation methods work similar to feature (object) based methods which aim to match spatial features between observations and model fields. However, the field deformation method cannot identify object features and only works on the entire field. Considering the goal of evaluating the spatial pattern, a feature-based method (i.e. Object-Based Diagnostic Evaluation) is selected in this study to provide more spatial information. Considering this, chapter 2 provides a comprehensive evaluation of NU-WRF precipitation forecast skill stressing the following questions:

1) Does a finer model resolution improve the model skill in precipitation forecast and how much does it improve?
2) Does a model without cumulus parameterization at fine resolution (i.e. 4-km) show better skill predicting precipitation than a model with cumulus parameterization?
3) Is the model skill evaluated from traditional grid-to-grid methods consistent with the skill evaluated from the Method for Object-Based Diagnostic Evaluation (MODE) and what additional spatial information is revealed by using MODE?

1.2 The Role of Different Precipitation in the Drought

Drought has been studied for a long time because of its potential damage to agriculture, ecology and human society. Based on different areas of interest, there are different drought definitions based on meteorology, hydrology, agriculture, groundwater and ecology. Each definition highlights different characteristics of drought, but are commonly characterized as abnormally high temperature, dry soil, precipitation deficit, reduced surface/ground water etc. (Van Loon 2015). To present the condition of temporal water shortage, several indices are widely used to indicate the drought severity, such as the Standardized Precipitation Index (SPI, McKee et al. 1993), Standardized Precipitation-Evapotranspiration Index (SPEI, Vicente-Serrano et al. 2010), Palmer Drought Severity Index (PDSI, Palmer 1965) and U.S. Drought Monitor (USDM, Svoboda et al.

2002). These drought indices compare variables tightly linked with the dry state (e.g. precipitation, soil moisture, temperature, evaporation, runoff etc.) to their historical normal levels, and thus are used for identifying, monitoring and managing drought impacts.

According to past studies, precipitation, temperature and evapotranspiration, which can impact the onset, duration and severity of drought, are the most commonly analyzed variables to explain and quantify the driving force of historical droughts (Otkin et al. 2013; Mo and Lettenmaier 2015, 2016; Hobbins et al. 2016; Erfanian and Fu 2019). Although the relative importance of the three variables are space and event dependent due to specific hydroclimate conditions, precipitation is found in many cases to be the most important driver of drought, especially in the U.S. Central Great Plains (CGP; Livneh and Hoerling 2016; Koster et al. 2019). Unlike temperature, evapotranspiration, radiation or other variables, precipitation can mitigate the severity of drought in a short time by refilling the water storage directly. The fast response in soil moisture (SM) and other water body may have delayed impacts into system directly impacted by water storage, such as ecosystems. This makes precipitation critical for understanding drought evolution.

Although precipitation is the most impactful factor controlling drought, there are few studies analyzing the roles of different precipitation types in drought evolution. Precipitation is usually treated as a whole instead of separating into specific types. Considering precipitation roughly based on scales – local and non-local precipitation, what role the local land-atmosphere (L-A) interaction and non-local atmospheric dynamics play within a drought period has not been well studied. This question is particularly important in CGP, where it has been shown that a strong soil moisture–precipitation (SM-P) coupling relationship exists and thus it is a hot spot for local L-A interaction studies (Koster 2004). From this aspect, two important meso-to-large scale weather systems -- mesoscale convective system and low level jet are necessary to consider in CGP, where both are prevalent and contribute largely to the regional precipitation (Hu et al. 2021).

A Mesoscale Convective System (MCS) is normally defined as an aggregation of convective storms exceeding a certain scale (>100 km in midlatitude) and persists for at least 3 hours (Parker and Johnson 2000). With this definition, MCS can bring long-lasting and intense precipitation. In the Great Plains, MCSs are often initialized at the foot of Rocky Mountains and propagate eastward, which are maximized at night and account for up to 70% of the warm season precipitation (Fritsch et al. 1986; Carbone et al. 2002; Carbone and Tuttle 2008). MCSs also sometimes accompany large scale systems (e.g. cyclones, frontal systems, low level jet) or with other severe weathers (e.g. hails and tornados etc.), which together result in intense precipitation and even flooding (Houze 2004; Peters and Schumacher 2015). Therefore, when defining precipitation types in the CGP, MCS is an important non-local weather system that needs to be considered.

Another important external forcing of precipitation in the CGP is the low level jet (LLJ), which is a strong southerly low level wind prevailing at night and can bring moisture from the Gulf of Mexico inland (Bonner 1968). This process can be facilitated when it is coupled with the upper-level jet. With an upper-level trough to the west of Great Plains and a ridge to the east, a circulation associating with the upper-level divergence (low-level convergence) downstream the trough induce more moisture transport via LLJs and increased precipitation largely in the Great Plains (Wang and Chen 2009). This trough-ridge synoptic structure is also a favorable environment for MCS development where southwesterly warm flow is raised upward to destabilize the air in south and central plain (Peters and Schumacher 2014; Yang et al. 2017). Therefore, MCS easily occur and coincide with coupled LLJ, which in turn supports MCS development and sustains more intense, longer duration and larger MCSs by feeding warm moist air (Houze 2004; Coniglio et al. 2010; Feng et al. 2016).

While the importance of MCS and LLJ in Great Plain has been widely accepted, there is little research illustrating their roles during drought evolution. Barandiaran et al. (2013) found a concurrent northward shift of warm season precipitation and LLJ in the Great Plains from 1979 to 2012 indicating a dominant role of LLJ in precipitation distribution. However, their results also show a weaker relationship between LLJ strength and precipitation during two dry years (2010 and 2012), pointing out some prerequisites are necessary for LLJs contribution to precipitation in the region. Based on this, some of the key research questions that will be addressed in chapter 3 include the following:

1) Which precipitation type (MCS relate precipitation, LLJ relate precipitation or local precipitation) contributes the most during a drought and how is this different for different drought periods?
2) How does the LLJ interact with MCS and local preciption and how well are these events simulated in the model?

1.3 Links Between Soil Moisture and Precipitation

Land-atmosphere (L-A) interactions consists of a series of physical processes that transfer water, energy and other constituents (e.g. carbon, nitrogen …) from the land surface to the atmosphere. Due to limited observations, it is still challenging to fully understand and quantify this complicated process. One of the important topics in L-A interaction is to quantify the processes linking soil moisture and precipitation, which is still not well understood. Previous studies have explored the triggering of convection within soil moisture-precipitation (SM-P) feedbacks with the afternoon being the best time for strong L-A coupling with increased boundary layer growth which can intersect the lifted condensation level (LCL) and trigger convection (Betts and Ball 1998; Eltahir 1998; Findell and Eltahir 2003b; Song et al. 2016; Hsu et al. 2017; Santanello et al. 2018). Afternoon rain is therefore a hot topic for many L-A interaction studies (Taylor et al. 2012; Welty and Zeng 2018; Moon et al. 2019).

However, due to complex nature of the atmosphere, the SM-P feedbacks are not always easily detected. Meso-to-large scale systems such as atmospheric rivers (Lavers and Villarini 2013), frontal systems, MCSs and LLJs can either indirectly alter the atmospheric environment or directly amplify precipitation and interfere with the local SM-P processes. Some research has shown that large scale atomospheric systems are the dominate factor for triggering precipitation rather than the impact from the land surface (Phillips and Klein 2014; Zhou et al. 2016; Song et al. 2016; Wei et al. 2016; Herrera-Estrada et al. 2019). This is espcially true for the CGP study region where MCSs and LLJs are found to produce a large portion of precipitation during the night. Therefore, separating out the impacts of MCSs and LLJs should enable detecting a a stronger L-A coupling signal.

Most past L-A studies choose to analyze the local L-A interactions without seperating out the impact of meso-to-large scale events due to the complicated nature of defining these large systesms. However, the L-A interaction do not stop during days of large scale systems. Furthermore, not only do meso-to-large scale systems produce heavy precipitation changing the soil moisture, the soil moisture can also in turn affect the large scale systems (Campbell et al. 2019; Ferguson et al. 2020; Hu et al. 2021). Therefore, the analysis in this study aims to separate different precipitation types in order to analyze days with local L-A process but also for days with the non-local impacts. Based on this, some of the key research questions that will be addressed in chapter 4 include the following:

1) How does soil moisture affect precipitation formation and when do the strong L-A interactions occurred during a day in the model simulation?

2) How does soil moisture impact the MCSs and LLJs and influence regional precipitation?

Chapter 2: Impact of Model Resolutions and Cumulus Parameterization

Note: The content of this chapter was published in Environmental Modeling and Software (Zhang et al. 2021).

The accuracy of model simulations is mainly based on model configurations and the hypothesized physical mechanism behind them. Understanding impact of model configurations is important before using model simulation as future expectation and interpreting the real-world physical processes. Thus, this chapter provides a basic understanding of two model configurations before digging into precipitation analysis in the next two chapters. The NU-WRF model skill predicting precipitation at different running resolutions, with and without cumulus parameterization are evaluated using both a grid-to-grid method and an object-based method, which provides a comprehensive understanding of the impact of model resolutions and cumulus parameterization. The results also help understanding the model deficiencies and provide the optimal configuration for model simulations used in chapters 3 and 4.

2.1 Datasets

2.1.1 NU-WRF

There are two sets of NU-WRF simulations used in this chapter: (1) NU-WRF runs at 4km, 12km and 24km spatial resolutions with cumulus scheme turned on over CONUS from the NASA downscaling project, and (2) NU-WRF runs at 4km in a smaller region in central US with both cumulus scheme turned on (cu-on) and off (cu-off). Spectral nudging is applied to all model runs for wind, geopotential height and temperature. Spectral nudging is a technique to 'assimilate' upper air variables for self-defined large-scale in spectrum while keeping model ability to develop small-scale features (Waldron et al. 1996; Von Storch et al. 2000). Due to the different domain sizes, models in (1) were nudged at 600 km and models in (2) were nudged at 800 km. However, this small difference in nudging should not impact the overall results (Lee et al. 2017). Except for the cumulus scheme and nudging, other configurations are the same in all simulations (Table 2-1). The atmospheric initial and boundary conditions are forced by MERRA-2 reanalysis data with 6-h intervals. Grell 3D (G3D; Grell & Dévényi, 2002) and UW (Park and Bretherton 2009) schemes are used as deep and shallow cumulus scheme (hereafter refer to GW scheme) except in cu-off simulation. Mellor-Yamada-Janjic (MYJ; Janjić, 1990, 1994, 2002) scheme is used for boundary layer parameterization. The land surface is initialized with 10 years (1990~1999) spin-up period for (1) and an even longer time (from 1990 to May 31 at 2002~2004) for models in (2). In both cases the LIS modeling framework was used with the Noah 3.3 (Chen and Dudhia 2001; Ek et al. 2003) as the land surface model. Three summers (JJA) from 2002 to 2004 are chosen for analysis. To make the two sets of NU-WRF results comparable, only eastern Kansas and western Missouri (hereafter referred to as ROI4-24 for models in (1), Fig. 2-1) are used in analysis. More details of the model configuration can be found in the NASA downscaling project report (Ferraro et al. 2017).

Table 2-1:
Model configurations used in the study

Model	**Resolution**	**Domain**	**Nudging**	**Cumulus scheme**	**PBL scheme**	**Forcing**
ROI4	4 km	CONUS (clip to ROI for analysis)	600 km	G3D and UW	Mellor-Yamada-Janjic (MYJ)	MERRA-2
ROI12	12 km					
ROI24	24 km					
cu-on	4 km	Larger than ROI (clip to ROI for analysis)	800 km			
cu-off				None		

2.1.2 Stage IV

Stage IV hourly precipitation (Lin 2011) is used in this chapter as reference. Stage IV data (hourly/6-hourly) is a mosaicked 4km precipitation estimate based on radar and gauge measurements and is produced by the 12 National Weather Service (NWS) River Forecast Centers (RFCs) over CONUS. Any time with missing values that cover more than 15% of the study region are excluded from the validation. This cut off leads to 6575 valid hours (99.26% of total hours during the three summers) used in the analysis.

2.2 Methods

The goal of this chapter is to evaluate the impact of model resolution and cumulus parameterization in NU-WRF in eastern Kansas and western Missouri (36.3º N to 41.5º N, -100º W to -92.5º W, top plot in Fig. 2-1) from June to August in 2002-2004. With five model runs (ROI4-24, cu-on and cu-off), precipitation from NU-WRF was verified using the Stage IV dataset. The 4km map of cu-on and cu-off were chosen as the standard resolution map (23368 grids in ROI) to ensure a larger number of sample grids in the ROI. All other datasets were resampled to this map projection before analysis. The nearest neighbor method was used for downscaling and the unweighted averaging method was used for upscaling.

To evaluate model precipitation (P), the model skill was first analyzed based on a grid-to-grid comparisons – precipitation frequency, bias and select skill scores (Sect. 2.2.1). To extract a clear skill signal, hourly precipitation data are summed into daily precipitation. These commonly used grid-to-grid metrics provide a basic understanding of model skill. A Method for Object-Based Diagnostic Evaluation (MODE) is then used to verify the spatial patterns of precipitation considering geometry and location of precipitation events. A brief description of MODE is given in Sect. 2.2.2. The spatial verification was assessed only in cu-on and cu-off with hourly data to keep the accuracy of spatial distributions. Since the MODE analysis is sensitive to validating hours, a -6 to 6-h time lag analysis was carried out to check the timing of predicted precipitation.

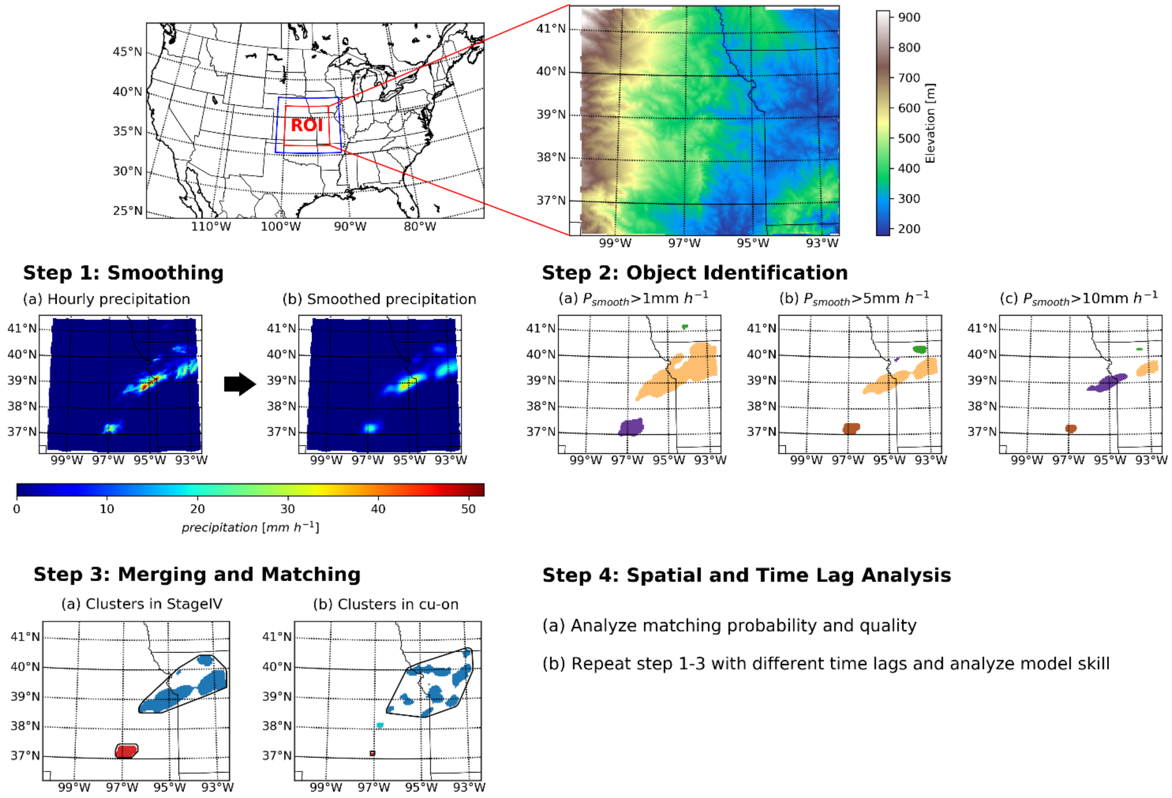

Figure 2-1:
Study region and flow chart of MODE analysis based on hourly data. The blue box shows the running domain for cu-on and cu-off, and the red box shows the analysis region (ROI). Step 1 shows an example of the smoothing process for Stage IV precipitation at 3 a.m. August 28, 2004. Step 2 shows basic simple objects with different colors based on precipitation intensities. Step 3 shows an example of matched clusters between (a) Stage IV and (b) cu-on for Ps>5mm h^{-1}*. The matched clusters are outlined and drawn with the same color.*

2.2.1 Skill Scores in the Study

There are three skill scores used in this study: Heidke Skill Score (HSS), Gilbert Skill Score (GSS) and Modified Taylor Skill Score (MTSS). They are used to assess the model skill on grid-to-grid comparison over the Region of Interest (ROI). Both HSS and GSS (Wilks 2011) measure the model's ability to produce a correct prediction compared to a random reference forecast and are easily calculated from a contingency table. Skill scores like the HSS and GSS provide a meaningful benchmark as positive values indicate more skill than a random forecast. HSS ranges from -1 to 1 with a perfect forecast skill score of 1. The HSS measures model skill based on correctly predicting both precipitation and no precipitation cases and can be calculated from Eq. (2-1) below:

$$HSS = \frac{(a+d)/n-[(a+b)(a+c)+(b+d)(c+d)]/n^2}{1-[(a+b)(a+c)+(b+d)(c+d)]/n^2} \tag{2-1}$$

where a is the number of times the model successfully predicts observational precipitation (hit); b is the count when model predicts precipitation when it was not observed (false alarm); c is the number of times the model predicts no precipitation in precipitation days (miss); d is the number of times that no precipitation is observed in both the model and the reality (also considered a hit); and n is the total number of predictions evaluated.

In contrasts, the GSS evaluates ‘corrected’ hits, which only considers event hits (exclude null events). This is particularly useful for evaluating rare events like precipitation. The GSS ranges from -1/3 to 1 and it can be calculated from equations (2-2 and 2-3) below, where the variables are the same as in equation 2-1:

$$GSS = \frac{a/(a+b+c)-a_{ref}/(a+b+c)}{1-a_{ref}/(a+b+c)} = \frac{a-a_{ref}}{a+b+c-a_{ref}} \tag{2-2}$$

$$a_{ref} = (a+b)(a+c)/n \tag{2-3}$$

Different from HSS and GSS, the MTSS is a skill metric based on correlation and variance of the model compared to observation. MTSS is based on the Taylor skill score (TSS, Taylor, 2001), but assumes that the maximum correlation attainable by the model is 1 and is defined by Eq. (2-4):

$$MTSS = \frac{(1+R)^4}{4\left(NSTD+\frac{1}{NSTD}\right)^2} \tag{2-4}$$

where R is the Pearson Correlation between model and observation and $NSTD$ is the normalized standard deviation of model (standard deviation of model divided by the standard deviation of observation) and is 1 when the model variance equals the observational variance. The MTSS score ranges from 0 to 1 where 1 indicates a perfect match between the model and observations.

2.2.2 MODE Application

The Method for Object-Based Diagnostic Evaluation (MODE) is based on research by Davis et al. (2006a, 2006b) and Brown et al. (2007) to verify field (e.g. precipitation) spatially in a way closer to human's visual judgement. The main idea of this method is to measure the matching pattern in both model and observational fields. The MODE is applied on analyzing precipitation field using Model Evaluation Tools (MET, Brown et al., 2021) v5.1, which is developed by Developmental Testbed Center (DTC) in the U.S. MET includes several modules (such as regridding, grid-to-point and grid-to-grid verification measures, MODE, fields decomposition etc.) to help process and evaluate model predictions (originally designed for the WRF model but can be applied to other models). In this study, the process of implementing MODE for evaluating model precipitation is broken up into four key steps that are visually depicted in Fig. 2-1.

(1) Smoothing: Both forecast (cu-on and cu-off) and observational precipitation (Stage IV) were firstly smoothed (P_s, area weighted average) with a circular radius in MODE (a 4 grid-square radius was chosen as in Davis et al., 2006b) to show the main signal of precipitation distribution.

(2) Object Identification: Considering three different precipitation thresholds (1 mm h^{-1}, 5 mm h^{-1} and 10 mm h^{-1}), event fields were identified for both model and observational data. Each identified separate precipitation area is then called a 'simple object'.

(3) Merging and Matching: All simple objects were then used to calculate a total interest for all pairs of objects between model and observation based on their attributes (i.e. centroid distance, boundary distance, angle difference, area ratio and intersection area ratio). Then a threshold of 0.7 was used in the total interest to define matched objects as suggested in Brown et al. (2007). As a result, an object could match more than one object in the other field, which are merged. Meanwhile, to consider the possible objects caused by the same convective system, any objects

enclosed by the same precipitation contour (70% of thresholds in step 2, which is 0.7 mm h^{-1}, 3.5 mm h^{-1} and 7 mm h^{-1}) were merged again as a cluster to simplify the later analysis. To clarify the term used in this chapter, hereafter, any matched object(s) is (are) called a ‘cluster’, and the word ‘object’ only refers to the simple objects before any merging takes place. More details of matching algorithm can be found in MET user guide (https://dtcenter.org/community-code/model-evaluation-tools-met).

(4) Spatial and Time Lag Analysis: Matching results from MODE (step 1-3) are then analyzed to verify the model skill spatially by comparing the match, miss and false alarm, location and spatial extent of matched precipitation clusters. To account for a potential time lag between the model and observations which could impact the interpretation, this spatial analysis was repeated 13 times with time lags that range from -6 to 6 h.

2.3 Results

2.3.1 Grid-to-Grid Skill Scores

All model and observational data were accumulated into daily precipitation. Days with $P > 1$ mm d^{-1} are considered as precipitation events and used to summarize the contingency table of hit, false alarm, misses and no precipitation ($P < 1$ mm d^{-1}) and the three corresponding skill scores (HSS, GSS and MTSS) are calculated. Table 2-2 presents a summary of these metrics. The general precipitation hit rate is not high (<20%) and is nearly the same as the false alarm rate (~20%) for all models. Most non precipitation days are predicted correctly, which accounts for more than half of the three summers and explains the higher HSS as compared to the GSS. Both HSS and GSS are larger than 0.2 in all models showing that the model skill is better than a random forecast.

Table 2-2:
Contingency table and model skill scores based on daily precipitation

Model[a]	**Precipitation hit**[b]	**False alarm**	**Misses**	**No precipitation**	**HSS**	**GSS**	**MTSS**	**Frequency bias**[c]
cu-on	**18.0%**	19.3%	**5.6%**	57.1%	0.426	0.271	**0.240**	**1.582**
cu-off	12.6%	**7.9%**	11.0%	**68.5%**	**0.451**	**0.291**	0.233	0.871
ROI4	**18.0%**	21.4%	**5.6%**	55.0%	**0.392**	**0.244**	**0.243**	**1.672**
ROI12	17.6%	21.5%	6.0%	54.9%	0.379	0.234	0.216	1.658
ROI24	17.1%	**19.9%**	6.5%	**56.5%**	0.389	0.241	0.218	1.568

[a] Bold numbers are the best performance between cu-on and cu-off and among ROI4-24;
[b] Precipitation in this table is considered as P>1 mm d^{-1};
[c] Frequency bias=(precipitation hit + false alarm) / (precipitation hit + misses)

Considering the impact of the cumulus scheme, cu-off shows a better estimation of precipitation frequency. Table 2-2 shows that the all models with G3D scheme overestimate precipitation frequency (see frequency bias) by 56%-67% whereas cu-off only underestimates precipitation frequency by 12.9%. This shows the large overestimation of precipitation frequency in G3D scheme model simulations and a slight underestimation of frequency in cu-off. Specifically, cu-on shows a higher precipitation hit rate and false alarm whereas the rate of misses and no precipitation hit is higher in cu-off. This difference indicates the spatial error in cu-off should account for its lower precipitation hit rate with a more realistic precipitation frequency. Although the precipitation hit is lower in cu-off, both its HSS and GSS are higher than cu-on. The increase in the HSS and GSS is mainly a result of the reduced false alarm rate which is only 7.9% in cu-off but is over 19% for all models with cumulus parameterization on. This indicates that cu-off has better overall model skill for correctly distinguishing the occurrence of precipitation and no precipitation days, despite its lower precipitation hit rate. On the contrary, MTSS shows an opposite result with a higher skill score in cu-on. This is not too surprising considering the factors (Pearson correlation and NSTD) determining the MTSS as it describes different aspect of model skill rather than the frequency-based skill scores like HSS and GSS. The median of Pearson correlation in cu-on is a bit higher

(0.415) compared to 0.397 in cu-off, but the median of NSTD is closer to 1 in cu-off (1.022) than in cu-on (1.099). The small difference in correlation, NSTD and the overall difference in MTSS of 0.007 imply no clear superiority in either of the two models. The contrasting results of HSS, GSS and MTSS indicate the necessity of multi-aspect assessment to get the whole picture of the model performance.

Unlike the larger differences in precipitation frequency between cu-on and cu-off, the difference among ROI4-24 is small (Table 2-2). The largest difference among ROI4-24 frequency is below 1.6%, and the differences of HSS and GSS are below 0.013 as compared to at least 5.4% differences in frequency and at least 0.02 difference in HSS and GSS between cu-on and cu-off. This indicates a smaller influence of model resolution than cumulus scheme. ROI4 does show the highest value in all three skill scores indicating an improved prediction in the 4-km spatial resolution simulation, but this improvement is not consistent with the increase in model resolution. This inconsistent change in increasing model resolution could be caused by resampling uncertainty since all models are compared at 4 km resolution. To validate the impact of map resolution, all three skill scores was calculated at 12-km and 24-km map resolution as well. The results (Fig. 2-2) showed a similar comparison in that ROI4 outperformed ROI12-24. Furthermore, ROI12 has lower skill scores than ROI24 in nearly all map resolutions. An increased difference in skill scores is found between ROI4 and ROI12/ROI24 with the increasing map resolution, which implies that the increased skill of the 4 km model is partially caused by its better representation of land surface heterogeneity and thus results in better skill scores based on a grid-to-grid comparison. This is further supported by the difference between ROI12 and ROI24, which decreases with increasing map resolution in HSS and ROI12 even overtakes ROI24 in MTSS when evaluating at a 24km resolution. Therefore, despite the inconsistent comparison between ROI12 and ROI24, ROI4 does show some improvement over the coarser model simulations.

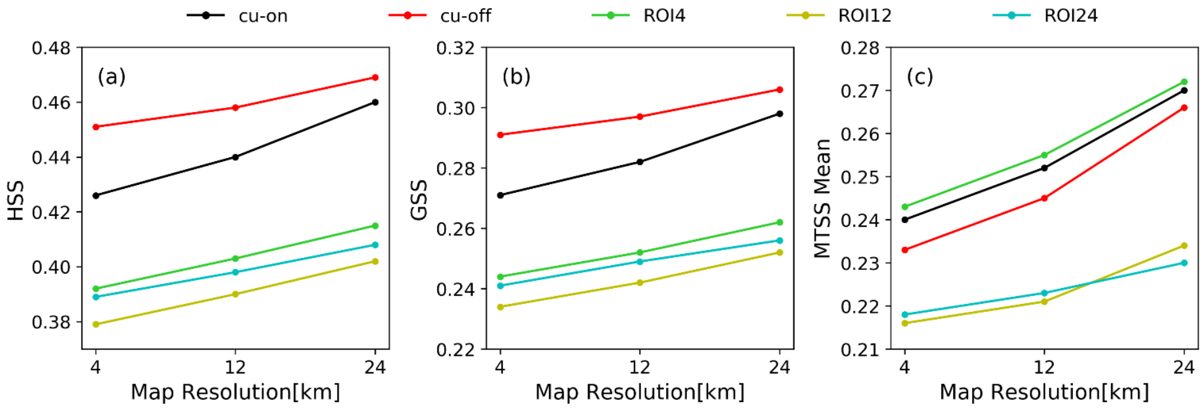

Figure 2-2:
Impact of map resolution on different model skill scores: (a) HSS, (b) GSS, (c) MTSS.

2.3.2 Grid-to-Grid Precipitation Bias

To present the precipitation bias clearly, a probability of bias bins is calculated in Figure 2-3 considering three cases: precipitation days (P_{obs}>1 mm d^{-1}), no precipitation days ($P_{obs}\leq1$ mm d^{-1}) and all days. The plot is created by first categorizing daily grid bias into different bins, and then calculating the portion (probability) of each bin. All models show the largest probabilities for bias=0 (-0.01~0.01) in all days (Fig. 2-3c) due to the large portion of no precipitation hits (Fig. 2-3b). For precipitation days, on the contrary, all models have a bias all the time (probability of 99.9% in Fig. 2-3a). It is clear that the bias distribution is different depending on whether it rains or not. There is a slight wet bias (0-2 mm) in nearly all models for no precipitation days (Fig. 2-3b) but a slight dry bias (-4-0 mm) in precipitation days (Fig. 2-3a). The overall performance is different for each model (Fig. 2-3c). All models with GW scheme (cu-on and ROI4-24) show an overall wet bias (17%-22%), which is mainly due to the wet bias in no precipitation ($P_{obs}\leq1$ mm d^{-1}) events that account for 76.47% of the time. On the contrary, the positive and negative bias are more evenly distributed in cu-off. The difference between cu-on and cu-off indicates that GW scheme produces slightly more precipitation for about 8% of time in our study region. Therefore, cu-off has better skill with less precipitation bias compared to cu-on. The relative suppression in cu-off is consistent with its frequency analysis (Table 2-2) which has less false alarms, more misses and no-precipitation days.

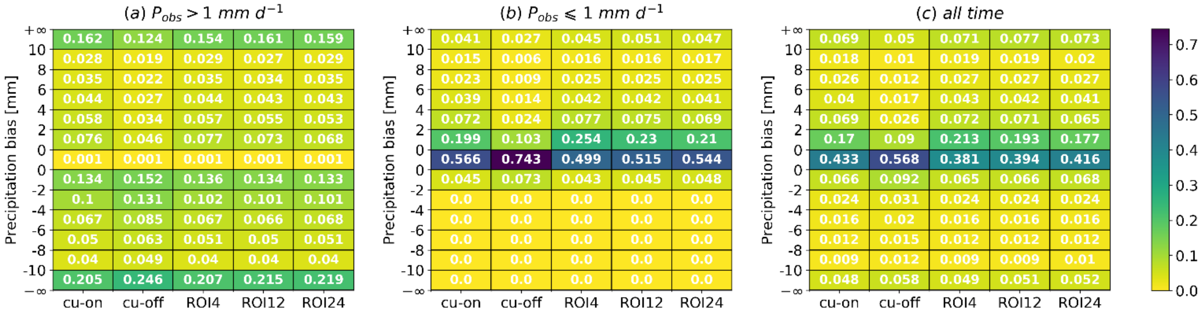

Figure 2-3:
Probability of precipitation bias for all models with cases: (a) precipitation days (observational daily precipitation $P_{obs} > 1$ *mm* d^{-1}*); (b) no precipitation days (*$P_{obs} \leq 1$ *mm* d^{-1}*); (c) all days of three summers (JJA) in 2002-2004.*

There is no improvement in the bias for finer resolution models. Unlike the skill scores, the bias increases from ROI24 to ROI4 based on the decreasing no bias probability. This unexpected result may be caused by using GW scheme, whose assumptions may not be appropriate for finer resolutions. Nevertheless, the total difference of bias probability (bias not equal to zero) between ROI4-24 (less than 4% in Fig. 2-3c) is much smaller than the difference between cu-on and cu-off (13%), which indicates there is less impact due to model resolution as compared to cumulus parameterization.

The GW scheme explains the small wet bias in no precipitation days, but the cause of the mutual small dry bias in precipitation days is unknown. Moreover, all models show similar probabilities of extreme bias (> 10 mm or < -10 mm), which are even larger than the probabilities of small bias (-2-0 mm and 0-2 mm) in precipitation days (Fig. 2-3a). Only about 4% of positive or negative extreme bias in precipitation days are explained by the use of GW scheme. Figure 2-4 shows a spatial distribution of days with extreme bias when precipitation occurs ($P_{obs}>1$ mm d^{-1}) in cu-on.

The extreme bias is widely distributed and does not spatially compensate between wet days and dry days. All models (Fig. 2-5 and Fig. 2-6) produced a similar distribution of the extremely dry bias with cores (count > 20 days) in North Kansas, Midwest Missouri and Northeastern Oklahoma. Consistent with the previous analysis, cu-off shows a suppression of precipitation spatially compared to cu-on, with more days of extreme dry bias than days of extreme wet bias.

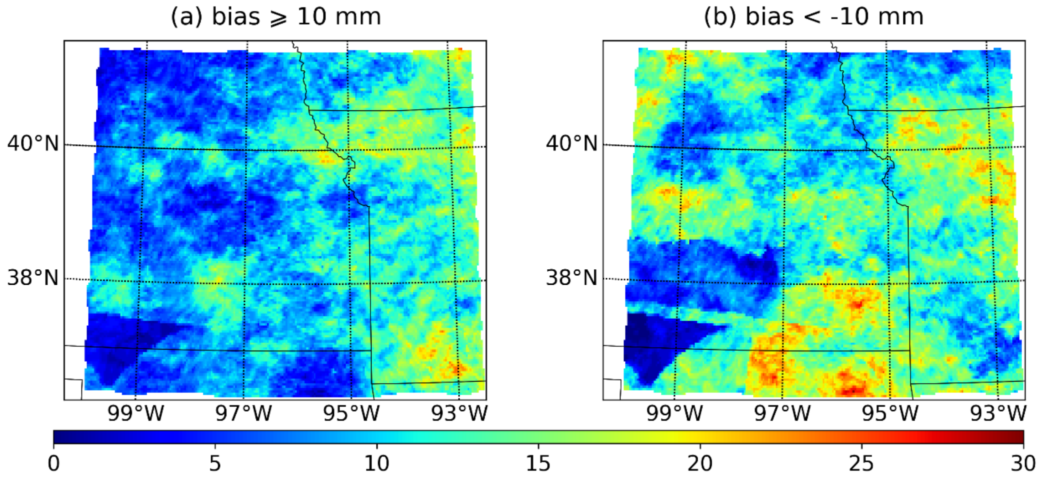

Figure 2-4:
Spatial distribution of extreme bias days in cu-on model for $P_{obs} > 1$ *mm* d^{-1}*. Map color shows the day count that a grid falls into the bias bin during the three summers in 2002-2004 (263 valid days). The region with small counts and obvious bounds in the bottom left is caused by the missing value in Stage IV, which reduces the counting days.*

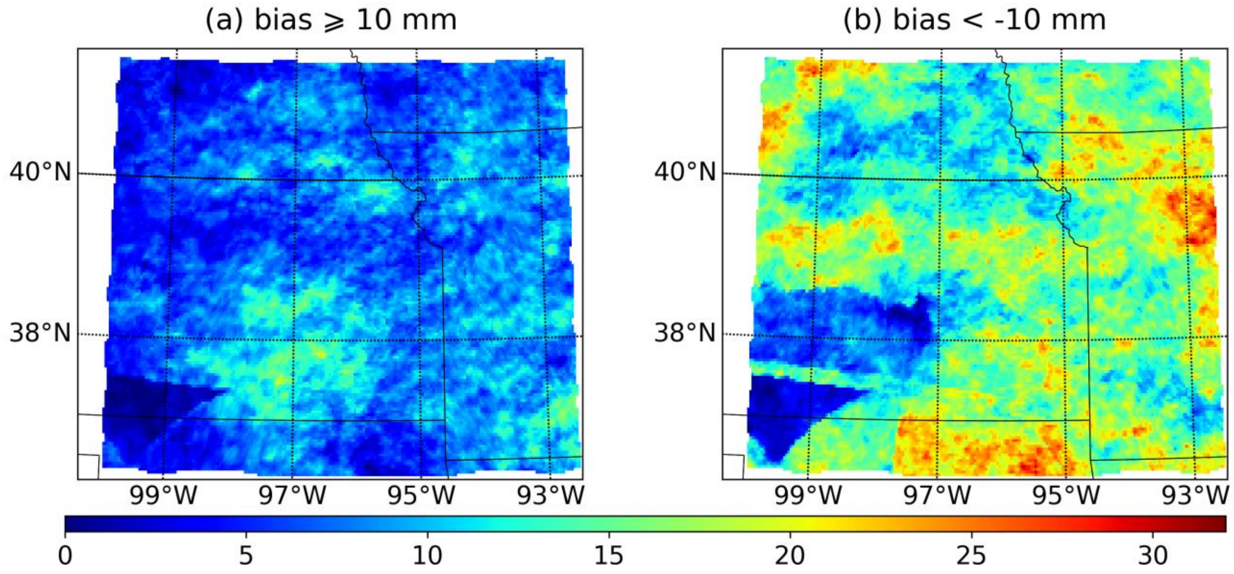

Figure 2-5:
Spatial distribution of extreme bias days in cu-off model for $P_{obs} > 1$ *mm* d^{-1}*.*

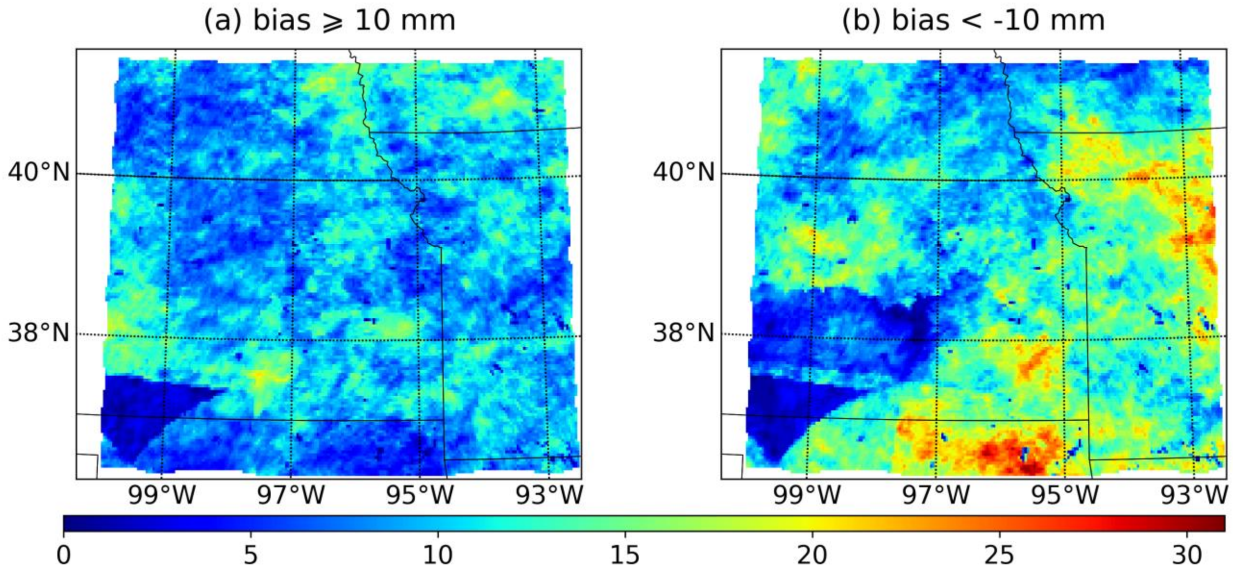

Figure 2-6:
Spatial distribution of extreme bias days in ROI4 model for $P_{obs} > 1$ *mm* d^{-1}*. The spatial distribution in ROI12-24 are quite similar and omitted to show here.*

2.3.3 Object-based Spatial Analysis

The previous grid-to-grid analysis shows very limited difference of model skill among ROI4-24, which may be caused by the same configuration except for their resolutions. Therefore, the spatial and time lag analyses (Sect. 2.2.4) are only conducted on the cu-on and cu-off model simulations. To assess the spatial matching performance, hourly simple objects identified from MODE are analyzed to get the probability of match, miss and false alarm in Table 2-3. This table is, however, different from a normal contingency table which gives a total probability of 1. Based on objects, the counts of three measurements are defined as: (1) Match: the minimum number of objects between matched clusters; (2) Miss: the number of unmatched objects in observation; (3) False alarm: number of additional objects in the model compared to matched objects. The probability of the three measurements in Table 2-3 are then calculated differently. Match and miss probability are the portion of matched or missed objects in observation (match or miss counts/total observational objects), which give the sum of two probabilities equal to 1. As a contrast, the probability of false alarm is referenced to model objects (false alarm counts/total model objects). The reason for choosing simple objects instead of matched clusters to count the probability is due to the matching process in MODE. The MODE treats all unmatched objects as a whole cluster even though they may belong to different events. The incapability of recognizing multiple unmatched events (clusters) by the algorithm makes standard use of the cluster method inappropriate to assess the probability of matching.

Table 2-3:
Matching probability of hourly precipitation objects

Model	P_s>1mm h^{-1} [a] (60% of time[b])			P_s>5 mm h^{-1} [a] (39.1% of time[b])			P_s>10 mm h^{-1} [a] (24.2% of time[b])		
	Match[c]	Miss[c]	False Alarm[c]	Match[c]	Miss[c]	False Alarm[c]	Match[c]	Miss[c]	False Alarm[c]
cu-on	38.5%	61.5%	76.2%	16.7%	83.3%	82.3%	7.9%	92.1%	89.8%
cu-off	28.0%	72.0%	71.7%	16.7%	83.3%	82.2%	10.4%	89.6%	88.9%

[a] P_s is the smoothed precipitation used to identify simple objects;
[b] Time with observational events occurred compared to total sample hours = 6575 h (273.96 day) in 2002-2004 summers (excluding dates with large missing area in Stage IV);
[c] All match, miss and false alarm are based on comparison of simple objects (instead of matched clusters). This table only account for times when at least one object is found in model or observational field.

From Table 2-3, both cu-on and cu-off have a high miss rate (>60%) and a large false alarm rate (>70%) especially for intense precipitation events, indicating spatial or/and temporal mismatch of precipitation events. To better understand the cause of the low matching rate, the total number of objects and a ratio of event hours (hours with objects in the model/hours with objects in the observations; Table 2-4) are used to show the event frequency in the model. Except in cu-on when P_s>1 mm h^{-1}, both models in all precipitation intensities produced overall equivalent or less objects than observation, which seems to contradict the high false alarm rate. However, nearly all ratios of event hours are less than 1, which indicates widespread precipitation (more objects, also confirmed by the area ratio much larger than 1 in Fig. 2-9) with less temporal frequency (fewer hours with precipitation) produced by the model. A more detailed event comparison can be seen from Fig. 2-7. Both models overestimate events (Obj_m>Obj_o) and this overestimation decreases with increasing intensity from 30%-50% to 10%-20%. This decreasing trend is opposite to the increasing false alarm rate with more intense events (Table 2-3) and again strengthens the idea that both models produce more precipitation events in a short time period, especially for high intensity events. In contrast, both models tend to produce fewer events (>55%) in rainy hours ($Obj_o>0$), which explains the high miss rate in Table 2-3. Thus, the high miss rate and false alarm rate are caused in different ways despite the large portion of no-precipitation hit hours ($Obj_m=Obj_o$ is more than 59% of time in Fig. 2-7b).

Table 2-4:
Object counts at different precipitation intensities

	Total objects (events)			Ratio of event hours [a]	
	cu-on	cu-off	Stage IV	cu-on	cu-off
$P_s>1$ mm h^{-1}	20993	12858	12997	1.147	0.905
$P_s>5$ mm h^{-1}	6287	6259	6670	0.838	0.862
$P_s>10$ mm h^{-1}	2474	3017	3219	0.726	0.863

[a] Ratio of event hours = hours with objects in model/hours with objects in observation

When comparing the two models, there is a large difference in matching probability (Table 2-3) and time components (Fig. 2-7) of light precipitation events. For $P_s>1$ mm h^{-1} observational events (Fig. 2-7a), cu-on overestimated precipitation objects for most of the time (53%) whereas cu-off only overestimated for 30% of the time. Similarly, for no observational events (Fig. 2-7b), cu-on overestimated 41% of the time which is 17% more time than cu-off. This large difference is only found in light rain events (1 mm $h^{-1}<P_s<5$ mm h^{-1}) whereas both models have nearly the same matching probability and time components for $P_s>5$ mm h^{-1} and $P_s>10$ mm h^{-1}. Although cu-on overestimated light rain events ~20% more often than cu-off (Fig. 2-7), it produced a 10.5% higher matching probability (Table 2-3). This seemingly contradiction could be explained by the different reference that matching probability is compared to observational objects while the false alarm rate is reference to model objects. The largely overproduced objects (almost the same number of observational objects in Table 2-4) for light precipitation in cu-on not only increased the denominator (total model objects) of false alarm rate but also increased the matching observational objects as well.

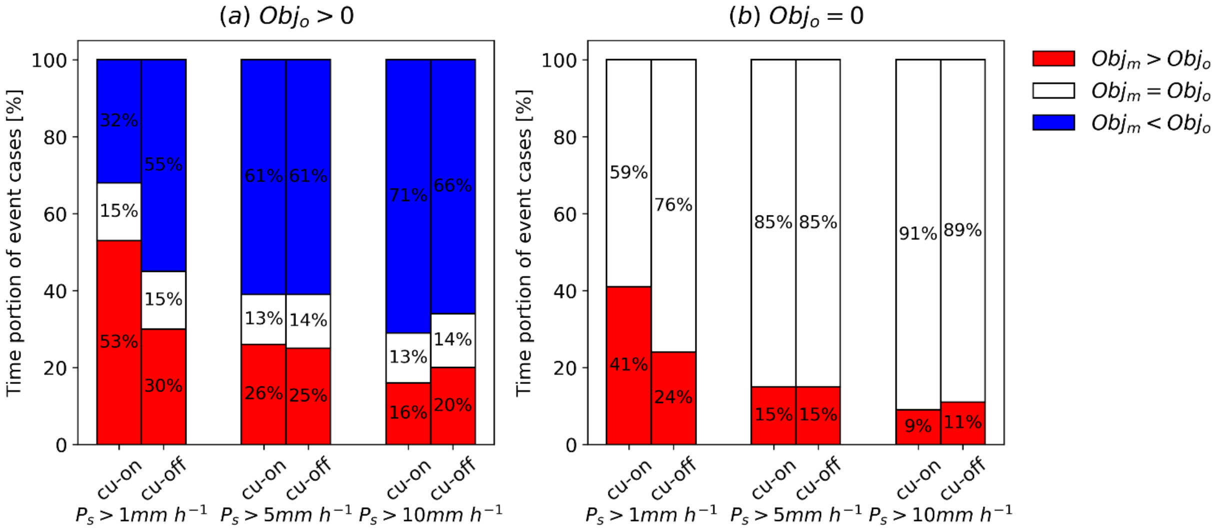

Figure 2-7:
Time components of event comparison based on simple objects. Red, white and blue bars show the percentage of time that model objects (Obj_m) are more, equal or less than observational objects (Obj_o) separately when observational precipitation events based on different intensities (a) occurred ($Obj_o>0$) and (b) not occurred.

In addition to evaluate matching rate based on simple objects, it is also informative to further assess the matching quality based on clusters. Before digging into the quality evaluation, Figure 2-8 provides a histogram of event scale (area) for all matched clusters for three different intensity thresholds. Clearly, both the number of events and precipitation area decrease with intensity. The logarithmic area distribution shows the general precipitation scale smaller than 10000 km^2 (~50 percentile for P_s>1 mm h^{-1}) for cu-on and 5700 km^2 for cu-off. Although cu-off produced smaller-scale precipitation compared to cu-on (Fig. 2-8a), the scale of intense precipitation is larger (Fig. 2-8c, P_s>10 mm h^{-1}). Similarly, cu-off has less matched precipitation clusters at low intensities but more for intense events. This indicates a preference of light yet larger-scale precipitation in cu-on, whereas cu-off produced relatively more intense but smaller-scale precipitation. By checking the intensity ratios of matched clusters (Table 2-5), it is found that the cu-on tends to overestimate light rain intensity while underestimating heavy rain intensity. The cu-off generally produces rain intensity closer to observation but it overestimates heavy rain intensity.

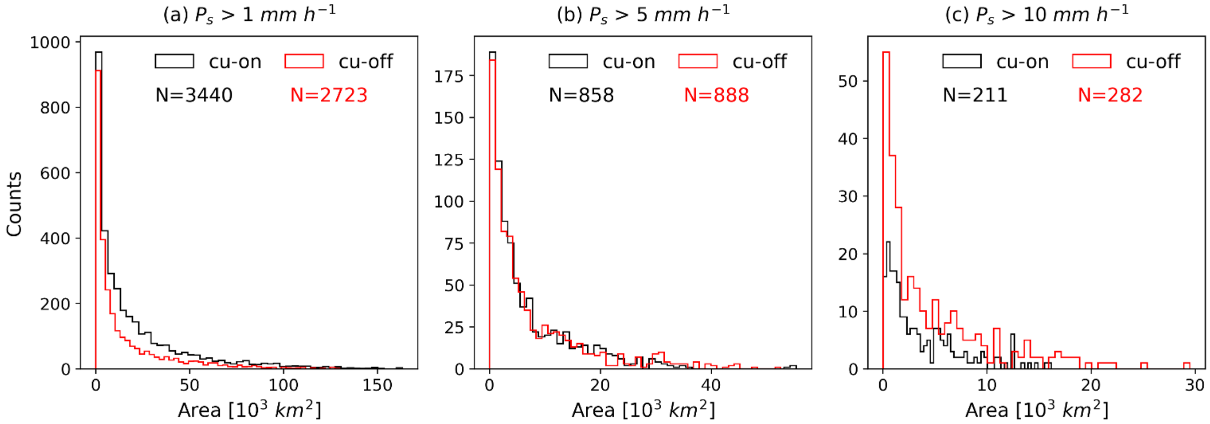

Figure 2-8:
Histogram of event scale (area) for matched clusters. All matched events are divided into 50 bins. The total events are written in corresponding colors (black for cu-on and red for cu-off).

Table 2-5:
Precipitation ratios (model/observations) at different intensity percentiles (P_s>1mm h^{-1}).

Intensity Percentile	Ratio	
	cu-on	cu-off
10	1.561	0.923
25	1.247	1.003
50	0.937	1.089
75	0.795	1.163
90	0.784	1.227

In order to assess the matching quality of the spatial pattern, the spatial error (distance between mass centers) and area ratio (area of model cluster (A_m) / area of observational cluster (A_o)) of matched clusters were used to imply spatial accuracy. It should be noted that the area ratio here is different from the definition in MET. The area ratio in MET is defined as the lesser object area over the larger object area, which is less informative for comparative analysis as the reference changes based on which object is larger.

To present the main performance of the two models, 10% of the data are removed from one side (centroid distance) or both sides (area ratio) to exclude extreme values (Fig. 2-9). Both cu-on and cu-off have a large range of spatial error with the mean around 58-70 km. The cu-off seems to show a better forecast in location with a shorter mean distance, but the mean difference between two models is small (4-6 km smaller in cu-off). Results in area ratio (Fig. 2-9b) shows that both models overestimate precipitation scale (all mean area ratio are at least 2 times greater). Unlike the spatial error, not all mean area ratios are closer to 1 in cu-off especially for P_s>10 mm h^{-1}. Although cu-off does not predict better precipitation scale than cu-on in all intensities, it shows a smaller variation in both spatial measurements indicating a more stable performance of model skill in the case of different intensities. The inconsistent change with intensity in cu-off contrasts that from cu-on, which is found to reduce the matching distance and area ratio for higher intensity events. This difference may relate to the use of the cumulus scheme. However, with only one specific cumulus scheme (GW) used in this study, the relationship between spatial prediction and precipitation intensity while using the cumulus scheme is not certain. Further research using other cumulus schemes to test the trend is left for future work.

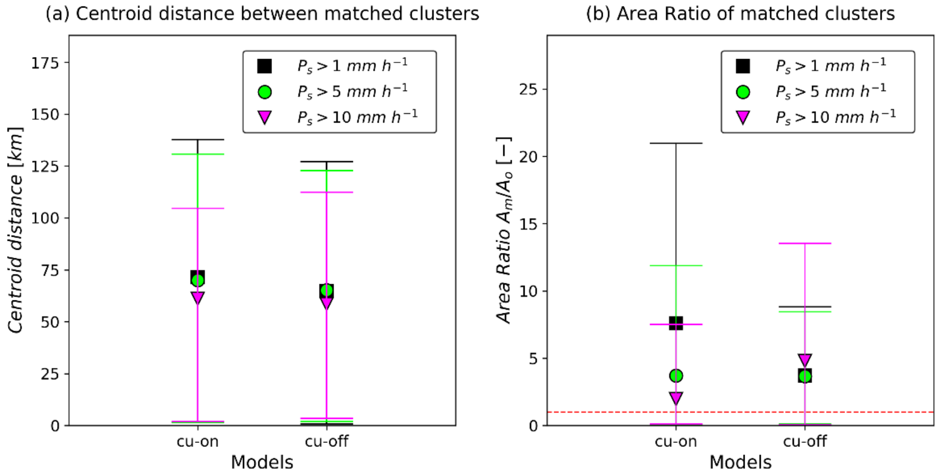

Figure 2-9:
(a) Centroid distance and (b) area ratio of matched clusters in cu-on and cu-off. Symbols show the mean value of each attribute. The upper and lower limits in (a) are 90 percentiles and minimum values and in (b) are 95 percentiles and 5 percentiles respectively. Different colors represent for different precipitation intensities. The dashed red line in (b) shows the perfect prediction with area ratio of 1.

2.2.4 Time Lag Analysis

The results above are sensitive to time lag which could mislead the interpretation of model skill, especially with at least 10% of the time when both cu-on and cu-off have missed or overproduced the precipitation events (ratio of event hours in Table 2-4). To assess the temporal difference, the time lag influence was analyzed by repeating the spatial matching process 13 times with up to 6-h lags of both prior (negative) and subsequent (positive) forecasts. A comparison of spatial error and area ratio of matched clusters is present in Figure 2-10.

For low intensity events (P_s>1 mm h^{-1}), both models show clear decreasing trends in matching distance as the time lag moves towards 0 (Fig. 2-10a). Similarly, the area ratio is generally lower around lag 0 and increases with larger time lags when P_s>1 mm h^{-1}. Although the smallest value of cu-on occurs at time lag of -1 h, the little difference in matching distance between lag=-1 h and lag=0 h could be caused by its larger number of simple objects in matched clusters. With largely overproduced precipitation events of P_s>1 mm h^{-1} (Table 2-4), the number of simple objects formed a cluster in cu-on is more than its counterparts in cu-off. The more simple objects in the cluster, the more uncertain the spatial error of the cluster is shifted. Meanwhile, more simple objects in a cluster also leads to a larger cluster area, which results in a larger area ratio. This explains the better performance of cu-off which shows a 5.4 km shorter mean matching distance and 3.1 smaller area ratio than cu-on (Fig. 2-10a). Nevertheless, all clear trends and comparison along the time lag axis disappear in moderate to intense precipitation events (Fig. 2-10b-c) indicating poor skill in both models to predict spatial and temporal patterns for these events. These clear trends are also found in 5th and 95th percentile data (Fig. 2-11). Although the matching distance and area ratio have a large variation (can be seen from Fig. 2-9), the overall trend shows the peak and trough (shortest distance and area ratio closest to 1) around lag 0. Likewise, the time dependency of the 5th and 95th percentile decreases as precipitation intensity increases.

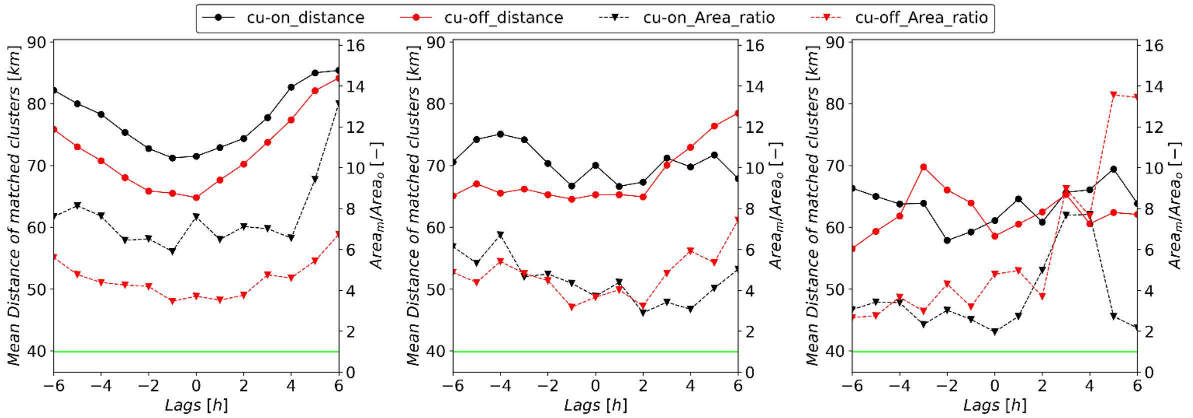

(a) $P_s > 1\ mm\ h^{-1}$ (b) $P_s > 5\ mm\ h^{-1}$ (c) $P_s > 10\ mm\ h^{-1}$

Figure 2-10:

Time lag dependency of (1) left y-axis: mean matching distance, and (2) right y-axis: area ratio in different precipitation intensities. Plots are based on matched clusters. Area ratio is the ratio of area of matched clusters in model and observation. Green line on the bottom shows the perfect area ratio of 1.

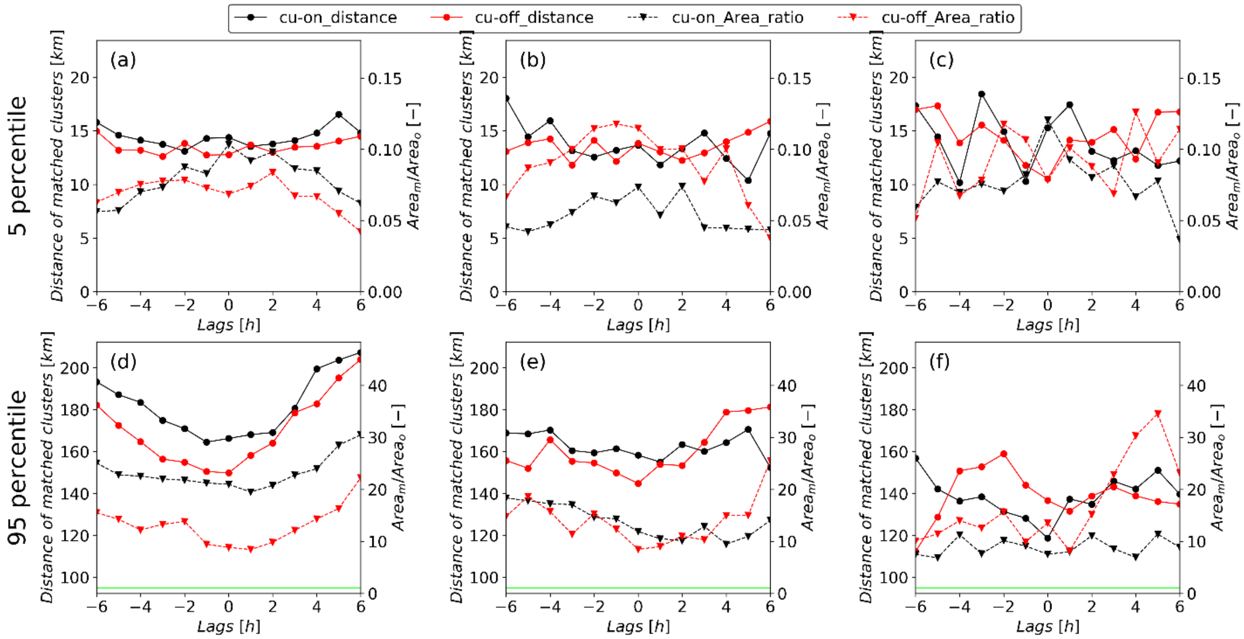

$P_s > 1\ mm\ h^{-1}$ $P_s > 5\ mm\ h^{-1}$ $P_s > 10\ mm\ h^{-1}$

Figure 2-11:
Time lag dependency of mean matching distance and area ratio at 5 and 95 percentiles

2.2.5. Probability of Object Detection

Because using object-based method, there is the possibility that the paired precipitation object falls out of the region and thus considered as unmatched. This uncertainty in object detection relies on the domain size, the location of the object and the searching distance for possible matching objects. To evaluate this uncertainty, a probability of detection was calculated. Figure 2-12 shows a schematic plot illustrating the detection of an object which could match with a known object and falls inside the ROI. Assuming the searching distance is R (R<1/2domain size) and the searching region is a square box with the length of 2R+1, the probability that an object matches with a known object and falls into the ROI can be calculated as below.

$$m = \min(R + 1, \min(nx + 1 - i, i)) \tag{2-5}$$

$$n = \min(R + 1, \min(ny + 1 - j, j)) \tag{2-6}$$

$$P_o = \frac{[R+m(i)]\times[R+n(j)]}{(2R+1)^2} \tag{2-7}$$

Where P_o is the probability and i and j are the row and column number of the centroid for a known object inside the domain. Considering that the known object can be anywhere inside the domain, the overall probability that the matching objects falls into the ROI can be calculated as below.

$$P = \frac{\sum_{j=0}^{ny}\sum_{i=0}^{nx} P_o}{nx\times ny} = \frac{\sum_{j=0}^{ny}\sum_{i=0}^{nx}\frac{[R+m(i)]\times[R+n(j)]}{(2R+1)^2}}{nx\times ny} \tag{2-8}$$

Where nx and ny show the size (number of columns and rows) of the ROI. The larger the domain and the shorter the searching radius R, the higher the probability it can be detected for the potential matching objects.

Figure 2-9 shows that 90 percent of the matched clusters are within a distance of 150 km. Thus, the 150 km (37.5 grids) is used as a searching distance R which result in a detection probability of 76.67%. This means there is at least a 76.67% of probability to detect 90% of the matched objects.

Based on this, results presented in this chapter should be overall reliable measures of the model skill.

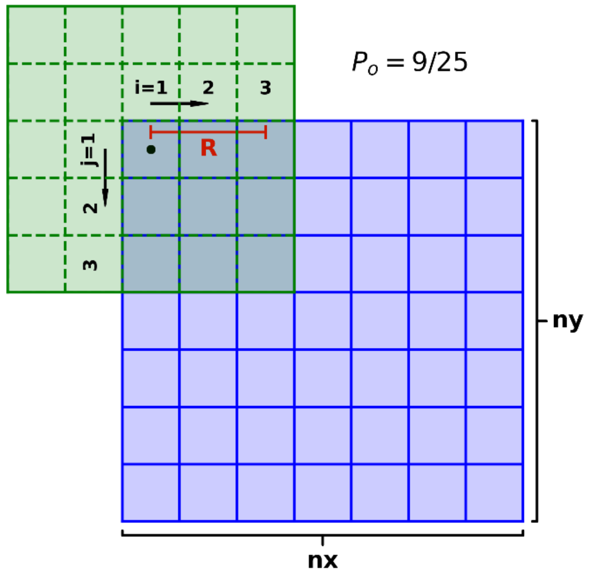

Figure 2-12:
Schematic plot to calculate probability of detection. The Blue region represents the given ROI. The green region represents the searching region of an object which could match with a known object (black dot shows the centroid of a known object). R is the searching distance. The overlapped region shows the probability that the potential matched object could fall into the ROI. The plot shows an example of a known object with centroid of i=0 and j=0, which gives the detection probability of P_o*=9/25 for its potential matching object.*

2.4 Discussion

The improvement in model skill caused by finer resolution is found to be very limited in the study. Although improvement is not found from 24 km to 12 km, ROI4 shows slightly better prediction in frequency (Table 2-2) in all three skill scores. The worse bias probability (Fig. 2-3) in ROI4 could be explained by GW scheme, which was designed to operate at coarse resolutions. Similarly, an hourly precipitation analysis by Lee et al.(2017) shows both larger diurnal bias and better overlap of joint probability distribution function (JPDF, between duration and peak intensity) in 4-km NU-WRF model compared to the coarser models in Central Plains. The contrasting results of both this daily analysis and Lee's hourly analysis point out the limited value added by finer resolution of NU-WRF models in this region. One of the possible reasons is that the spatial heterogeneity in Central Plain is less than other regions such as Rockies where there is a larger elevation expanse. As mentioned in Mass et al. (2002), there is a point of diminishing returns in forecast models and it varies from finer resolution (10-15 km) in Western U.S. to a coarser resolution (20-40 km) in the eastern part where mesoscale features are already well resolved in coarser resolution because of the flatter terrain. Thus, the small added value from surface heterogeneity in our research area competes with error caused by the GW scheme being applied at finer resolutions. In addition, as spectral nudging is used in this study, deficiencies in MERRA-2 could be introduced to impact the physical solution of the model and hence reduced the improvement by the finer resolution models.

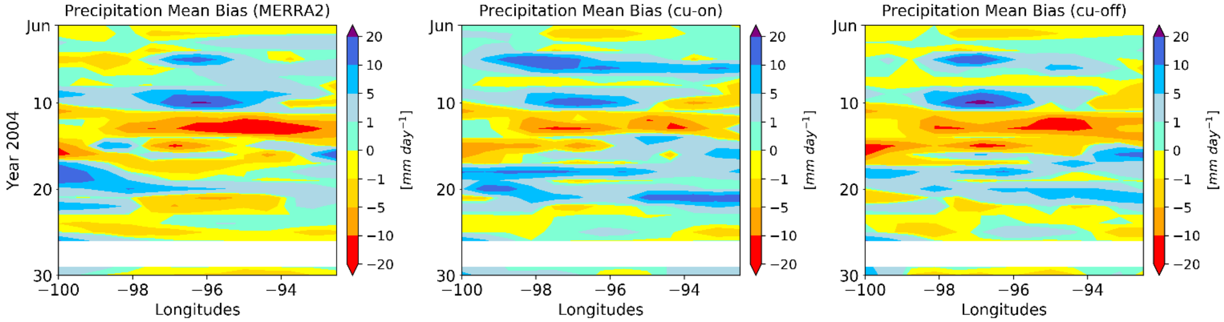

Figure 2-13:
Hovmöller diagram of precipitation mean bias in June 2004. Negative values of longitudes are degrees in West. Reference is Stage IV daily precipitation. The blank (white) bars show the dates with missing data in Stage IV data and are exclude from analysis.

This study also shows some interesting findings. There is a slightly dry bias and about 35% extreme bias (P>10 mm d^{-1} and P<10 mm d^{-1}) in precipitation days in all five models (Fig. 2-3). These mutual biases in all five models indicate dominate factors other than cumulus parameterization and model resolution. One possible cause could be from the MERRA-2 boundary condition. To analyze this, the model precipitation (not gauge corrected) from MERRA-2 was used as a reference instead of gauge corrected precipitation to compare the spatial similarity between the NU-WRF and MERRA-2. If there is a similar pattern between MERRA-2 and the result in this study, it means that the boundary condition might be a reason for the bias. Figure 2-13 shows the Hovmöller diagram of precipitation mean bias for MERRA-2, and the cu-on and cu-off model runs in June 2004. The full three-summer performance is shown to have similar results in Fig. 2-14. There is not a strong trend for dry or wet bias in MERRA-2. The same is true for the eastward propagation. Besides the larger and wider wet bias in cu-on, the spatial patterns of bias in cu-on and cu-off are quite similar as in MERRA-2 from a coarser temporal scale, especially for the extreme bias. This similarity supports the idea that MERRA-2 boundary conditions and nudging may be the cause for the overall bias in all model runs.

However, to fully understand the cause of this bias requires more analysis including considering other boundary forcings. Besides the boundary condition, other model parameterizations such as radiation, PBL and the land surface all play important roles in predicting precipitation and may also contribute to the bias (Pei et al. 2014; Li et al. 2014; Hirsch et al. 2019). It should be noted that the impact from these parameterizations may vary with domain, model, and the research period. In addition, the lack of convection propagation (Liu et al., 2017) and the time inconsistency between model and observation can also result in bias. Analysis in chapter 3 shows largely underestimate night-morning mesoscale convective systems (MCSs) and a potential dry persistence caused by overestimate net shortwave radiation and inaccurate flux partition which might explain the extreme and slightly dry bias in the model. Although not all possible factors mentioned above were checked in this dissertation, results from chapter 3 shows a potential cause and the rest of the untested factors can be explored in future studies to better understand shortcomings in precipitation prediction.

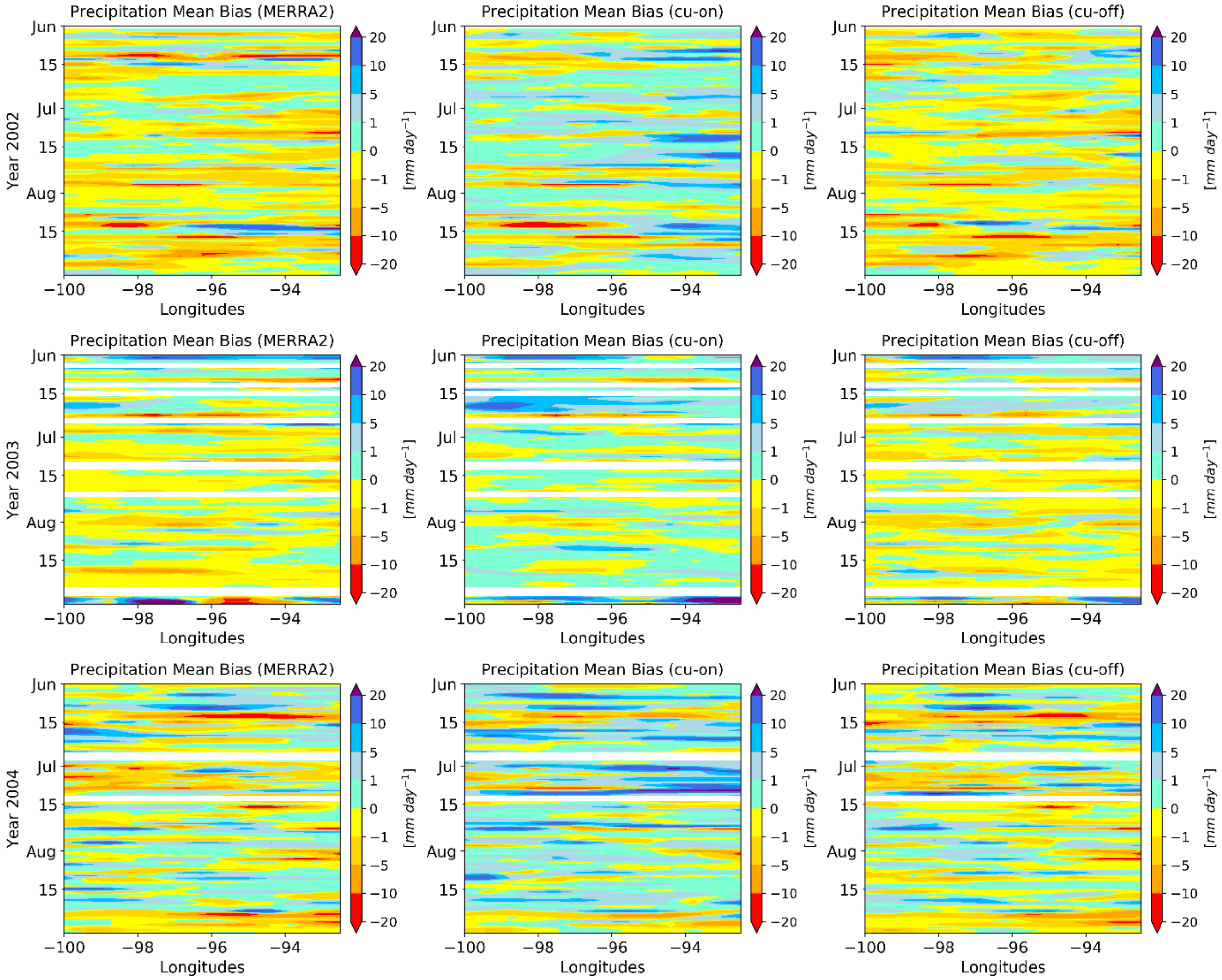

Figure 2-14:
Hovmöller diagram of precipitation mean bias in Jun-Aug for 2002-2004.

This study not only analyzed the spatial pattern but also revealed an imperfect pattern of forming precipitation in cu-on and cu-off models. The low matching rate and the poor matching quality in both models show the large mismatch of precipitation events in terms of spatial pattern. Although there is no consistent time lag in cu-on and cu-off, the large spatial discrepancy could be partly caused by the model patterns. The largely overestimated objects (Table 2-4) and 55% overestimation time (Fig. 2-7) in cu-on for light rain events (P>1 mm h^{-1}) contrasts with its intense precipitation cases and indicate an easy triggering for shallow convection in cu-on with a larger rain area (Fig. 2-9). This is consistent with research of Yu and Lee (2010) who found the excessive cumulus rain region reduced after modified trigger function in Kain–Fritsch (KF) scheme. However, for more intense precipitation and cu-off simulations, fewer hours with events are produced indicating a possible obstacle to initializing precipitation, although the generated precipitation area is still larger than observation (Fig. 2-9). This may relate to the deep convection in the model, which contributes more intense precipitation. Interestingly, this pattern is clearer in cu-on with even less precipitation events for P>10 mm h^{-1} than cu-off. Because the cumulus precipitation can be an adding component representing sub-grid processes, the less intense events in cu-on indicates insufficient ability to develop deep convection using G3D scheme. Only ~15% of time both models correctly predict event counts (Fig. 2-7a). This time portion is stable despite the model and precipitation intensities, which points the problem towards the other aspects of the NU-WRF model rather than the use of cumulus parameterization.

There are some uncertainties in this study, such as the uncertainty of resampling, the choice of observational dataset and the probability of object detection near the edges. However, results in Figure 2-2 show small resampling impact. The change of map resolution does not change the relative position among models in nearly all three skill scores. The variation in three resolution standards is within 14%, with an average of 6%, 7% and 10% for HSS, GSS and MTSS respectively. All 4 km models (ROI4, cu-on and cu-off) show higher skill scores than ROI12-24 in all three resolutions. ROI12 has lower skill scores than ROI24 in most map resolutions, but the difference between them is less than 0.01. Therefore, the decision of using 4 km map as the standard projection in this study should not make a big impact on the analysis.

As for the uncertainty from observational dataset, a similar analysis was done in the preliminary test (not shown) using Livneh daily precipitation with a smaller ROI in five Julys from 2000 to

2004. Again, the impact of model resolution is separate from the use of cumulus parameterization. Results from the test are similar to this study. The overall wet bias in all times, the slightly dry bias and more than 28% probability of extreme bias in precipitation days were all reproduced. The improvement in finer resolution model is small (MTSS of ROI4, ROI12 and ROI24 are 0.166, 0.151 and 0.151 respectively at 0.0625-degree map). The test used a simplified version of MODE analysis, which only considered centroid distance. The results also showed a general shorter matching distance in cu-off compared to cu-on while both models overpredicted the precipitation spatial extent. Therefore, the choice of observational data is unlikely to change the conclusion.

It is known that precipitation forecast is sensitive to the different cumulus schemes applied because of their different closure assumptions and scale considerations (Wang and Seaman 1997). The UW scheme (a convective inhibition based scheme) is found to produce deeper daily PBL growth, triggers shallower development of clouds compared to Zhang-McFarlane scheme (a convective available potential energy based scheme) (Williams, 2019) and reduce the precipitation compared to native shallow scheme in G3D (Iguchi et al. 2017). Research of Iguchi et al. (2017) also shows more negative daily precipitation bias in GW model compared to models using the new simplified Arakawa–Schubert scheme (NSAS; Han and Pan, 2011), new Kain–Fritsch scheme (NKF; Kain, 2004) and Betts–Miller–Janjic´ scheme (BMJ) in summer Central Plain. This indicates that excessive precipitation is a common problem with these cumulus schemes applied in the Central Plains and thus may aggravate the wet bias in this region. However, there are also other scale-aware cumulus schemes under development that provide promising results. Kwon and Hong (2017) introduced three aspects of scale-aware dependency into simplified Arakawa–Schubert scheme (GSAS) and found it outperforms precipitation prediction in no-cumulus simulation at both 3 km and 1 km scale in South Korea. The main contribution of the improvement in their study comes from including scale-dependency into cloud-base mass flux. Therefore, it is still probable to see improvements using scale-aware cumulus schemes in the future.

2.5 Summary

This chapter evaluates the precipitation forecast skill in NU-WRF considering two configuration impacts in terms of model resolution and the use of cumulus parameterization. The two impacts are evaluated separately, and little improvement is found with increasing model resolution. It may be due to the domain region (small elevation variation) and model configuration (the use of GW scheme and nudging) which could restrict or reduce the difference. The use of GW cumulus scheme produced a slightly wetter environment and is found to be more influential on model prediction than using different model resolutions. The cu-off model produced better precipitation pattern than cu-on although it shows a large inaccuracy especially in a grid-to-grid evaluation. The advantage of the no-cumulus scheme model should become more obvious and more accurately represent the land surface spatial heterogeneity with finer temporal and spatial resolutions (such as 1 km). Summarizing all information above, cu-off at 4km is considered to provide the best precipitation prediction. It is then chosen as the optimal configuration for later analysis in chapter 3 and 4. This chapter also shows some interesting model patterns such as the widespread but less frequent and more intense precipitation, which indicating a possible obstacle to trigger precipitation and a preference for deep convection. The possible causes of these patterns were not all tested but results in chapter 3 may help to partly explain it.

Chapter 3: Different Precipitation in a drought evolution

In the Central Great Plain, MCSs and LLJs have large impacts on precipitation and are especially prevalent during the nighttime. Considering their importance and the large contribution to regional precipitation, it is important to identify different drivers of precipitation in order to distinguish and analyze the local and non-local processes and their representation within model simulations. MCS and LLJ are then representative as non-local impacts and are analyzed with local precipitation to quantify their relative contributions during the 2018 drought. The analysis focuses on the role and drivers of precipitation during the drought evolution as well as the role of soil moisture conditions and their representation in coupled land-atmosphere models. It should be noted that the term 'local' here represents the absence of MCS and LLJ and may include other large-scale impacts (e.g. ENSO). These large-scale impacts are not easily disentangled from quantifying the precipitation, and their impacts are assumed evenly distributed in the chosen small study area (ROI of 37°-43°N and 91°-100°W in Fig. 3-1a). The analysis in this chapter is based on a model simulation (NASA Unified Weather Research and Forecast, Peters-Lidard et al. 2015) and a composite reference dataset including radar, reanalysis and an uncoupled (land-only) Land Information System model (LIS, Kumar et al., 2006)**.**

3.1 Datasets

3.1.1 ARM MCS Data

The Atmospheric Radiation Measurement (ARM) MCS database has a high spatial resolution of 4 km and covers most of CONUS east of Rocky Mountains. MCSs in this dataset are identified based on NASA Global MergedIR infrared brightness temperature and GridRad mosaic 3D Next-Generation Radar (NEXRAD) data and tracked using FLEXTRKR algorithm (Feng et al. 2018). The details of the data processing method can be found in Feng et al. (2019). Five warm-season

(2012-2016 May-Oct) ARM MCS data are used in this study to train and test MCS identification method in Section 3.2.2.

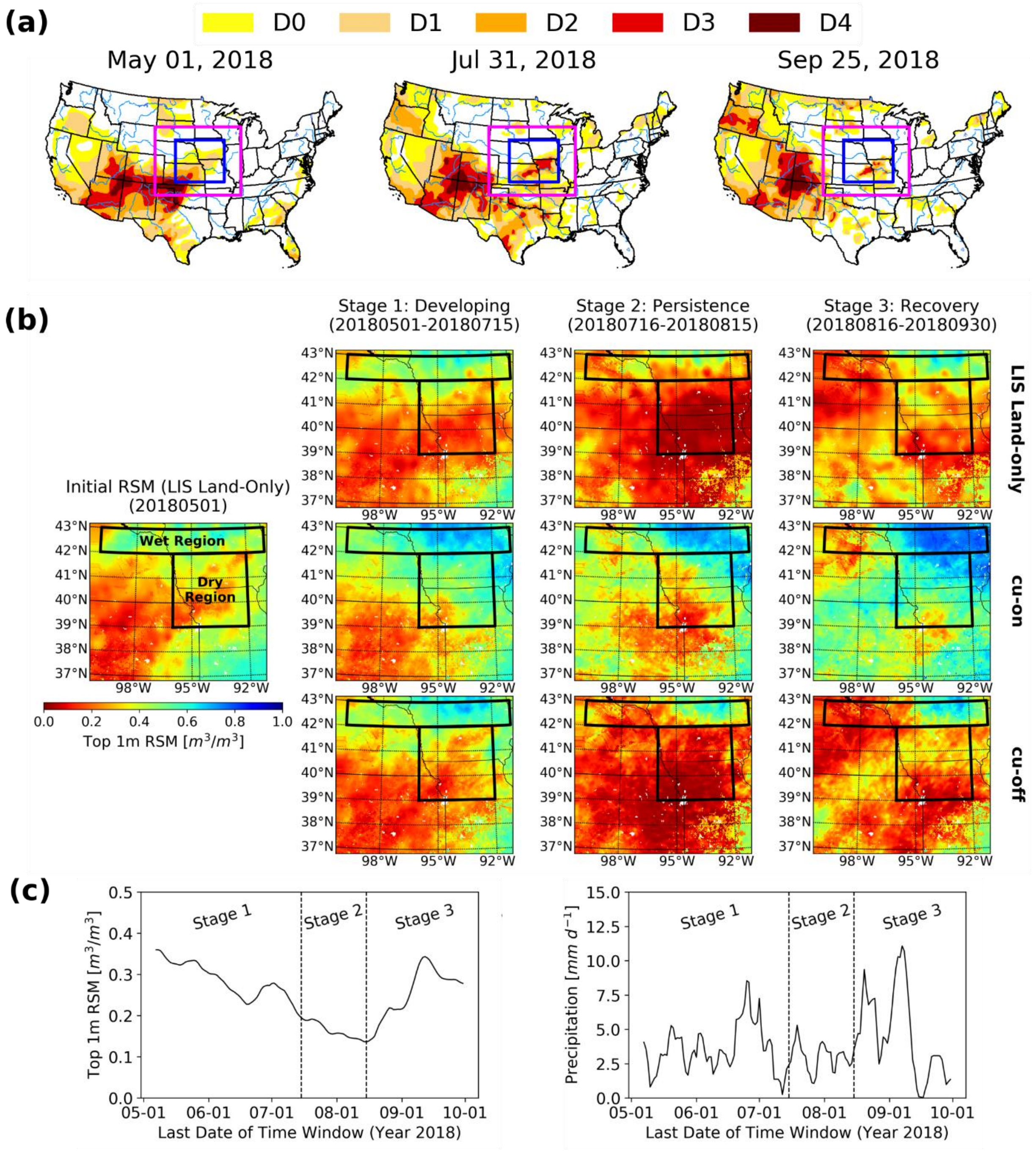

Figure 3-1:
Drought evolution of the study area: (a) U.S. drought monitor with representative dates in three drought stages. The pink outline is the model running domain and blue outline is the region of interest (ROI (b)). (b) Top 1-m relative soil moisture at initial time and the average condition of the models in the three drought stages with outlined wet and dry regions. (c) 7-day (moving window) LIS average top 1-m relative soil moisture and precipitation in the ROI.

3.1.2 IEM Radar Reflectivity

Iowa Environmental Mesonet (IEM, https://mesonet.agron.iastate.edu) generated mosaic NEXRAD (Level 3) base reflectivity (N0Q) of U.S. This mosaic product has 5-min intervals and spatial resolution of ~1 km. The increment of the reflectivity is 1 dBZ, which gives a smoother transition than abrupt class jump of 5 dBZ in N0R product. This data also removed anomalous clutter propagation and suspected false echoes using radar echo tops. Due to the fine resolution, this product was first regrided to a 4-km map as consistent with the NU-WRF model. The regrided reflectivity of 2012-2016 May-Oct were used together with ARM MCS data to build and test MCS identification method. Then the method is applied onto 2018 reflectivity as reference to compare with model results. Although this product has a high frequency of every 5 minutes, only data with an interval of an hour are used to build MCS identification method so that the timestep is consistent with model output.

3.1.3 MERRA-2 Low Level Jets

The LLJ data is provided by the Ferguson group who identified and classified coupled LLJ (CLLJ, when LLJ is coupled with upper level jet) and uncoupled LLJ (UCLLJ) based on Bonner-Whiteman classification (Bonner 1968; Whiteman et al. 1997) and analysis of local Finite-Amplitude Wave Activity (Huang and Nakamura 2016) using MERRA-2 at 0600 UTC during the drought period. The coupled LLJ is defined when it is associated with the trough-ridge structure and the uncoupled LLJ is underneath an upper-level ridge or a zonal flow. More details of LLJ identification can be found in Burrows et al. (2019) and Ferguson et al. (2020). Although the MERRA-2 data has a resolution of $0.5^{o}x0.625^{o}$, the accuracy of LLJ classification is at ~125 km due to the applied wave-amplitude thresholds used in Burrows et al. (2019) on 125-km European Centre for Medium-Range Weather Forecasts Coupled Earth Reanalysis of the twentieth century

(CERA-20 C). The MERRA-2 defined LLJs were downscaled to 4 km before analysis. Because of the small domain in this study, it is difficult to identify the complete synoptic structures from model simulations. Meanwhile, the coupled models use spectral nudging which ‘assimilate’ upper-level wind. Therefore, the MERRA-2 LLJs are used as the only source of identified LLJs in this study and considered to be the same in both reference and the model.

Table 3-1:
Model configuration

Model	Resolution	Nudging	Cumulus scheme	Boundary layer scheme	Forcing
cu-on	4 km	600 km	G3D and UW	MYJ	MERRA-2
cu-off			None		
LIS Land-only		uncoupled			NLDAS-2

3.1.4 NU-WRF and LIS Land-only Model

In this study, two sets of NU-WRF simulations -- cu-off and cu-on are used. Configurations of the two coupled models (Table 3-1) are nearly the same as the previous study in chapter 2, which showed a more realistic spatial precipitation in cu-off. The only difference is the spectral nudging (for upper-level wind, geopotential height and temperature), which varies with the domain size and was set to 600 km in this study (800 km in chapter 2). A spin-up of LIS land-only (uncoupled) model was run using forcing of NLDAS-2 from 1979 to 2018 May 1st, 0000 UTC, followed by the two NU-WRF runs till the end of September. The LIS Land-only model was also continued to run after the spin-up for the same period till the end of September as reference for precipitation (downscaled from NLDAS-2) and surface relating variables (e.g. soil moisture, sensible heat flux, latent heat flux, net radiation at surface). The cu-on is first used to see if it can simulate reasonable MCSs and if it does, how well it performs during a drought. A simple MCS verification in cu-on and cu-off have been presented in Section 3.2.2, and the cu-on is found unable to simulate MCS occurrence and is exclude from later drought analysis. All hourly model outputs are aggregated into daily data for precipitation analysis.

3.2 Method

3.2.1 Overview

The study period for the 2018 drought was chosen from May to September based on USDM. The 2018 drought in Central Great Plains emerged as a result an expansion of the southwestern drought which began in the winter of 2017. May was selected as the first month of the analysis for two reasons. The first reason was that May is the beginning of the warm season when local L-A interactions are expected to play a stronger role due to increased solar radiation. The second reason is that during the month of May the drought over the Great Plains began to peel off from the southwestern drought region and developed into its own extreme drought core (D3 in USDM) from May to August (Fig. 3-1a). Although there is still plenty of precipitation during the five months, the soil moisture is very dry with percentiles less than 50 for most of time, especially before mid-August (Fig. 3-2). To analyze the drought, two coupled models (cu-on and cu-off) and an uncoupled model (LIS land-only) were run over the study region. The LIS simulation is used as reference for Land-Atmosphere (L-A) analysis during the drought period and was used to create the initial states in the coupled model runs (see Section 3.1.4. for more details).

The 2018 drought period is split into 3 stages based on the 7-day average top-1m relative soil moisture (RSM, Fig. 3-1b-c) in LIS: 1) developing stage (May 1 – July 15, 76 days); 2) persistence stage (July 16 – Aug 15, 31 days); 3) recovery stage (Aug 16 – Sep 30, 46 days). The RSM is the available portion of soil moisture above the wilting point divided by maximum available soil moisture above the wilting point (equation 3-1).

$$RSM = (SM_c - SM_w)/(SM_{max} - SM_w) \tag{3-1}$$

Here, SM_c is the soil moisture content, SM_w is the wilting point and SM_{max} is the maximum soil moisture achievable. The RSM provides a good indicator of drought spatially as it accounts for the difference in soil textures and types through the maximum (SM_{max}) and wilting point (SM_w) soil moisture. The 7-day average RSM over the study area is used in this study instead of any standard drought indices because RSM can show the continuous change and comparison in real-time conditions rather than relative abnormal levels. Since this is not a multi-year study nor a global analysis which covers different climate regions, the use of absolute values can help to understand the change in time series for the region. July 15 and August 15 are chosen as stage separation dates when 7-day top 1-m RSM mean fell below 0.2 and when RSM started to continuously recover from the low trough. Although the drought does not completely vanish by the end of September, the RSM is recovered to a similar level as in May. This stage separation is also consistent with 7-day average precipitation in Fig. 3-1c. A wet and dry region are then defined for comparison based on the average RSM spatial pattern on May 1st (Fig. 3-1b). Figure 3-2 shows the dry region is nearly below 20th percentile before mid-August whereas the wet region is nearly above the 50th percentile for the whole period.

To identify MCS events during the drought event, a 2-filter method based on machine-learning is used to identify MCSs using radar reflectivity. This method is revised from Haberlie and Ashley (2018b,a, 2019) (see Section 3.2.2. for more details) and is applied to identify MCSs in coupled models and in IEM data, and together with a LLJ identification method based on low level wind speed and cyclonic/anticyclonic local wave activity (Burrows et al. 2019; Ferguson et al. 2020) using MERRA-2 at 0600 UTC to classify precipitation types for 2018 drought.

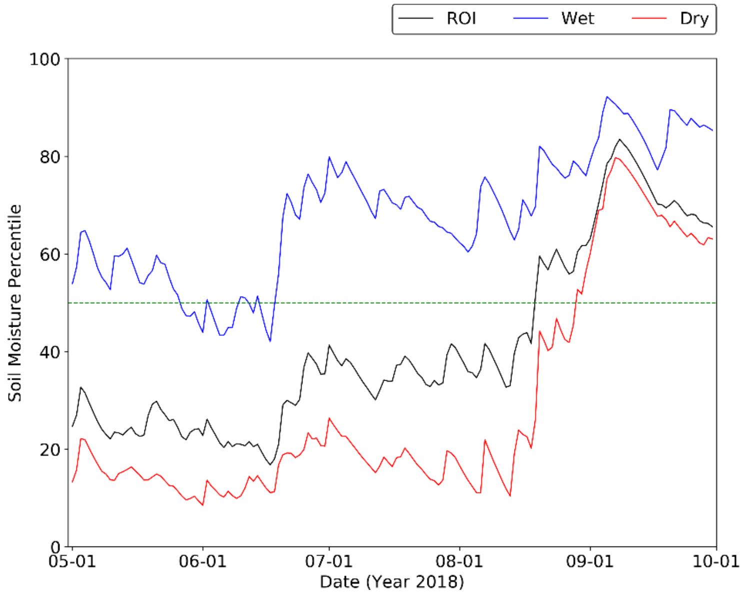

Figure 3-2:
LIS soil moisture percentile compared to its climatology. For everyday from 2018 May to Sep, the percentile is calculated compared to the nearest 2 weeks (one week before and after) in historical years from 1979 to 2017. The dashed green line shows the 50th percentile. The black line shows the inner interest domain (ROI) as blue box region in Fig. 3-1a. The blue and red lines are average percentiles of wet and dry regions respectively.

Precipitation is classified into 4 categories separating the local and non-local events: 1) MCS impacted precipitation (MCSs cover at least 10% of the region); 2) LLJ-impacted precipitation (LLJs cover at least 10% of the region); 3) MCS-LLJ impacted precipitation (both MCS and LLJ cover at least 10% of the region although not necessarily overlapping) and 4) local precipitation (LC, precipitation that is not classified as MCS or LLJ impacted). The threshold of 10% is chosen to balance the area difference between the wet and dry region and it is approximately the minimum MCS size requirement (90~100 km × 90~100 km area in the wet and dry regions). MCSs and LLJs are prevalent at night which usually peak around midnight (0600 UTC) and die out before the noon in the Central U.S (Bonner 1968; Carbone et al. 2002; Carbone and Tuttle 2008; Wang and Chen 2009; Berg et al. 2015). A similar pattern is also found in the climatology in the study region (Fig. 3-3a). Therefore, the time of 1800 UTC (12 CST) is chosen to separate the daily impact of MCSs and LLJs. If MCS- or (and) LLJ-impact precipitation is (are) found at any hour within a day (LLJ only identified at 0600 UTC), it’s considered as an MCS- or (and) LLJ-impact day. The frequency and intensity of different types of precipitation are then compared at all stages and between wet and dry regions to quantify their contributions. The model performance is assessed based on its accuracy identifying daily status of precipitation, MCS-impacted and LLJ-impacted. The soil moisture-precipitation process is then analyzed to understand the model inaccuracies. Lastly, a time lag analysis is performed on the LLJ classification to illustrate its influence on precipitation.

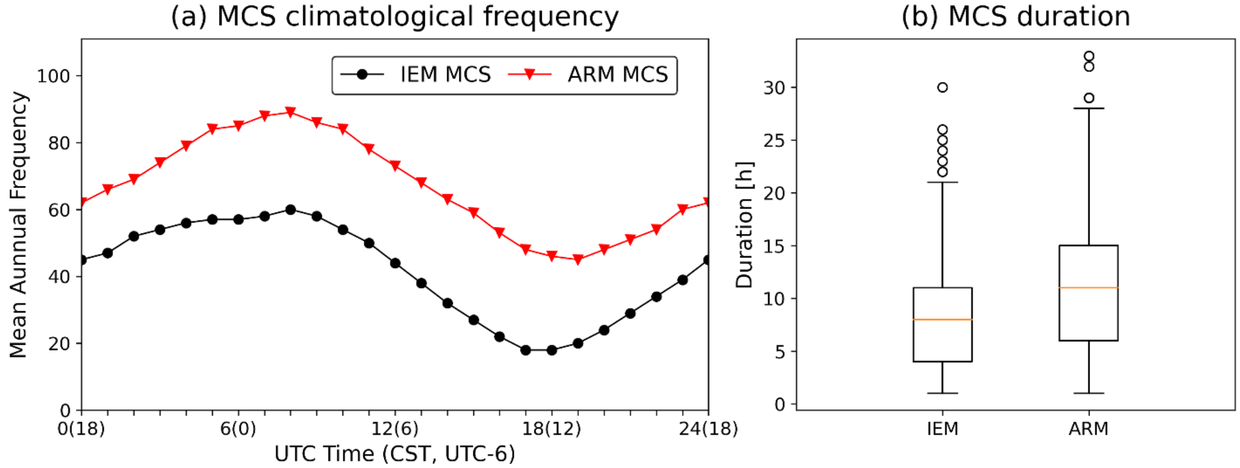

Figure 3-3: (a) Mean annual frequency and (b) duration of MCSs in ROI climatology
(a) Mean annual frequency and (b) duration of MCSs in ROI (blue region in Fig. 3-1a) climatology (2012-2016 May-Oct). The duration less than 3 hours is caused by the cut-off effects that MCSs are identified in a larger running domain (pink region in Fig. 3-1a) whereas the analysis region (ROI) is a subset.

3.2.2 MCS Identification

There are many different methods for classifying an MCS event (Parker and Johnson 2000; Schumacher and Johnson 2005; Hane et al. 2008; Coniglio et al. 2010) but all of them rely on a specific measure whether or not a certain threshold of the storm intensity and a certain duration time is exceeded. The MCSs in this study are defined as convective system with a scale exceeding 100 km for at least 3 hours as definition in Parker and Johnson (2000), and are identified in a 2-filter algorithm revised from Haberlie and Ashley (2018a,b, 2019). The steps used to identify MCSs are given as below.

1) The first step is identifying potential MCS slices using IEM radar reflectivity. For all hours, nearby convective regions (≥40dBZ) exceeding an area of $48km^2$ (different from $40km^2$ in Haberlie and Ashley (2019) due to different data resolutions) contained at least one intense cell (≥50dBZ) inside are merged within a radius of 24 km. The major axes of the merged convective regions are then checked to be at least 100 km to meet the requirement of MCS scale. Then the wider stratiform regions (≥20dBZ) with any merged convective regions inside are identified as potential MCS slices. These slices are the possible MCS precipitation regions. Next, fourteen slice features, same as in Haberlie and Ashley (2018a) are calculated including area, solidity, intense area, minor axis length, convex area, intense-stratiform ratio, convection area, convection-stratiform ratio, intensity variance, major axis length, mean intensity, eccentricity, intense-convection ratio and max intensity.
2) The second step is to create potential MCS tracks. The tracking method used in this study is based on the tracking method in Haberlie and Ashley (2018b) who used a 14-dimensional Euclidean distance between overlapped MCS slice features from step 1 to find the optimal matching MCS slice in the next time step. In their study, all overlapped slices are compared with a timestep of 15 minutes. In contrast, the reference (ARM dataset, see Section 3.1.1) MCSs use 50% as an overlap threshold on 30 min interval inferred brightness temperature for tracking (Feng et al. 2018). To be more consistent with our reference, the overlap ratio is set to be at least 20% considering the coarser temporal resolution in the model simulation (hourly). Meanwhile, the matching algorithm is revised from a one-to-one matching in Haberlie and Ashley's study to a multiple-to-one matching algorithm. All slices matching to the same slice in next time step are considered to belong to the same MCS development. This algorithm allows tracking MCS movement back to its origin and reduces MCS miss classification from

underestimating their durations. However, to avoid overestimating the duration, only one of the slices splitting from the same MCS with the most similarity is considered to be matched. Each MCS duration was then checked to ensure a duration of at least 3 hours.

3) The third step creates a 2-filter threshold algorithm to identify MCSs based on machine learning. Previous processed MCSs are not considered as final MCSs because other weather systems which have similar scale structures might be misinterpreted as MCSs slices. To reduce misinterpretation, Haberlie and Ashley applied machine learning method 'correcting' MCS slices based on their 14 features after step 1. In contrasts, in this study, the machine learning method is used to apply in the last step because the uncertainty of training slices previously could be brought into later tracking process. The machine learning method used for the final identification is 'Gradient Boosting' (Friedman 2001; Hastie et al. 2009) which was used to train MCSs in a 'leave-one-year' cross-validation for historical IEM data from May to October in 2012-2016. The Gradient Boosting (GB) method was selected because it performed well at identifying MCSs in Haberlie and Ashley's study. The parameters in the GB method are set to be the same as in their best performance in Haberlie and Ashley's study (n_estimators=1000, learning_rate=0.1) which produced an average Heidke skill score of 0.93 for 8 years testing. The GB classifier can be easily applied using a Python library 'scikit-learn' (http://scikit-learn.org). The GB classifier requires a training data set and the initial plan was to use the Atmospheric Radiation Measurement (ARM) MCS database (Feng et al. 2018, 2019) as a reference. However, because the ARM data uses a longer required duration (≥ 6 hours) to define MCSs, it was not reasonable to directly reference it to train the MCS slices. The inconsistent MCS definition increases the uncertainty in MCS training and makes the theoretically highest testing accuracy to an unknow value below 100%. To solve this problem,

A new reference pool is built consisting of all slices from their respective MCS tracks if they overlapped with ARM MCSs at any time step. The new reference pool is then used to iteratively train and test historical data in a cross-validation framework. For each iteration, two thresholds are used to define MCSs. The first threshold (Th1) is used on probability predicted by GB classifier verifying MCS slices, above which can filter the non-MCS structures based on their features. The second threshold (Th2) is applied by checking the portion of slices verified as MCSs by GB classifier in each MCS track, and thus filter the tracks with too many non-MCS slices. This is an original aspect of this work and is called the 2-filter identification. It has the advantage removing misinterpreted structures while keeping the slices consistency within the reference MCS tracks. The sensitivity of the two thresholds were tested given a range of values from 0.5 to 1 with an interval of 0.05. The optimal thresholds were found to be Th1=0.65 and Th2=0.5, which produced an average accuracy of 88.5% from the five iterative tests. Figure 3-3 verifies the 2-filter method can produce reasonable MCS frequency in diurnal cycles and durations for 2012-2016 reference time period. The discrepancies in frequency and durations in IEM MCSs are caused by different MCSs definitions and identification algorithms from ARM dataset. The best training years are found to be a composite of 2012 and 2014-2016. These optimal settings are then applied on 2018 IEM data and NU-WRF simulations to identify the reference and model MCSs separately.

The number of MCSs produced by the cu-on, cu-off models and the reference data set are shown in Figure 3-4. Compared with cu-off, cu-on largely underestimate MCS frequency and durations. Although the cu-on MCS precipitation is about 1.12 mm h^{-1} more intense than cu-off (not shown), the low MCS frequency cannot explain the largely wetter soil during the drought (Fig. 3-1b). This indicates the overestimation of local precipitation in cu-on which is consistent with previous finding in chapter 2 (Zhang et al. 2021) that cu-on tends to overestimate light rain both in frequency and space. It is clear that cu-on does not show skill generating reasonable MCSs and thus is excluded from the remaining drought analysis. As a contrast, cu-off shows a similar MCS diurnal pattern and duration as in IEM, although it also underestimates nocturnal MCSs largely. Therefore, only cu-off analysis is present as coupled model result in Section 3.3.

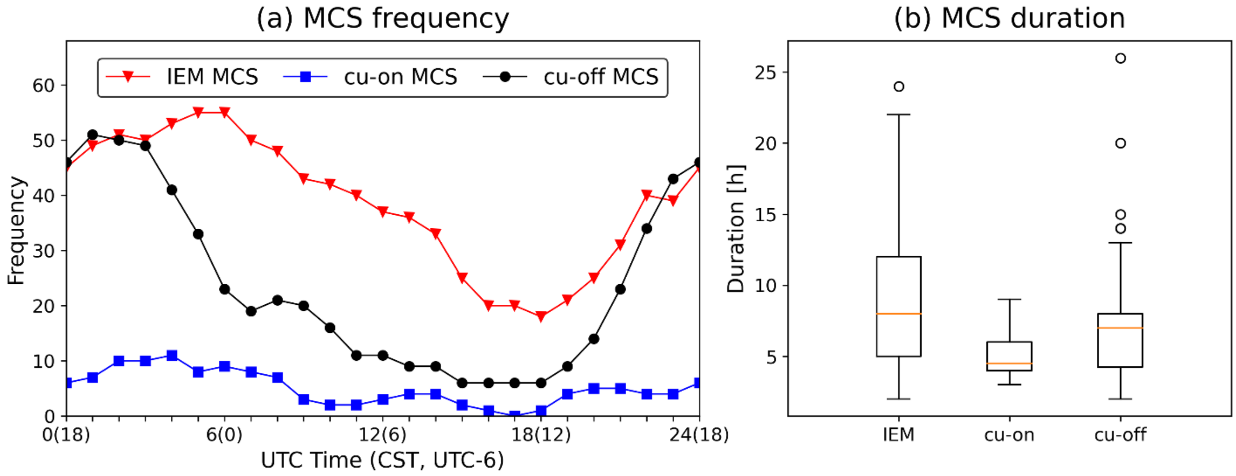

Figure 3-4:
Diurnal MCS frequency and duration of 2018 May-Sep in ROI

3.3 Results

3.3.1 Contribution of Different Precipitation Types in Reference

The LLJ-impact (green), MCS-impact (orange), precipitation days (blue; ≥1 mm d^{-1}), and precipitation intensity (color bar) in both the wet and dry regions are shown in Figure 3-5. LLJ and MCS are largely distributed during the whole period. Consistent with the 3 drought stages, MCS and LLJ sparsely occur in stage 2 (driest period, Jul 15-Aug 15) compared to other times, indicating there is a large contribution to the precipitation. Due to the larger zonal coverage in wet region, days with LLJ impact in the wet region without affecting the dry region means the LLJ mainly pass the western parts of the domain. To clearly show the impact of MCS and LLJ, the corresponding precipitation types are analyzed in terms of the frequency and intensity of precipitation in each drought stage in Figure 3-6 and 3-7. It should be noticed that the analysis here is present on a daily scale, which is different from many hourly-based analysis in past studies.

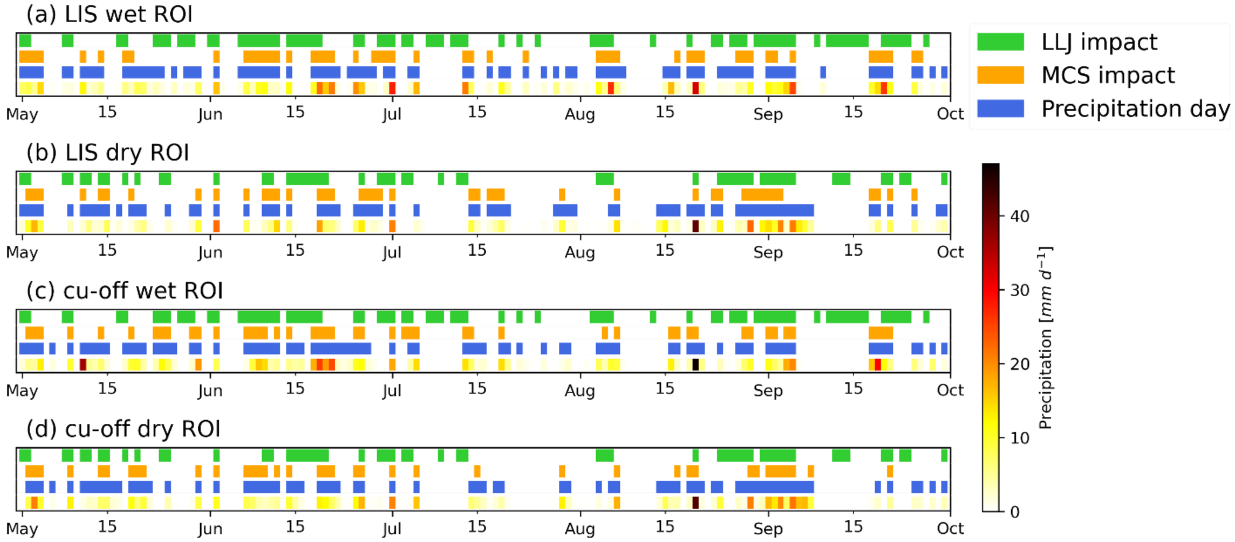

Figure 3-5:
Temporal distribution with classified precipitation types in 2018 May-Sep. Last row in each subplot is the daily precipitation. Precipitation at least 1 mm d^{-1} *is considered as a precipitation day.*

According to reference (LIS), the dominant precipitation type during this drought (May-Sep, Table 3-2) is the MCS-LLJ impact precipitation (PML), followed by MCS-impact precipitation (PMCS), local precipitation (PLC) and LLJ-impact precipitation (PLLJ) accounting for ~49%, 25-30%, 12-17% and ~10% of total precipitation respectively in wet and dry regions. The PML is the most frequent and intense precipitation type (LIS in Fig. 3-6a and Fig. 3-7a). About 17%-22% of days in stage 1 and 3 have PML, which account 41%-63% of total precipitation in each stage. As a contrast, MCSs and LLJs largely decreased in stage 2. The MCS and LLJ relating precipitation days decreased from 47% (38%) to 23% (19%) in wet (dry) region and furthered the drought persistence. The reduced MCSs and LLJs allow a clearer display of the importance of local precipitation, which is shown to be the most frequent (about 20%) precipitation type in stage 2. However, the PML was back to be the dominant precipitation in stage 3 with the return of MCSs and LLJs. The soil moisture also shows a recovery with a total precipitation of about 235 mm within 46 days in stage 3.

Table 3-2:
Contribution of different precipitation types during the 2018 drought

		Precipitation contribution^a				Total precipitation^a (mm)
	Region	PLC	PMCS	PLLJ	PML	
LIS	Wet	11.7%	29.6%	10.2%	48.4%	687.16
	Dry	16.6%	24.9%	9.4%	49.1%	541.17
cu-off	Wet	15.7%	34.8%	6.5%	43.1%	711.19
	Dry	15.8%	29.9%	6.9%	47.3%	582.08

^{a} Only precipitation days ($P \geq 1\text{mm d}^{-1}$) are taken into account

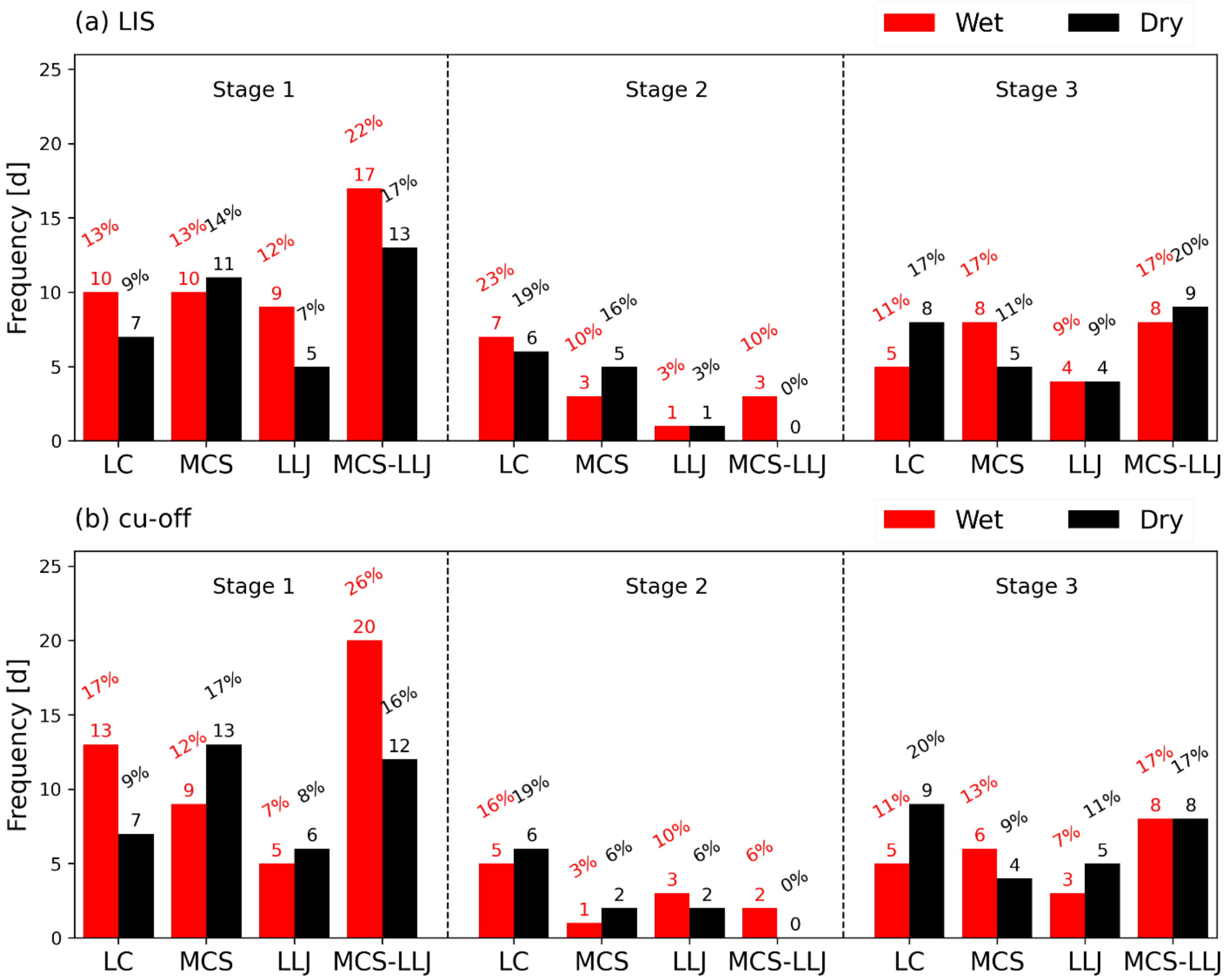

Figure 3-6:
Frequency of different precipitation types in 3 drought stages: local (LC), MCS-impact, LLJ-impact and both MCS-LLJ impact. The precipitation type is classified based on a daily timestep. The percentage values above the bar show the portion of days according to total days in each stage. The days included in the three drought stages are 76, 31 and 46 respectively.

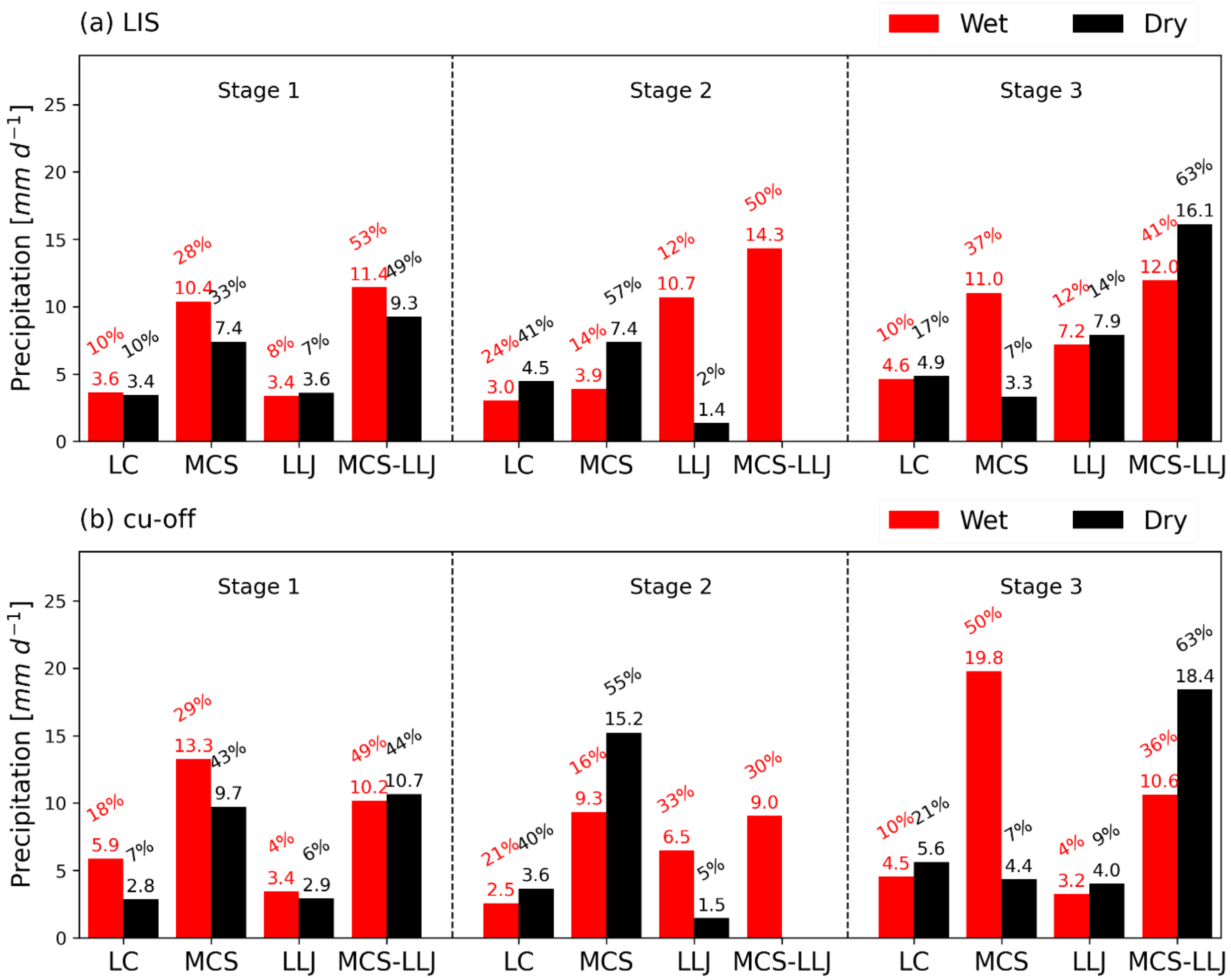

Figure 3-7:
Daily precipitation intensity for different precipitation types in the three drought stages. The intensity here is the daily average value over the wet and dry regions. The percentage values account for the portion to total precipitation (only for $P \geq 1$ mm d^{-1}) in each stage.

It is clear from Figures 3-6 and 3-7 that the MCS and LLJ classifications contribute the most precipitation during the 2018 drought. For both the wet and dry regions, the reference MCS relative precipitation (PMCS+PML) and LLJ relative precipitation (PLLJ+PML) are 74%-78% and ~59% of total precipitation (Table 3-2), which is consistent with their large contributions in many past studies. Here the MCS relative precipitation shows a bit larger contribution than the largest 70% MCS contribution in Fritsch et al. (1986) because of the coarser temporal resolution (daily) and the least 10% coverage definition for MCS impact region. This may include some periods of light rain that are not specifically defined as MCS precipitation on an hourly analysis. However, considering the small wet and dry region, it is likely that the nearby precipitation is somewhat impacted by the atmospheric environment favoring MCSs a few hours before or after. Thus, this estimate also includes indirect impacts from MCSs and LLJs and provides an upper bound estimate of the impact.

The local precipitation (PLC) is the third largest classification contributing to total precipitation, which shows a relatively stable frequency (Fig. 3-6a, 9%-23% of time in all three stages) regardless of the MCS/LLJ-impact. There is no consistent frequency preference of PLC over dry or wet region over the drought period but the dry period (stage 2) clearly shows a more frequent local precipitation (19%-23% of time) than stage 1 or stage 3 (9%-17% of time), indicating a stronger local L-A coupling during this time. Moreover, the contribution of PLC is about 24%-40% of total precipitation in stage 2 (Fig. 3-7a), which is about twice of contribution in stage 1 and 3. However, the intensity of PLC in stage 2 does not show a big difference from the other two stages. This means the majority of the increased PLC contribution in stage 2 is due to its increased precipitation frequency (percentage), and also caused by the absence of MCSs and LLJs. This highlights the role of PLC and again stress the importance of MCSs and LLJs in drought development which dominate the precipitation in this region.

3.3.2 Precipitation Interpreted in the Model

The cu-off model is found to have a good estimation of the precipitation days and reasonable skill to correctly identify the precipitation types and its intensity (Fig. 3-6 and Fig. 3-7). For both wet and dry regions, when comparing the daily precipitation status (whether it is a precipitation day), the accuracy in cu-off is about 85%. To estimate more accurately, every day is identified considering 3 aspects: (1) whether it is a precipitation day; (2) whether LLJ impact the region; (3)

whether MCS impact the region. This allows more specific classification on no precipitation days (P<1mm d^{-1}) in addition to 4 precipitation types used in the previous section. With this comparison, the cu-off is found to correctly identify 71% of daily status during the whole drought period (Fig. 3-5) and 58% of days in referenced precipitation days. Since the LLJ is considered to be the same in reference and model, the cause of daily classification difference relies on the model skill of predicting MCSs and its accuracy of predicting daily precipitation intensity (determines if it is a precipitation day). Clearly, cu-off has some deficiencies in predicting MCSs and daily precipitation. The cu-off shows some uncertainty predicting the PMCS and PML intensity that PMCS is sometimes more intense than PML whereas the reference always show the most intense precipitation in PML. Considering the lateral boundary limited by MERRA2, the cu-off model should be able to pass the moving MCSs into the domain near the boundary. However, with the overall less PMCS frequency in the model (Fig. 3-6), the higher PMCS intensity (Fig. 3-7) and the overall larger PMCS contribution (Table 3-2) indicates a reinforced influence from the local L-A interaction on simulating MCS intensity. Meanwhile, the overall PLLJ contribution is underestimated by 3% (Table 3-2) with less PLLJ intensity (Fig. 3-7), which may explain the overall underestimation of PML contribution in cu-off (Table 3-2). A more detailed analysis interpreting the LLJ impact is conducted in section 3.3.3, which helps to explain the PLLJ and PML difference.

As mentioned above, cu-off is likely to show an enhanced local L-A impacts on MCSs. In addition, chapter 2 shows the cu-off model tends to underestimate precipitation events (Table 2-4 and Fig. 2-7) which suggest a possible internal cause inhibiting precipitation triggering. These two results rise a possible explanation that there is a dry tendency in cu-off. To test whether this dry tendency exists in cu-off, daily P (precipitation)-MCS-LLJ status are compared to reference with 3 assessing categories: (1) overestimate precipitation strength (i.e. producing precipitation on no precipitation days, escalating PLC to PMCS or PLLJ to PML); (2) underestimate precipitation strength (opposite to (1)) and (3) the same forecast strength. Table 3-3 shows the portion of days in each stage that cu-off overestimate or underestimate the precipitation strength. There are more underestimation days in both regions in stage 2 and stage 3 and more overestimation days in stage 1. This seems to show an inconsistent tendency in different stages. However, considering the strong underestimation of precipitation strength in stage 2 when MCS- and LLJ-impact are largely reduced, it is possible that the dry tendency is based on a local mechanism which can be easily disturbed by MCSs and LLJs.

Table 3-3:
Difference of daily P-MCS-LLJ status in cu-off

Stage	Estimating P Strength	Wet ROI[a]	Dry ROI[a]
1	Overestimate days	19.7%	15.8%
	Underestimate days	14.5%	10.5%
2	Overestimate days	12.9%	6.5%
	Underestimate days	25.8%	19.4%
3	Overestimate days	4.3%	15.2%
	Underestimate days	15.2%	17.4%

[a] Percentage values are overestimate/underestimate precipitation strength days according to total days in each stage.

To further explore the potential dry bias in cu-off, a daily time series of variables relating to L-A interaction are analyzed. It is found that cu-off largely overestimate daytime sensible heat (SH) during the whole drought period and slightly underestimate daytime latent heat (LH) which results in a lower daytime evaporative fraction (EF; Fig. 3-8). This flux difference indicates that the boundary layer in cu-off is likely to grow higher and drier (Fig. 3-8g-h) during the day and leave a higher stable capping inversion at night, which in turn inhibit the convection on the next day and extend the dry persistence. However, this pattern can be interrupted when there is a non-local system destabilizing the boundary layer, such as transporting low level moisture into the region (e.g. MCSs and LLJs) or cooling the top of the boundary layer which weakens the capping influence and increase the vertical temperature gradience allowing low air mass to shoot over the boundary layer.

Due to the lack of atmospheric profile in reference, the assumed mechanism resulting a local dry persistence in cu-off cannot be proved directly. However, the existence of the dry persistence can be checked using Markov Chain. For any two consecutive days without MCS and LLJ impact, the precipitation status is recorded to calculate the probability of the second day (t+1) precipitation status based on the first day (t) precipitation status. Table 3-4 shows the excepted P-to-No P transition in the wet region, all other transitional probabilities to No P on second days are 2%-7% higher in cu-off, which indicates a weak dry persistence in the model. When all days are accounted with MCS and LLJ impacts, this dry persistence disappear (not shown) which agrees with previous assumption that it could be caused by a local land-atmosphere interaction in the model that are easily disrupted by meso-scale events. Although this drier persistence seems to be very weak, it could help to explain the difference identifying the daily P-MCS-LLJ status in Table 3-3. The precipitation strength is largely underestimated in stage 2 when the signal of local interaction is more obvious with less MCS and LLJ impacts. Both stage 1 and stage 3 are largely impacted by MCSs and LLJs, but the precipitation strength is generally underestimated in stage 3 whereas it is overestimated in stage 1. This may be explained by the temporal distribution of no-MCS and no-LLJ days which are more clustered in stage 3 rather than more discrete distribution in stage 1 (Fig.3-5). The longer period without MCS and LLJ impacts, the more likely the local feedback signal is obvious and reflected as an underestimation of precipitation strength.

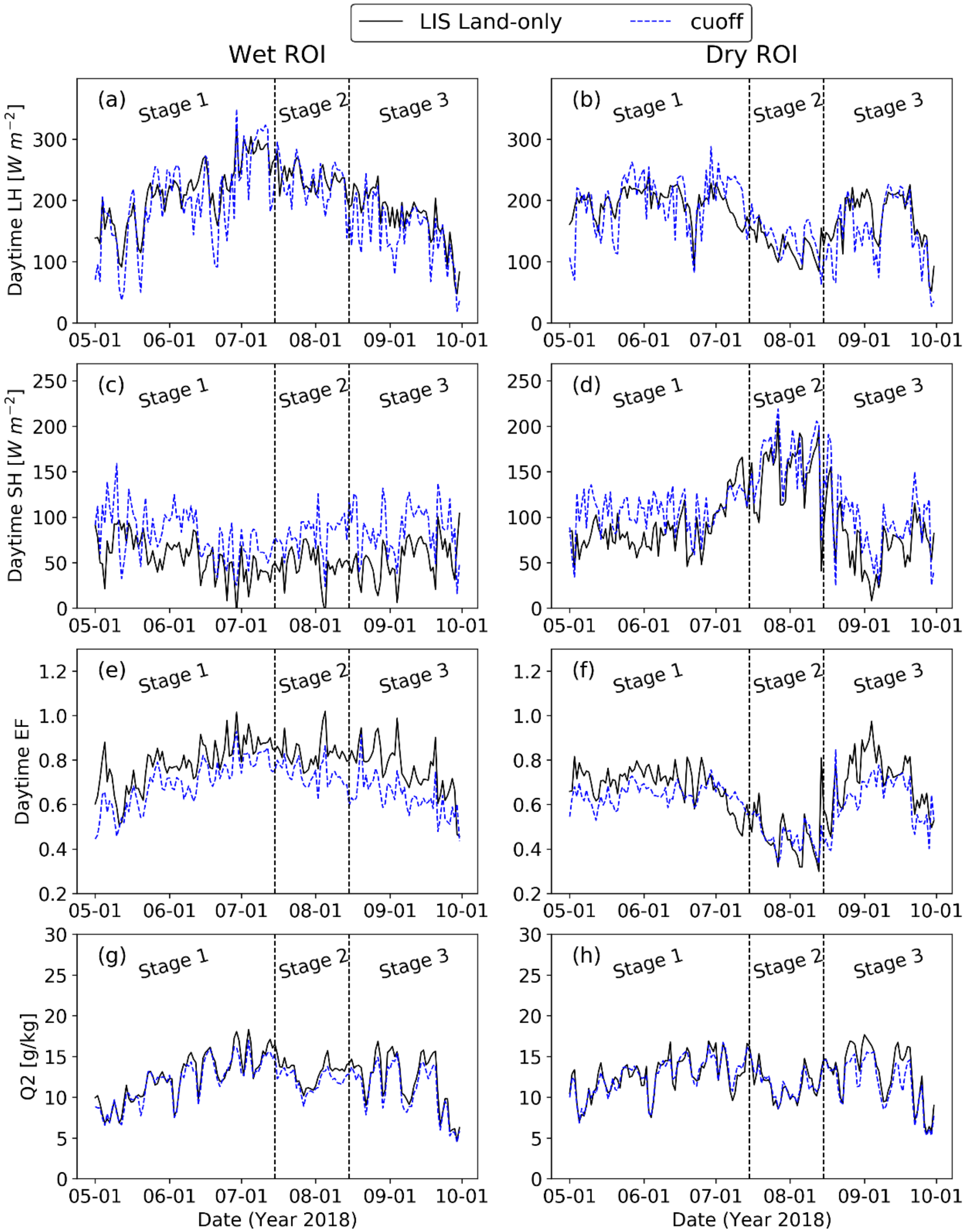

Figure 3-8:
Daytime average surface flux: (a)-(b) daytime latent heat; (c)-(d) daytime sensible heat; (e)-(f) daytime evaporative fraction (EF); and (g-h) daily 2-m vapor mixing ratio in wet and dry ROI

Table 3-4:
Markov Chain of precipitation status without MCS and LLJ impacts

			t+1 (Wet ROI)		t+1 (Dry ROI)	
			P	No P	P	No P
t	LIS	P	38.5%	61.5%	42.9%	57.1%
		No P	29.4%	70.6%	17.5%	82.5%
	cu-off	P	44.4%	55.6%	40.0%	60.0%
		No P	22.2%	77.8%	15.4%	84.6%

3.3.3 Time Lag Impact of LLJ on Precipitation

Results in section 3.3.1 shows that LLJ alone seem to have small direct contribution to precipitation. Table 3-2 shows that the most LLJ relating contributions is due to PML when MCS is incorporated with the least contribution of precipitation due to PLLJ alone (Fig. 3-6). The PLLJ intensity can has a high variability but is generally about the same magnitude as PLC (Fig. 3-7). In addition, the precipitation days impacted by LLJ in Figure 3-6 only account for 55%-60% of total LLJ occurrence in wet and dry regions for the whole drought period. These indicate that the LLJ is not a deterministic factor causing the precipitation. To understand whether and how LLJs can indirectly contribute to precipitation, an up to 6-day time lag analysis (Fig. 3-9) is conducted using Kendall’s Tau correlation between the occurrence of LLJ (LLJoc) and precipitation (Poc), the LLJ occurrence and daily precipitation (Pavg), the LLJ coverage (LLJpct) and precipitation occurrence, the LLJ coverage and daily precipitation.

All four paired correlations are similar for all time lags, and they all pass the significance test only in 1-day lag (Fig. 3-9). In the wet region, no other time lags are significant, and the 1-day lag correlation is the highest around 0.2. The lag-0 correlation is almost 0, which indicates that the LLJ impact on precipitation in the region is weak indicator for the first day but prepares the environment favoring for precipitation with 1 day in advance instead of triggering the same-day precipitation in wet region. This explains the difference of PLLJ contribution and its intensity between cu-off and the reference (Table 3-2 and Fig. 3-7) that PLLJ is not strictly relate to LLJs on the same day. Conversely, correlations in the dry region are slightly higher and are partly significant in time lags of 0, 2 and 5 days. Both reference and cu-off show significant correlation between LLJpct and Poc/Pavg on the same day (lag-0), and only LLJpct-Pavg correlation is significant in reference on the third day (lag-2). This means the dry region is more sensitive to LLJ impact. The LLJ impact to form precipitation is usually within 1-day lag, but there is a longer preservation of LLJ influence up to 2 days in advance based on the LLJ passing area which likely links the amount of importing moisture with precipitation intensity. The difference between the two regions may due to the higher sensible heat flux and the warmer air above the dry region (Fig. 3-10e-f), which produced a higher boundary layer with higher equivalent potential temperature (θ_e). When LLJ passed by, the strong wind and moist incoming air increase the instability more over dry region and allow its low-level air mass easier to reach higher altitude and trigger deeper convection. This produces a 2-5% higher chance that precipitation occurred on LLJ-impact day over the dry region. It is unclear why the correlation between LLJ occurrence and precipitation is significant on the 6th day (lag-5) at about 0.2 in dry region, but it may relate to the local L-A interaction when LLJ and MCSs are less frequent.

When comparing between cu-off and reference, the LLJ impact on precipitation is quite similar but slightly stronger in cu-off (Fig. 3-9). The lag-1 LLJ-P correlation is 0.03 (0.04) higher on average in cu-off over wet (dry) region, and there are 1-2 pairs of LLJ-P correlation passing significance test in lag-0 and lag-2 day for the dry region. Although these differences are quite small, the correlation is consistently higher in all time lags and the difference is about 0.05 (0.13) on average in wet (dry) region. This adds the confidence that the LLJ has a slightly stronger impact on precipitation in cu-off compared to the reference.

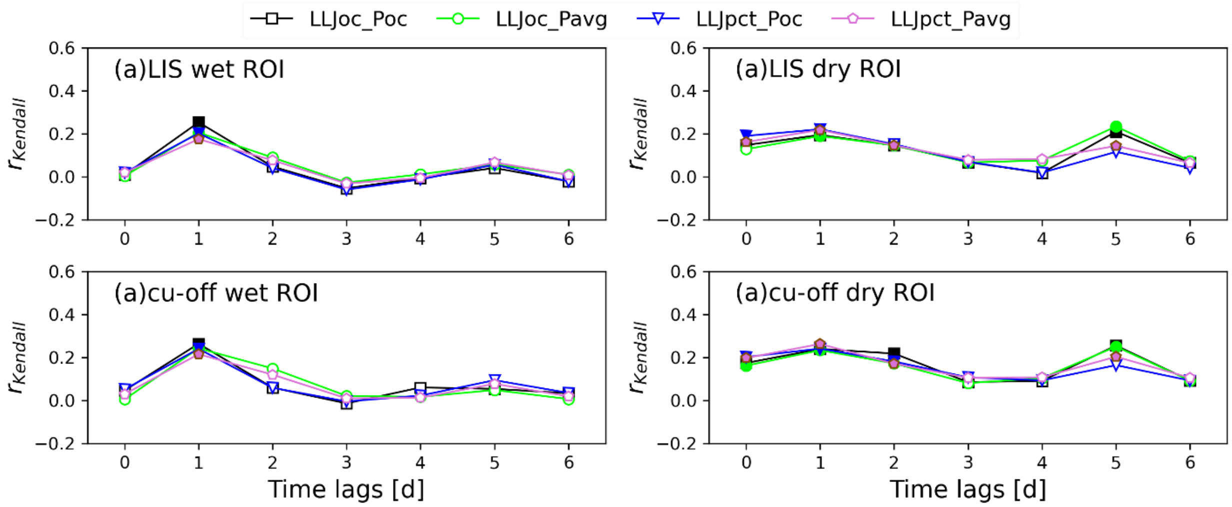

Figure 3-9:
Time lag analysis between LLJ and precipitation. Filled markers shows the significant correlation passing 5% confidence level.

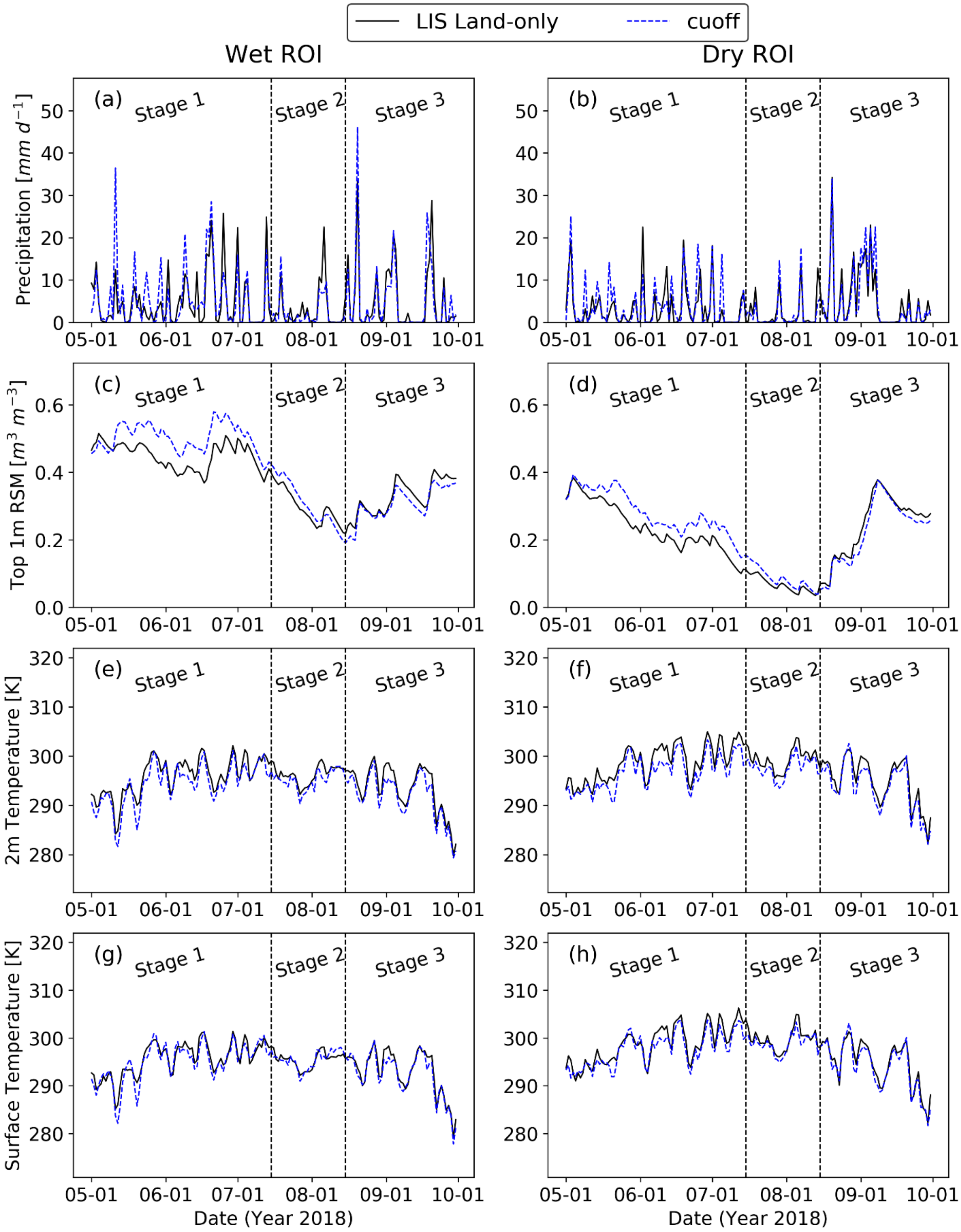

Figure 3-10:

Time series plot of (a-b) precipitation, (c-d) top 1-m relative soil moisture, (e-f) 2-m air temperature, and (g-h) surface temperature in wet and dry region

3.4 Discussion

An obvious overestimation of sensible heat flux is found in cu-off (Fig. 3-8), which could cause a drier persistence in the model. To find the cause of this large bias, the net total radiation, the net longwave and shortwave radiation as well as the surface albedo are plotted in Figure 3-11. It is obvious that the bias in sensible heat flux is mainly from the overestimation in net shortwave radiation. With the nearly perfect simulation of surface albedo (Fig. 3-11g-h), this overestimation is primarily due to the incoming shortwave. However, the bias in incoming shortwave is not the only reason causing surface flux bias. The EF in cu-off is found to have a very good fit to reference in stage 2 over dry region when net radiation is still overestimated. It is found that both latent heat and sensible heat are slightly overestimated balancing the bias in flux partitioning (Fig. 3-8a-d). As a contrast, latent heat is generally underestimated during other drought stages or in wet regions which increase the bias in flux partitioning. The larger latent heat over the dry region during stage 2 in cu-off is due to its higher remained RSM (Fig. 3-10d) when SM-ET relationship has converted from energy limited to water limited regime (EF<0.5). However, this cannot explain the underestimated latent heat for other drought stages when both RSM and net radiation are higher with a slightly lower 2-m mixing ratio (Fig. 3-8 and 3-10). One of the possible reasons is that the mechanism partitioning the surface flux in the model is different or largely dependent on a SM-relate threshold distinguishing the water-limited and energy-limited SM-ET relationship. Although to prove and test this assumption is beyond the scope of this study, a good guess of this SM-ET regime conversion is possibly lower than 0.2 in top 1-m RSM (Fig. 3-10d), which can be used for testing in the future work.

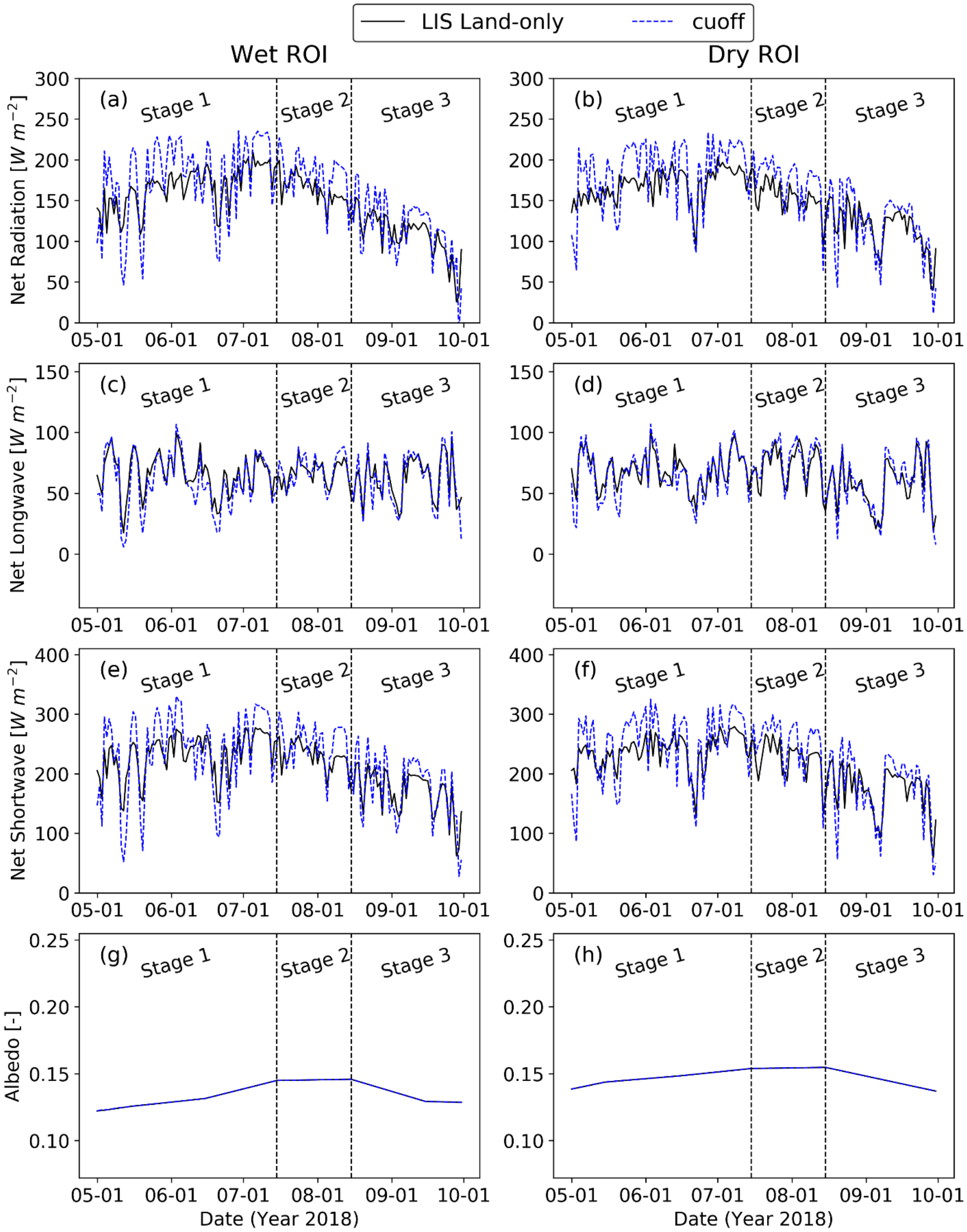

Figure 3-11:
Radiation and albedo comparison in wet and dry ROI: (a-b) Net downward radiation; (c-d) Net upward longwave radiation at surface; (e-f) Net downward shortwave radiation at surface; (g-h) surface albedo

In contrast to the common idea that stresses the importance of LLJs to bring large amounts of moisture into Great Plain, results in this study implies that the actual contribution directly from LLJ to the total precipitation may not be large. To understand the difference in LLJ impact and MCS impact, a MCS-P Kendall's Tau correlation is calculated in Figure 3-12 with 6 day time lags similar to LLJ-P correlation in Figure 3-9. Different from LLJ, MCS-P correlation is highest in lag-0 at about 0.56. Keep this in mind when considering the weak (<0.2) and partly insignificant LLJ-P correlation on the same day (lag-0), the MCS may also be the dominant factor in PML days. Most precipitation in PML is expected from MCS impact considering the PMCS contribution is more than 2 times the PLLJ contribution in both regions (Table 3-2). In addition, PML days account more than 60% of LLJ-impact precipitation days (PML+PLLJ) and about 83% of total LLJ-relating precipitation. Although it is difficult to split the contribution of MCSs and LLJs in PML, the results indicate the precipitation contributed directly from LLJ is very small. LLJ is found to work in a slower and indirect way contributing to precipitation up to 2 days ahead.

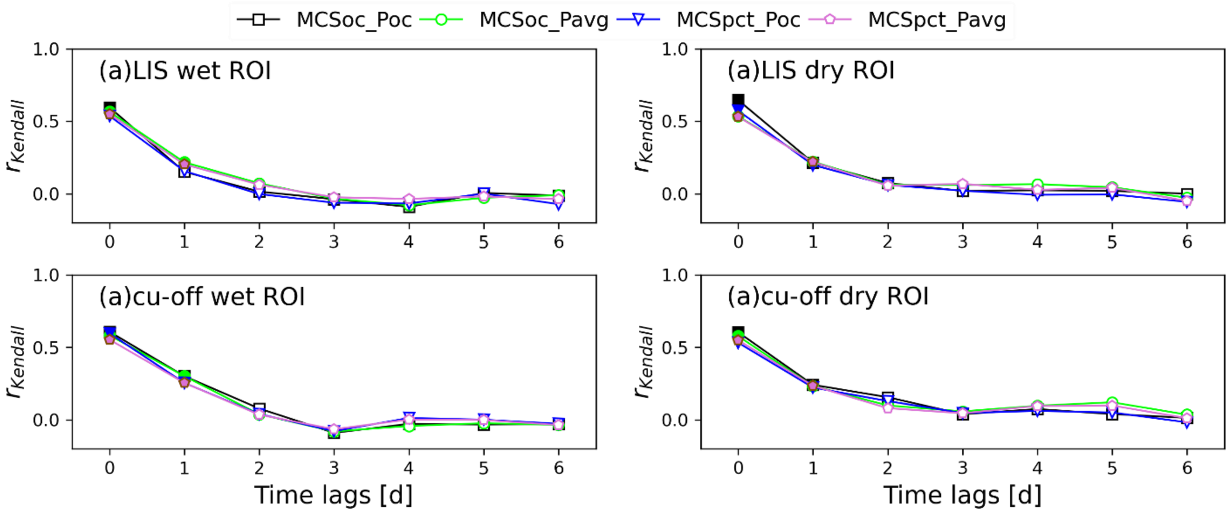

Figure 3-12:
Time lag analysis between MCS and precipitation. Filled markers show the significant correlation passing 5% confidence level.

In this study, there is uncertainty in MCS identification based on the possible inconsistent height for radar reflectivity. The radar reflectivity used in cu-off is the maximum reflectivity, which does not tell at which level it is detected, and thus could be different from reflectivity level detected in IEM (base reflectivity product which detects the lowest radar level). To test this uncertainty, reflectivity of cu-off was interpolated to 1.5 km and 2.5 km above the ground to identify the MCS as well. Figure 3-13 shows the comparison of diurnal MCS frequency. It is clear that using both 1.5km and 2.5km reflectivity would largely underestimate daily MCSs and the maximum reflectivity provides the best match. Therefore, with analysis based on the daily scale, our results should provide a good classification of daily P-MCS-LLJ status. However, Figure 3-13 shows a defect in cu-off in that it largely misses MCSs from local midnight till noon despite the chosen reflectivity height used in the classification.

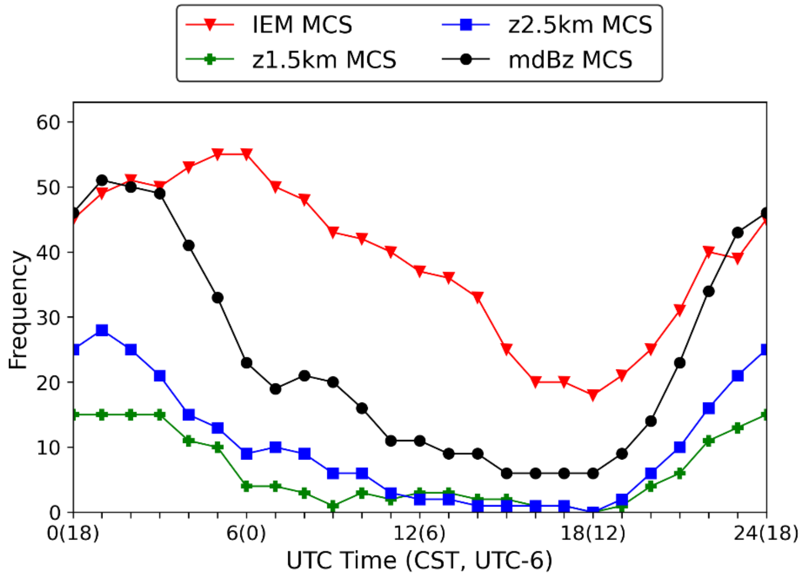

Figure 3-13:
Diurnal MCS frequency identified at different reflectivity heights

3.5 Summary

This chapter analyzed the precipitation drivers during the 2018 drought based on daily precipitation-mesoscale convective system-low level jet (P-MCS-LLJ) status and the corresponding cu-off model performance is evaluated. MCS is found to dominate the precipitation during the 2018 drought. Surprisingly, the direct LLJ influence on precipitation is small, and the large contribution in many past studies relating to LLJs is due to the MCSs which concurrently occurred and combined with LLJs on PML days. The LLJs are found to indirectly influence precipitation through providing moisture and dynamically preparing the atmospheric environment favoring for precipitation with 1-2 days in advance instead of producing same-day precipitation. The cu-off model is generally able to reproduce MCSs on the daily scale and shows a fair representative of different precipitation types and the overall changes of MCSs and LLJs during the drought evolution. However, some interesting model deficiencies are also found in this chapter. A dry persistence exists in the model because of the large overestimation of sensible heat due to the bias from incoming shortwave and inaccurate flux partitioning. In addition, the cu-off precipitation is more sensitive to MCSs and LLJs. Although the analysis in this chapter only finds a weak signal to support these two assumptions, it provides another explanation for inaccurate model forecast, such as the underestimation of precipitation events identified in chapter 2.

Chapter 4: The Role of Soil Moisture in Precipitation Formation

Previous studies have done a lot of analysis on the soil moisture – precipitation (SM-P) relationship and feedbacks (Eltahir 1998; Diro et al. 2014; Ford et al. 2015; Welty and Zeng 2018; Moon et al. 2019). The L-A interactions relating soil moisture to precipitation is very complicate due to different atmospheric environments. Thus, many studies use some simple indices such as convective triggering potential (CTP) and humidity index (HI) to distinguish different atmospheric environments and identify the favorable soil moisture condition to trigger precipitation under these environments (Findell and Eltahir 2003b,a; Ferguson and Wood 2011; Roundy and Santanello 2017; Santanello et al. 2018). However, these simple indices miss the details of the atmospheric condition and thus cannot ensure the results are not impacted by non-local scale factors. The SM-P relationship under non-local scale weather systems in past studies mostly focus on one specific meso-to-large scale system such as Mesoscale Convective System (MCS) and Low Level Jet (LLJ). There are few studies analyzing SM-P feedback under both local and non-local atmospheric environment. This gap in the research, to understand L-A interaction after teasing out the non-local system impacts motivates this study. Building off of the method in chapter 3 to identify the different precipitation days separating the MCS and LLJ impacts, allows for a further analysis to isolate local L-A interaction and to understand how the soil moisture contributes to precipitation formation under different atmospheric conditions.

4.1 Method

This chapter is builds off of the work in chapter 3 and provides further analysis of land-atmosphere (L-A) interaction based on soil moisture condition. The data used in this chapter is the same as chapter 3 with one additional model run. The additional model run was selected in order to analyze the role of soil moisture via L-A coupling during the drought. The new run was conducted by changing the initial soil conditions with the same model configuration as cu-off. The new run is hereafter called ‘cu-off_SWD’ (switching wet and dry region). The mean values of four soil properties (skin temperature, soil temperature, soil moisture and liquid soil moisture) in the wet and dry regions at the initial time (May 1, 0000 UTC) were switched first, followed by a 3-hour spin-up from 2100 UTC Apr 29 to 0000 UTC Apr 30 to ensure a complete updating of soil moisture relating properties such as albedo. The 3-hour spin-up period was chosen based on identifying a period when there was little precipitation within 15 days from May 1 at 2100 UTC to 0000 UTC. Only Apr 27-29 had little precipitation and Apr 29 provides the best match as shown in Figure 4-1. Except for skin temperature, the switched soil temperature and moisture fit well with their original initialization. The new initialized skin temperature is about 5K lower than original condition. This indicates a strong impact from the atmosphere of the chosen 3-hour spin-up period onto surface soil, which also can be seen from the slight bias for top 10cm soil conditions (L1) in Figure 4-1(b-d) compared to better matches in the deeper soil (L2-L4). The land condition after this 3-hour spin-up is then used as the new initialization for the drought period simulation from May to September. Results from this new model run (cu-off_SWD) is then compared with previous simulation of cu-off considering the different type of precipitation days.

Understanding how soil moisture affect the precipitation requires a good knowledge of when the L-A coupling is activated and how the evaporated moisture is transported and forms the precipitation. Among the variables analyzed, the lifting condensation level (LCL) is the height when near-surface unsaturated air is able to condense while rising up adiabatically. Thus, the LCL can be considered as the cloud base if the air is able to rise up to that level. The LCL deficit, which is defined as the difference between LCL and boundary layer height, is then a good indicator of when the near surface air is able to reach the LCL (LCL deficit ≤ 0) and thus trigger convection and cloud formation and possible precipitation. The cloud fraction is used in this study to present sub-grid cloudiness as a fast indicator for convection. It is from the model output using Xu and Randall's method (1996) based on relative humidity and condensate water (cloud liquid + ice) mixing ratio to approximate cloud fraction. Due to the moving air, clouds may not be generated locally. The cloud fraction is then used with precipitation, soil moisture and LCL deficit to determine if the cloud is formed locally.

For the first part of the analysis (section 4.2.1), the local precipitation days (PLC) are analyzed with respect to the basic L-A interaction and without the impacts of MCSs and LLJs. A series of SM-P relating variables and a diurnal cloud fraction profile are analyzed to build a basic understanding of when and where the local precipitation formed and the role of L-A coupling. After this, further analysis of other precipitation days: LLJ impacted precipitation (PLLJ), MCS impacted precipitation (PMCS) and both MCS and LLJ impacted precipitation (PML), are then compared with PLC days to illustrate how precipitation forms differently with LLJ and MCS impact (section 4.2.2). Results from cu-off_SWD are then compared with cu-off to understand the time when the L-A coupling is strong and how largely the soil moisture contributes to different precipitation. Lastly, a diurnal soil moisture path is plotted to summarize how soil moisture contribute to precipitation formation in the complicate real world with MCS and LLJ impacts in section 4.2.3.

4.2 Results

4.2.1 Soil Moisture Impacts on Local Precipitation Days

The cu-off_SWD only changed 16 (10.5%) and 11 (7.2%) days of P-MCS-LLJ status for the wet and dry region respectively during the whole drought period (153 days). The small change in daily precipitation (Fig. 4-2) indicates a relatively small cumulative impact of the change in soil moisture on daily precipitation and requires analyzing the L-A interactions at a finer temporal resolution to detect changes. Thus, a series of variables relating to L-A interaction on PLC days in cu-off are plotted over the average diurnal cycle in Figure 4-3 to provide a baseline for understanding L-A coupling in the dry and wet region.

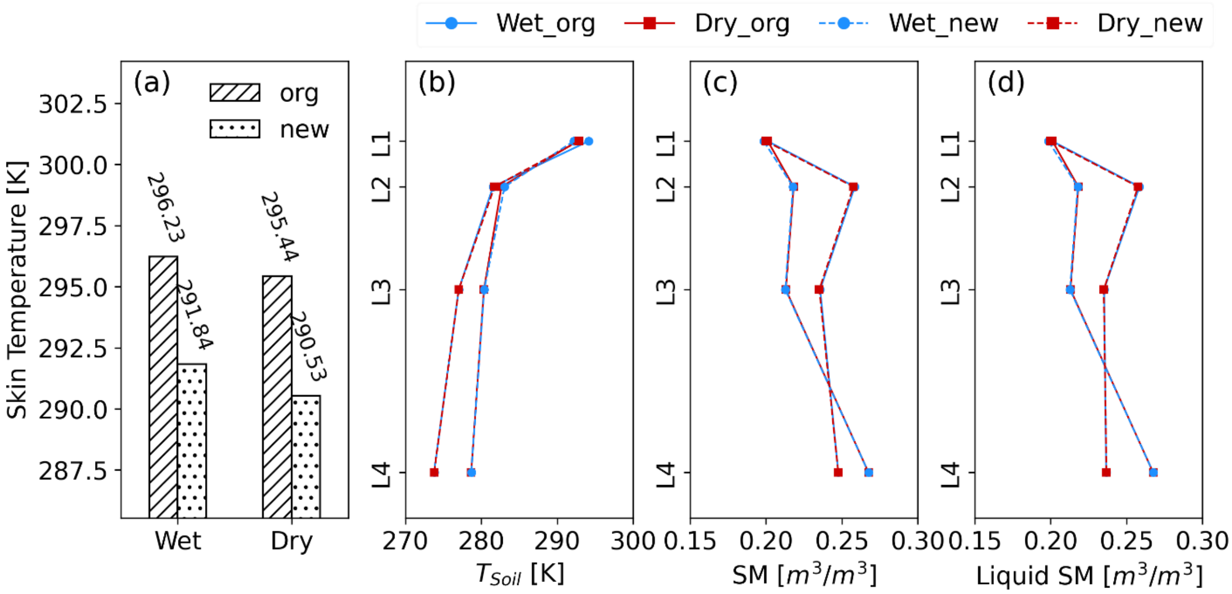

Figure 4-1:
Soil conditions before and after switching the regional mean between the wet and dry region. (a) is the skin temperature; (b) is the soil temperature; (c) is the soil moisture; (d) is the liquid soil moisture. L1-L4 refer to the soil layers from top to bottom with thickness of 10cm, 30cm, 60cm and 1m.

Figure 4-3a shows there are two precipitation periods in both the wet and dry regions: one in the afternoon (19-00 UTC) with a nearly constant intensity, and another stronger precipitation period with a peak during the night (early morning) in the wet (dry) region. For the afternoon precipitation, it is clear that it is caused by the growing boundary layer heated by the sensible heat flux allowing the evaporated moisture and pre-existing water vapor to rise up to the LCL (Fig. 4-3e-h). The negative LCL deficit falls below 0 from 1900 UTC to 2200 UTC, which matches well with the time of afternoon precipitation. However, the boundary layer is decoupled from the upper air (LCL deficit >0) before 1800 UTC and after 2200 UTC, which seems not able to explain the night or early morning precipitation.

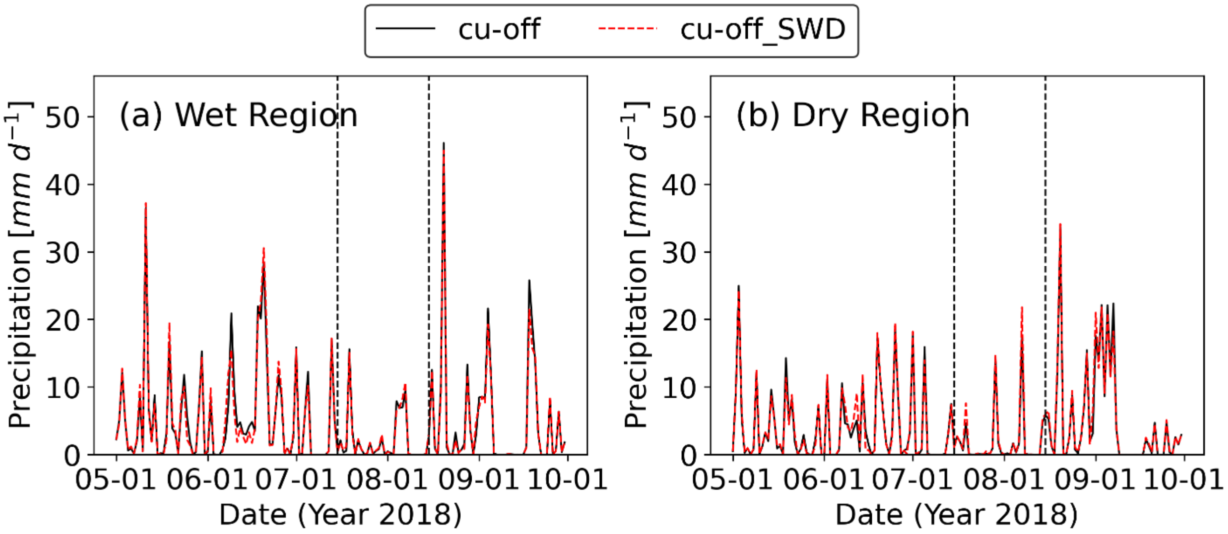

Figure 4-2:
Daily precipitation before and switch initial soil moisture in wet and dry ROI

To understand how this night-early morning precipitation is produced, the cloud fraction was analyzed. Compared to precipitation, cloud fraction has a faster response to locally triggered convection before precipitation is able to occur. Thus, it provides a more accurate time to distinguish the cause of precipitation. To better present the link between the land and cloud, an averaged diurnal cloud fraction profile is plotted in Figure 4-4a-b for PLC days. There is an increase of low-level clouds (around 900 hPa) from 1800 UTC to 2300 UTC showing the strong L-A coupling in the afternoon. For the wet region, more shallow clouds are formed in the afternoon with a longer duration compared to the dry region. This is owed to the larger evaporation (larger latent heat flux in Fig. 4-3e) over the wet soil region. There is a slow consistent increase of cloud fraction in the low level between 700 and 900 hPa during this time, indicating a small impact of the afternoon coupling. This impact can last to the evening after 0000 UTC when boundary layer and LCL are decoupled. However, without a gradual increase of cloud fraction from surface to upper levels, the deep clouds maintained and developed after the sunset (around 0000-0100 UTC) are therefore not likely caused by the local L-A interaction. Instead, it is mainly due to the cloud movement especially from west, which is the dominant wind direction in this region. This cloud moving pattern clearly affect both regions in the evening from 2200 UTC to 0800 UTC and then produces the nighttime precipitation. It should be noted that some shallow clouds started to form starting about 0300 UTC and lasted until the afternoon. Over the wet region, this shallow cloud showed a gradual increase and decrease within about 6 hours around 0600 UTC, which perfectly match with the nighttime precipitation. Therefore, the nighttime precipitation peak in the wet region is likely due to both the deep advected clouds and the shallow clouds. Although the land seems still decouple from atmosphere with LCL deficit above 300m after sunset, the decrease of LCL deficit and the nearly constant boundary layer height indicate a decrease in LCL, which means the air just above the top of boundary layer might condense with the temperature drop to form the shallow clouds. This is consistent with the larger increase in cloud fraction near 900 hPa over the wet region (5%) where the temperature is lower in the dry region (2%). In addition, the low level (850 hPa) geopotential field is also checked to see if there are other interactions. It is found that the low-pressure system is very common in or near the study region during the night (Fig. 4-5a). This strong pressure gradient accelerates the air movement, which on one hand could cause fronts to lift the warm air and form the clouds in or near the study region and make it easier for clouds to pass by the region. These commonly occurring low-pressure systems sometime work together with high pressure systems nearby and become a strong forcing to move the shallow clouds formed in nearby regions during the entire nighttime and into the morning.

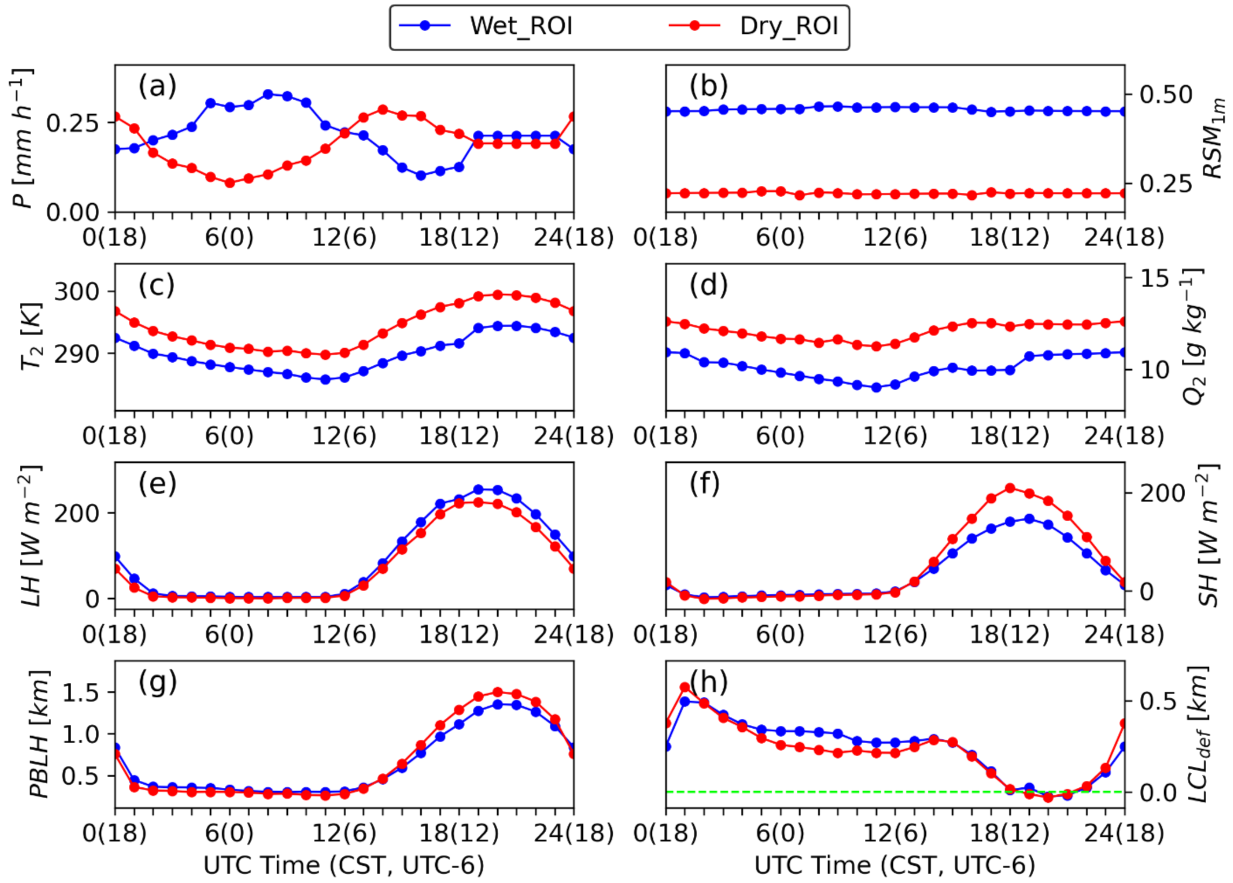

Figure 4-3:
Diurnal cycle of L-A relating variables on PLC days in cu-off: (a) hourly precipitation; (b) relative soil moisture; (c) 2m temperature; (d) 2m vapor mixing ratio; (e) latent heat flux; (f) sensible heat flux; (g) boundary layer height; (h) LCL deficit.

For the morning precipitation over the dry region, there is a connection between dry soils and an increase in clouds in the mid-to-high levels (300-500 hPa in Fig. 4-4b) from 0800 UTC to 1800 UTC. Similarly, the low-pressure system is again found but more in the middle and upper levels during this time at locations in or to the south of the dry region (Fig. 4-5b). Again, this cyclonic wind in the middle and upper levels transport or lift warm air from south into the dry region and is instrumental in forming the morning precipitation. In PLC days, these upper cyclone patterns mainly occurred in the south of the domain, which have less influence in the wet region. In addition to the upper level, there is an increase in the cloud fraction in low level from 1200 UTC to 1800

UTC in both the regions. Furthermore, considering the morning time and the same phenomenon also on other precipitation days (Fig. 4-4), these increased shallow cloud fractions are mainly due to the daytime heating and the increase in evaporation.

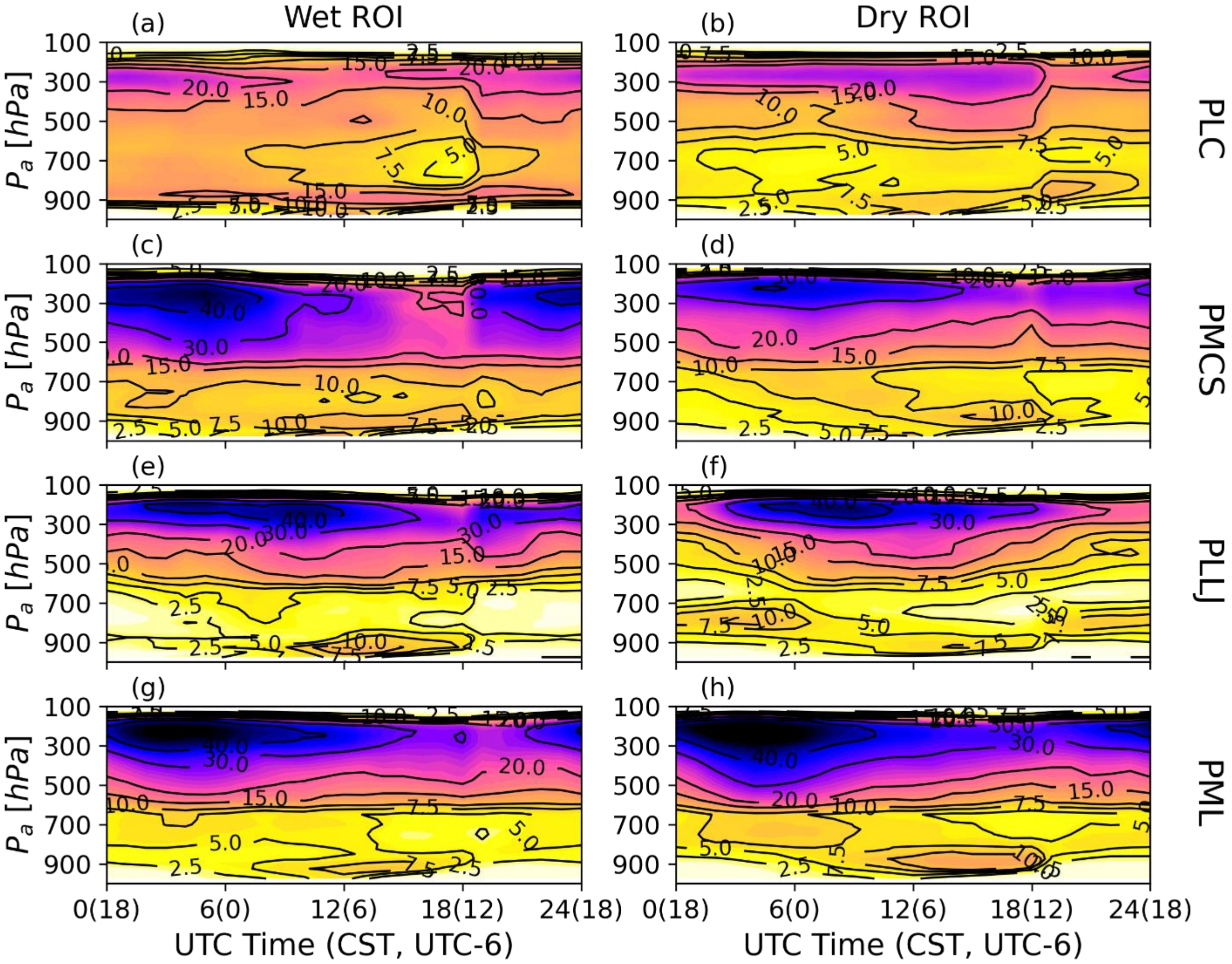

Figure 4-4:
Averaged diurnal cloud fraction profile for different precipitation days from cu-off. The filled color is the cloud fraction [%] at each level. The contours are drawn with cloud fraction of 2.5%, 5%, 7.5%, 10%, 15%, 20%, 30% and 40%.

With the cloud analysis above on PLC days, five main cloud formation patterns can be recognized from the cloud fraction profile: (1) local boundary-low level coupling caused shallow clouds in the afternoon below 700 hPa with cloud fraction less than 20%; (2) upper level clouds passed from nearby regions at 200-350 hPa levels with cloud fraction more than 20%; (3) shallow clouds formed by the temperature drop and low level pressure system during the night (0300 UTC to 1200 UTC) with cloud fraction less than 20%; (4) shallow clouds produced by daytime heating and increased evaporation in the morning (1200 UTC – 1800 UTC) with cloud fraction less than 20%; (5) middle-to-upper level cyclone caused clouds at 200-500 hPa levels with cloud fraction more than 20%. These five patterns build the basic understanding of the precipitation formation in this region.

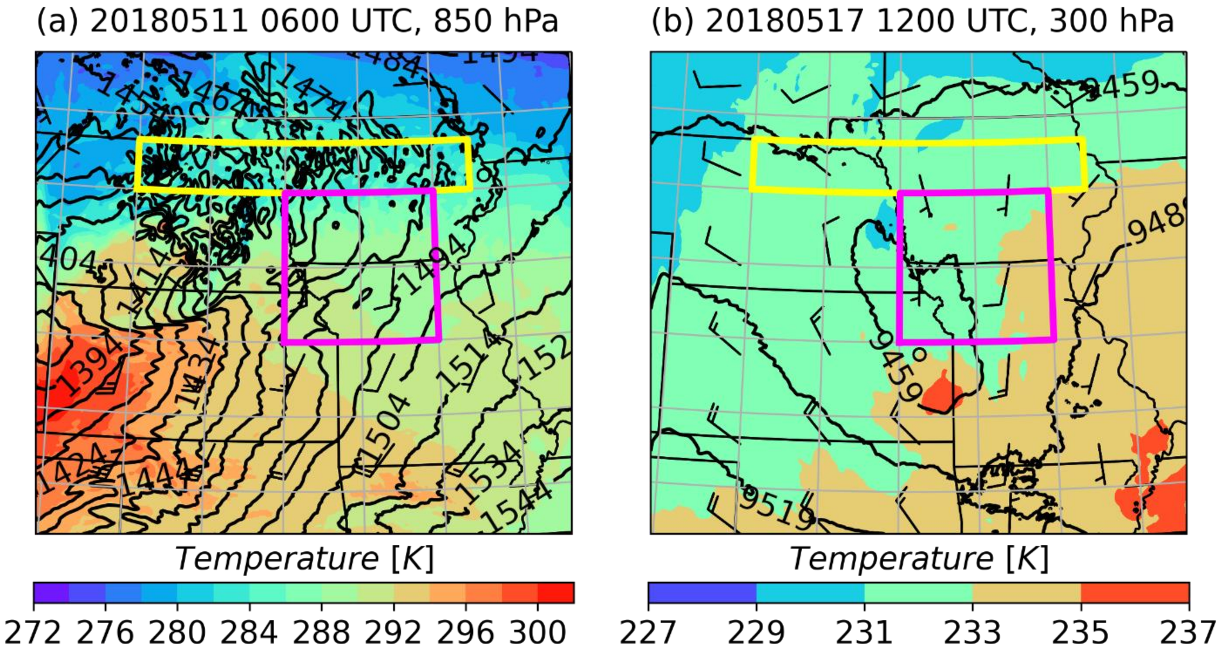
(a) 20180511 0600 UTC, 850 hPa

(b) 20180517 1200 UTC, 300 hPa

Figure 4-5:
Two examples of geopotential, wind and temperature field at 0600 UTC and 1200UTC. The contour lines show the geopotential height at given pressure level. The filled color shows the temperature contours. The purple and yellow box are the location of the dry and wet region.

4.2.2 Soil Moisture Impacts on Non-local Precipitation Days

With the five basic patterns described in previous section, it can be seen from the cloud fraction profile that the precipitation on PMCS, PLLJ and PML days all mainly controlled by stronger mid-to-upper-level cloud transport and cyclone system from evening till early morning (Fig. 4-4c-h). These upper clouds are thicker with a cloud fraction larger than 40%. It is found that many small deep L-A coupling induced convective events occurred during these days in, or near, the wet and dry regions. Figure 4-7 shows an example of a deep convection triggered in the boundary between wet and dry region. The dense pressure gradient with the small low-pressure center at the 850 hPa level and the relatively higher temperature near the same location at 300 hPa level indicates the lifting of the local air is able to reach the upper levels. These strong deep couplings are also seen with a lower LCL deficit at night, especially over dry soil (Fig. 4-6b,d,f). The LCL deficit even falls below 0 for PLLJ and PML days for the dry region, showing a preference of night L-A coupling on LLJ days. This should be explained by LLJ disturbance which bring moist entrainment into boundary layer and destabilized low-level atmosphere at night. The air previously trapped within the boundary layer is then able to lift into upper level more easily. Therefore, for time from 0600 UTC to 1200 UTC when LLJ is normally strong, there is an increase of cloud fraction near 700 hPa level showing the signal of this mid-level lifting which can also be seen in PML days (Fig. 4-4e-h). However, these mid-level lifting days are normally with cloud fraction about 5% or less, which indicating a limited contribution from the surface moisture into the upper air. The upper clouds are then still mainly caused by clouds moving from nearby regions. The shallow clouds are similar on PLC days which are sometimes connected to low pressure systems, but with more local triggered clouds in the early morning (1200-1800 UTC). Higher shallow cloud fraction is found in PMCS days as compared to PLLJ days during the nighttime (0600-1200 UTC) due to the strong wind in PLLJ days that disrupt the local signal. With the reduced LLJ advection of the clouds in the early morning, PLLJ days showed an increase in shallow cloud fraction thus indicating a stronger signal of local L-A interaction. Considering all of the analysis above, the overall local L-A interaction seems to produce shallow clouds and precipitation in the afternoon with a cloud faction of 10% and partly in the early morning as well. The evening and night precipitation is mainly caused by the moving the upper-level cloud system with cloud fraction of at least 20%. The local L-A coupling, when the environment is favored at night due to larger temperature drop or/and LLJ impact, is able to trigger deep convection and contribute to less than 10% upper cloud fraction (the 700 hPa level with L-A coupling shows about 7.5% cloud fraction lifting upward in Fig. 4-4c-h).

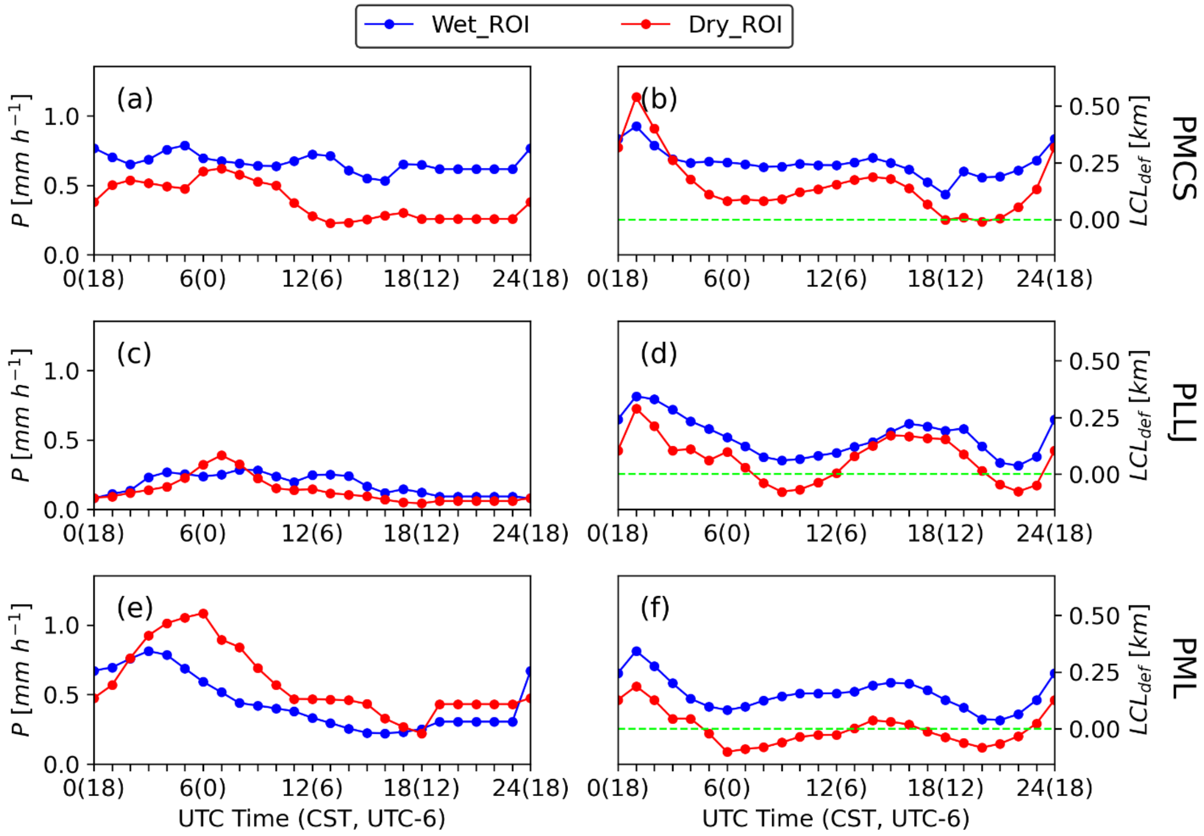

Figure 4-6:
Diurnal precipitation and LCL deficit for PMCS, PLLJ and PML days

All explanations above are based on comparison of different precipitation days in cu-off, which may not be accurate especially for interpretation of local coupling contribution. To confirm that the soil moisture does impact the precipitation in both the afternoon and nighttime on PLC, PMCS and PML days, and to better quantify the contribution of the L-A coupling, the previous cu-off results are compared with the cu-off_SWD to verify the previous explanation. The difference in the diurnal 1-m RSM, LCL deficit and precipitation for different precipitation days is plotted in Figure 4-8. The corresponding cloud fraction profiles are shown in Figure 4-9. It should be noted that the change in initial soil condition in cu-off_SWD does not keep the soil moisture to be wetter or drier throughout the entire drought compared to the original run in cu-off. To analyze the diurnal soil moisture impact, it should be treated differently based on the soil and other conditions for each precipitation category. Meanwhile, since the upper-level cloud fraction are largely impacted by the surrounding environment, the analysis focuses on how the soil moisture affects the low-level cloud fraction, and how largely the moisture is transport to the upper levels through deep L-A interactions.

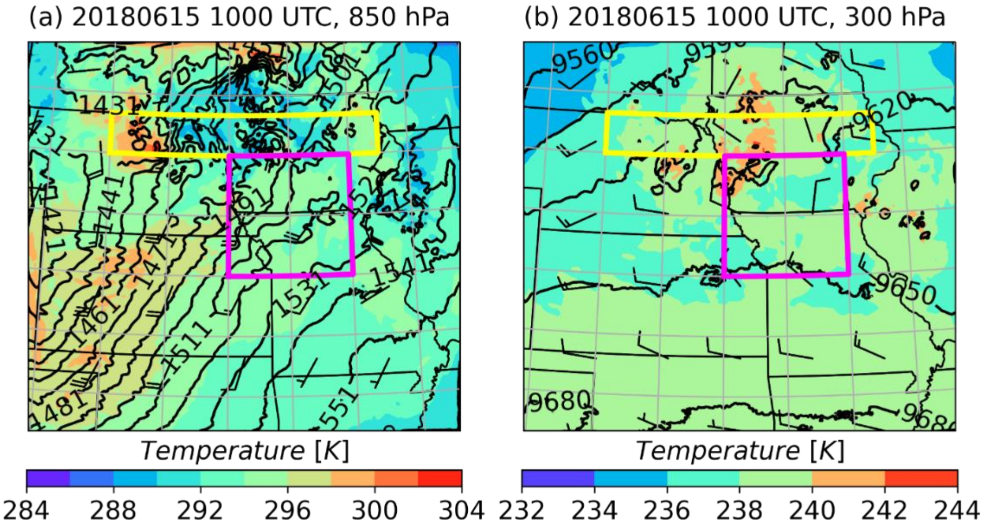

Figure 4-7:
Temperature at the 850 hPa (a) and 300 hPa (b) levels on 15th of June 2018. Location with rapid change of geopotential height in low level and higher temperature at high level indicates a deep convection

For PLC days, the 1-m RSM of cu-off_SWD in the dry and wet regions maintain its switched soil moisture status with a wet bias in dry region and a dry bias in wet region of about 0.05 (Fig. 4-8a). The corresponding LCL deficits also showed a decrease in dry region and a slight increase in wet region, meaning an increase (slight decrease) of L-A coupling in dry (wet) region. For 18-24 UTC when the L-A is strong in the afternoon, the cloud fraction in the low-level heights (>700 hPa) show a consistent change in response to their soil moisture change with increased cloud fraction less than 2% over dry region and the opposite over the wet region. For the night-morning time from 0400 UTC to 1200 UTC when local L-A might be active, no clear deep L-A interaction is observed. By comparing the wet and dry region, the cloud fraction change in 700-900 hPa levels is likely caused by cloud maintenance from early evening (Fig. 4-9a) or by advection (Fig. 4-9b). The clear boundary around 700 hPa level separating the opposite cloud fraction change over the wet region indicates a normally uncoupled state between the low level and middle level atmosphere. This boundary can also be seen in the dry region with a lighter red color separating the two increased cloud regions above and below.

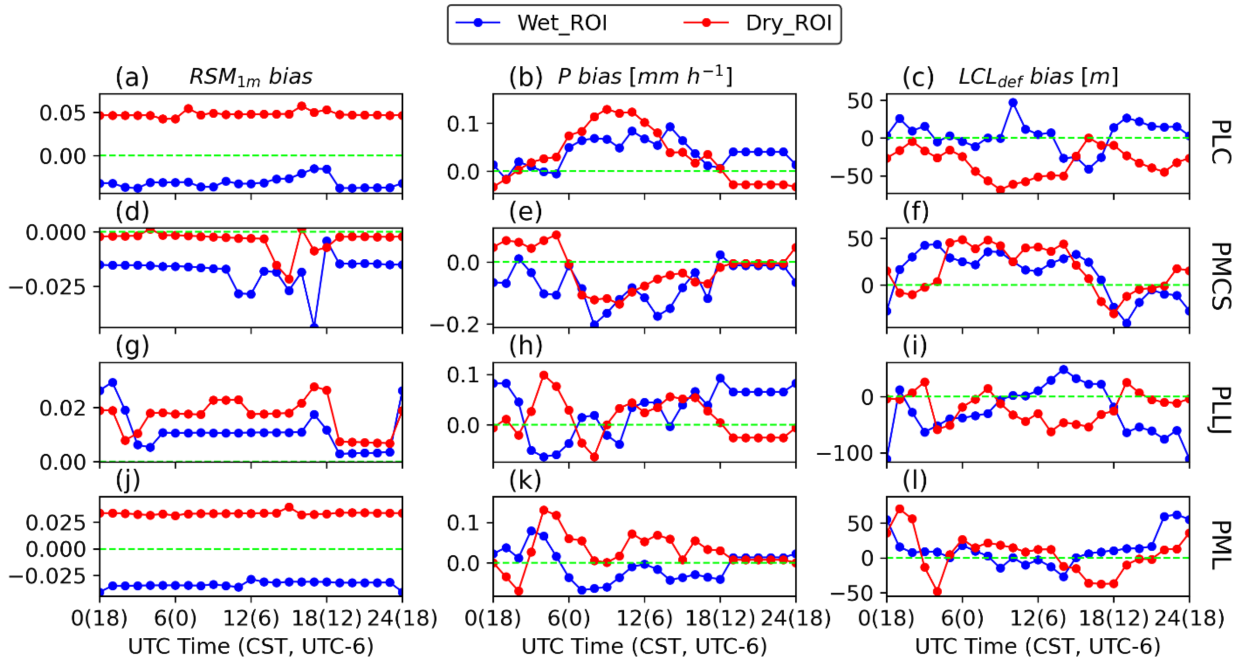

Figure 4-8:
Difference of diurnal RSM, LCL deficit and precipitation between cu-off_SWD and cu-off

The PMCS days are less interesting because the L-A coupling is weaker in the afternoon compared to PLC days (Fig. 4-3h and Fig. 4-6b). However, the decrease of LCL deficit in cu-off_SWD overshadows the impact of the small decrease in soil moisture and increased the shallow cloud fraction in both the regions. During the night, the land surface is uncoupled with the air above the boundary layer and does not feel the impact of the soil moisture change. In contrast, the PLLJ days show more clear results with enhanced L-A coupling around midnight and from 0900 UTC to 1200 UTC over the dry region (Fig. 4-8i). There is a clear spread of increased cloud fraction from near surface up to 300 hPa level in the dry region (Fig. 4-9f). This indicates a possible deep convection or a disturbance by the moisture brought in the LLJ. The performance in the wet region may provide some hints to the soil moisture impact. The wet region showed an enhanced L-A coupling around midnight and an increased decoupling in the morning with both LCL deficit positive (Fig. 4-6d and Fig. 4-8i). The decreased low-level cloud fraction around midnight is the opposite reaction to the increased soil moisture, which seems to indicate that the low-level change in cloud fraction is caused by the LLJ disturbance. However, there is an increased cloud fraction rising from 800 hPa to 500 hPa levels in the morning before 1200 UTC, which indicates a deep interaction also seen over the dry region. The 1200 UTC is critical here to separate the impact of LLJ and daytime heating because a low-to-middle level lifting is also seen in PLC days after 1200 UTC, which can be explained by the daytime heating and increased evaporation. The deep lifting found before 1200 UTC in PLLJ days is then a good proof illustrating how LLJ enhanced L-A interaction during the night, which is not seen in PLC days. During the nighttime, LLJ can build the well mixed moist low-level atmosphere with both moisture brought in from the southerly LLJ and the moisture released from the boundary layer when the land surface is coupled with the lower atmosphere (700 to 900 hPa, clearly seen on the dry region in Fig. 4-9f,d). The low level moisture is then lifted through normal interaction (mainly by daytime heating) or digested into synoptic system (e.g. cyclone) occurred in the mid-to-upper levels. The latter is commonly seen in the study region during the night with both the higher cloud fraction larger than 30% near the 300 hPa level and the extended cloud fraction larger than 15% above 500 hPa level. The soil moisture is then transmitted into low level via LLJ induced coupling and moreover into upper levels with occurred synoptic systems. The transmission from low level into mid-to-upper level is not easy to see in the early night because of the strong low-level wind which transfers the signal outside the small study region, but it is easier to see when LLJ gets weaker in the early morning. This pattern can also be seen in PML days as the change of cloud fraction in the low level is gradually passing to the upper levels during the night when more upper MCS occurred (Fig. 4-9h).

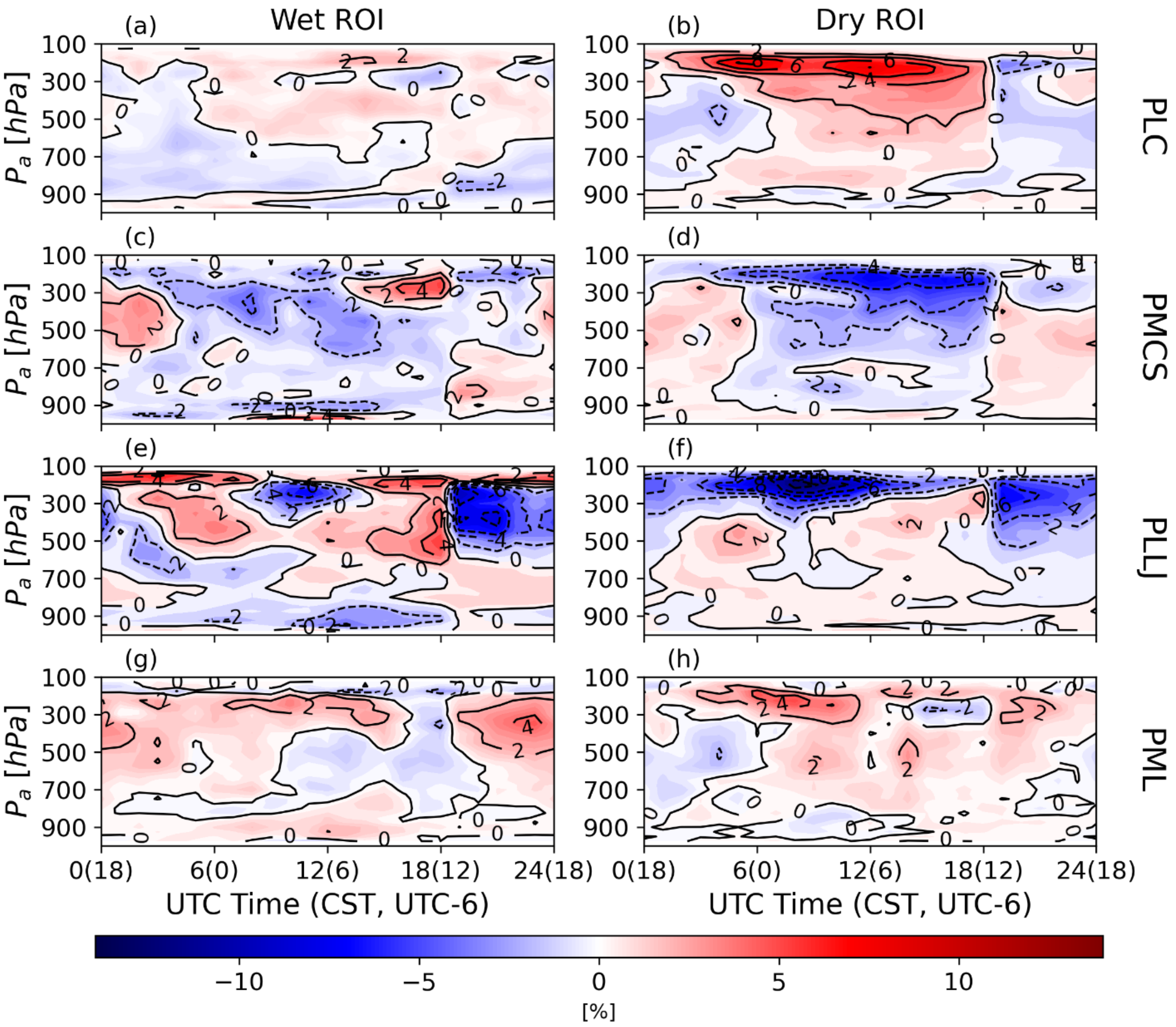

Figure 4-9:
Difference of cloud fraction diurnal profiles between cu-off_SWD and cu-off. The contours are drawn with an interval of 2%.

4.2.3 Diurnal Soil Moisture Path into Upper Troposphere

The previous two sections provide detailed explanations of when, where, and how the soil moisture impacts cloud formation in both the low levels and upper levels. To summarize the information and provide a better reference explaining all processes found in this study, a schematic plot showing the diurnal path of the soil moisture lifting and transporting into the upper troposphere is drawn in Figure 4-10. In this plot, the troposphere is split into three layers: low level with pressures larger than 800 hPa; middle level from 800 hPa to 500 hPa; and high level above 500 hPa. Figure 4-4 shows clear boundaries between these layers because of their respective speed of air movement. The lowest layer normally indicates where the boundary layer varies, which is decoupled with the air above except for during the daytime and an LLJ event at night. The evaporated soil moisture in the day might remain to form the shallow clouds and later falls back to soil as rain. When the shallow cloud does not form, the evaporative soil moisture has a chance to rise to the middle level, which has a relatively slower lifting compared to upper levels with largely spread similar cloud fraction (Fig. 4-4 and Fig. 4-9). The upper layer, which has strong westerlies and often bring MCSs and other synoptic systems (e.g. cyclones), absorb and accelerate the lifting moisture around 500 hPa at the boundary indicated by a rapid increase in cloud fraction (Fig. 4-4). Thus, even the boundary layer is decoupled from above air in the night, the mid-to-upper-level lifting can be strong with the frequent occurred weather system above. The moisture trapped in the nighttime boundary layer, is then more likely lifted to middle level on the next day. These processes produced about half or more than a day for surface moisture to finally reach the upper level and contribute to intensifying the precipitation.

Certainly, the soil moisture can be quickly recycled within a few hours in the daytime by precipitation from a shallow cloud. However, most of the precipitation within the study region is caused by the upper-level advection of the cloud system (including MCS) at night, which means the contributed soil moisture during this time should be traced back to the daytime evaporation or/and from the previous day residual moisture in the atmosphere. This time lag transport is important because it explained why the LLJ is found to have a weak relationship with the precipitation one or two days later as seen in chapter 3. Previous studies (Berg et al. 2015; Ferguson et al. 2020) showed the LLJ is prevalent from late evening (0200 UTC) to the morning (1200 UTC) in the Great Plain and peak around 0600 UTC. As depicted in Figure 4-10, the LLJ promotes air interaction between boundary layer and middle levels by adding moisture instability and provides opportunity transmitting the moisture further into upper levels with enhancement by synoptic systems. These processes take a few hours allowing low-level moisture reaching high levels when the strong upper cloud system starts dissipating by the precipitation produced in the early evening. The moisture lifted into upper levels thus partly condensed and forms precipitation within the existing cloud system, but sometimes it is still possible for moisture to leave in the upper level. The latter is very likely to happen if LLJ lasts longer time than 0600 UTC which makes the lifted moisture to reach the upper level in the morning (after 1200 UTC). Figure 4-6d shows a night LCL deficit decrease with a trough at 0900 UTC for PLLJ days, which confirms the assumption that the strongest LLJs in the study region occurred after 0600 UTC. This allows the lifted moisture to more likely stay in the atmosphere instead of forming precipitation in the nighttime. The remaining moisture destabilizes the upper level and makes the environment more favorable for precipitation the next day. If there is not much high-level cloud transport and without synoptic system or strong pressure gradient change, the upper moisture may be maintained and contribute to the precipitation even later in the day. In this way, the LLJ build a weak link with the precipitation in the next two days, as is found in chapter 3.

Overall, the contribution of the soil moisture to the precipitation seems to be small. Figure 4-9 shows that the change in RSM less than 5% commonly results in a cloud fraction change less than 2%. The precipitation change, therefore, is not directly impacted by the change of local soil moisture except for the afternoon precipitation and during parts of the morning. Although this contribution looks very small, a total of 16 (11) days in wet (dry) region are found to change the P-MCS-LLJ classifications. This means even the small change of soil moisture (< 0.05 m^{-3} m^{-3} in Fig. 4-1) could impact the surrounding region and produce an obvious change in precipitation intensity of 7-10% of the total days.

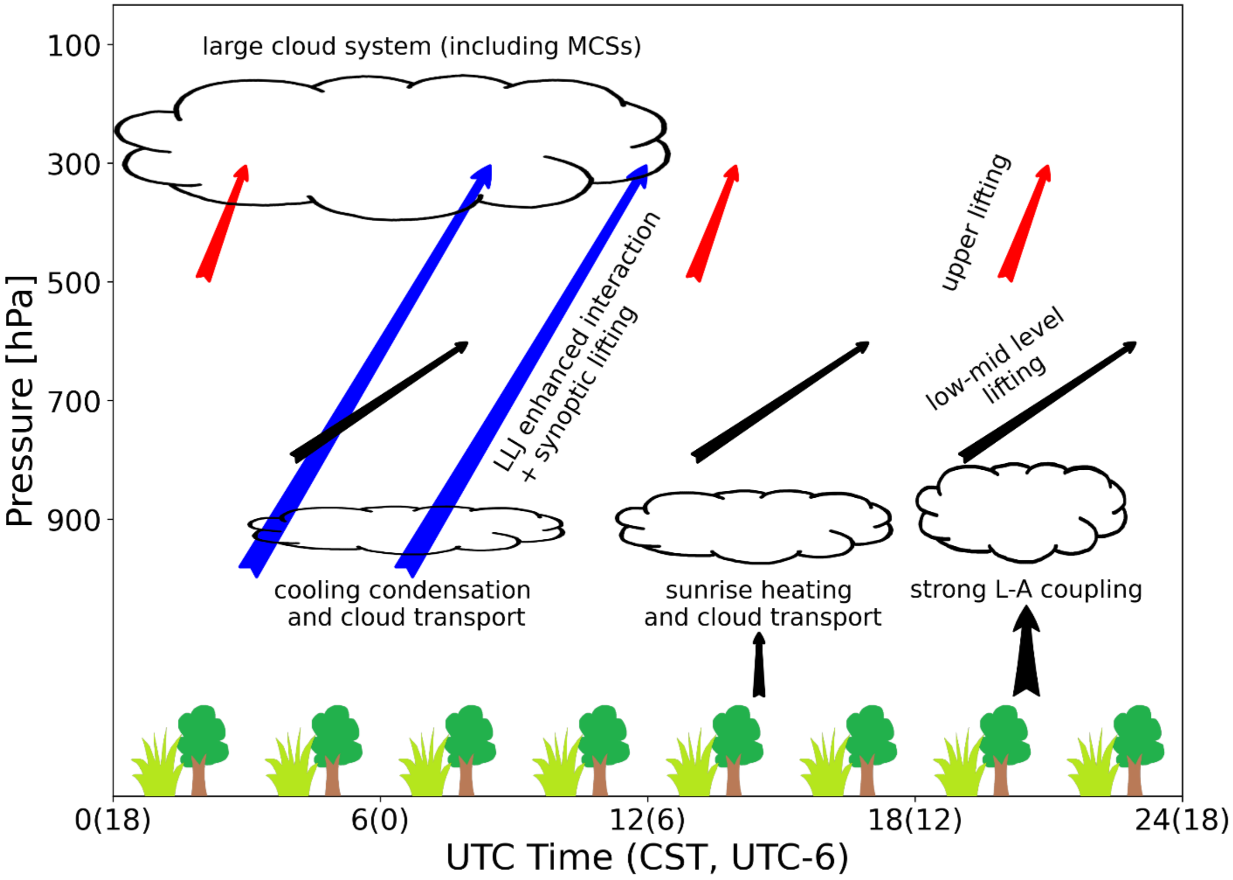

Figure 4-10:
Schematic plot of diurnal soil moisture path lifting to the upper troposphere. The red arrows indicates the upper moisture movement. The blue arrow shows the enhanced lifting with impacts of LLJ and synoptic system in LLJ nighttime. The black arrows are low and middle level path during normal conditions without the LLJ influence.

4.3 Discussion

The results of this chapter provide a better understanding of the moisture path contributing to precipitation from the surface and provide further insights to explain the model weakness in underestimating the nighttime MCSs in chapter 3. The large underestimation of MCSs in the model is mainly from 0400 UTC to 1800 UTC covering the whole night and early morning (Fig. 3-4a). Because the MCS is found in the upper level where geopotential height, wind and temperature are nudged in the model, the miss in MCS frequency is likely related to the upper moisture rather than a miss of large-scale system. This also reduces the likelihood of it being caused by the MERRA-2 forcing and focuses the attention to moisture transport. There are two possibilities causing the lack of MCSs in the night: one is a lack of lifting which does not provide enough moisture to support the formation and maintenance of the MCSs; the other possible cause is the inaccurate arrangement of MCS stability which produces precipitation too quickly in the early evening so that it cannot be maintained later in the nighttime. Previous results in chapter 3 (Fig. 3-4 and Table 3-2) showed that the model produce more MCS precipitation with shorter durations than the reference, which excludes the first guess of weak lifting. Although MCSs in this study comes from the nearby region, they should also form by moisture lifting and convergence. Therefore, the underestimate of MCSs should be mainly caused by its strong instability and fast moisture depletion in the early evening, which indicates too much moisture condensation in the cloud system (because the upper temperature is nudged). Another possibility for this error is issues in the microphysics scheme used. The Goddard 3ICE scheme is used in this study, which is found to be less skillful than an updated new Goddard 4ICE (cloud ice, snow, graupel, and frozen drops/hail) scheme simulating reflectivity structures and precipitation rate (Tao et al. 2016). Therefore, a new microphysics scheme may help alleviate this problem and should be tested in the future. However, the microphysics scheme is not the only possible cause. Recalling the finding in this chapter that the moisture contributes to upper-level clouds during the night (not considering the time when other large-scale system exists) comes from the daytime evaporation and if present, the residual moisture from previous day. It means the overestimate condensation of clouds may be caused by the moisture transport. If this happen, either one or both of daytime and nighttime moisture transport are overestimated. Although it is not directly known if the residual moisture comes from the local lifting process or by moisture transport in the previous day, the finding in chapter 3 that the model precipitation is slightly more sensitive to LLJ as compared to the reference with a day in advance (Fig. 3-9) implies an overestimation in local moisture lifting. Chapter 3 shows that the model produced slightly less latent heat and much higher sensible heat in both wet and dry regions (Fig. 3-8a-d), which means the overestimated moisture lifting is not caused by the local evapotranspiration. The higher sensible heat can produce higher boundary layer growth, which in turn make it easier for the LLJs to bring the near surface moisture up to higher levels. Therefore, the overestimated residual moisture lifted by LLJ from previous day, if it exists, should contribute to form more intense MCSs in the early evening and results in quick dissipation. However, it is not sure if the daytime moisture lifting is overestimated. Without a reference of boundary layer height, it cannot tell whether the model soil moisture in the daytime is easier to be trapped in the low-level layer because of the strong L-A coupling. In addition, how the overestimated sensible heat could impact the speed at which air parcel rises in the normal conditions (without LLJ and nearby weather system) is not known. These are questions beyond the scope of this study but should be checked in the future. Because this study only analyzed one warm season especially during a drought period, there is uncertainty to whether the same finding would persist during other time periods. However, if the overestimate MCS intensity during the early evening is caused by the overestimate sensible heat, it is expected that a similar results in other time periods when sensible heat is also overestimated would be seen.

Besides the moisture lifting, there are also some other interesting questions not answered in this chapter. The small change of initial soil moisture in this study may limit the interpretation of soil moisture contribution. If more extreme initial soil moisture such as the wilting point and saturated soil conditions were tested, it could lead to a clearer understanding of the baseline and the upper limit of its contribution. With more tests of different soil moisture conditions, how other soil moisture conditions impacts the enhancement or weakening of precipitation and the resulting nonlinear relationship cloud be explored. Another interesting aspect would be to check how different soil layers contribute and react to different precipitation intensities and how this feeds back into the atmosphere. Further research into these topics would broaden our understanding of L-A interaction.

4.4 Conclusion

This chapter presents a further analysis and provides understanding of the model performance from chapter 3. With the separation of different precipitation days, the vertical diurnal profile of cloud fraction illustrates when and where the different precipitation is formed in the atmosphere, which provides a way to understand L-A interaction and its interaction with MCSs and LLJs. The new model run (cu-off _SWD) with switched initial soil moisture in the wet and dry region creates a disturbance in soil moisture and provides a chance to identify its impact in the complicated environment. The difference between the cu-off and cu-off_SWD enables quantifying the contribution of soil moisture change to precipitation in terms of cloud fraction change. These analyses together build the understanding of the path for transporting soil moisture in the atmosphere. A soil moisture change less than 0.05 m^3 m^{-3} is found to produce less than 2% change in cloud fraction lifting to the upper troposphere. However, it still produced a 7-10% change in days with obvious precipitation intensity changes. More analyses are needed in the future to break the limitation of the small soil moisture change in this study.

In addition, there are two additional findings in this chapter. One is the enhanced moisture interaction caused by the increased instability from LLJ disturbance in the late nighttime which functions with frequent synoptic systems (e.g. mid-to-upper level cyclones) and explained the delayed LLJ contribution to precipitation 1-2 days later. Another finding is that the overestimate sensible heat flux in the model may contribute to its short-lived yet more intense MCS prediction. Although more studies are needed to support the explanation here, this chapter provides a solid basis for future studies.

Chapter 5: Conclusion and Future Work

This study provides a comprehensive evaluation of precipitation simulations from the NU-WRF model over the Central Great Plains. The precipitation forecasts are minimally influenced by model resolution, but a larger influenced by the cumulus scheme. At a fine resolution of 4km, there is no need to use the cumulus scheme. The results showed that the use of G3D scheme produced more light precipitation with a slight wet bias, and a large underestimation of MCSs. On the contrary, the model without the use of the cumulus scheme (cu-off) produced a higher level of skill at simulating spatial pattern of precipitation. After analyzing different precipitation types, the cu-off model is found to have a mediocre skill at reproducing different precipitation with MCS and LLJ impact at a daily time scale. During the 2018 drought period (May-Sep) in the Central Plains, MCSs are the dominant contributor of precipitation. The LLJ, however, is found to indirectly contributing to precipitation 1-2 days later. With further analysis of the diurnal L-A interactions, a soil moisture path illustrating its transport in the atmosphere under different atmospheric environment (with/without MCS/LLJ) is developed (Figure 4-10). Due to the chosen drought period and the small change of soil moisture in designed experiment, the soil moisture impact on precipitation was found to be small. The change of soil moisture less than 0.05 m^3 m^{-3} produced less than 2% change in cloud fraction lifting in the upper troposphere. However, it still produced a 7-10% days with obvious precipitation intensity change. Therefore, it is still possible to see a larger soil moisture contribution to precipitation if larger soil moisture change is made or a wetter period is selected.

This study also points out some model deficiencies, such as the largely overestimated sensible heat flux and the underestimated MCSs during nighttime. The overestimate heat flux is from the overestimated net shortwave radiation, which might be due to the radiation scheme (Goddard 2011) used in this study. The underestimated nighttime MCSs is thought to be caused by the large formation of clouds in the early evening which produces more intense but short-lived precipitation. Although the exact cause of these problems is not known, a few hypothesizes are presented. One hypothesis is that the overestimated sensible heat flux which enhances the L-A interaction via LLJ increased instability and/or the strong L-A coupling in the daytime. Another hypothesis is that the overestimate lifting or the error in microphysics scheme (Goddard 3ICE scheme) used in the study. Therefore, both newer microphysics and radiation schemes should be tested in the future and may fix the model deficiencies found in this study.

Even though there are still lingering questions, this research has moved the needle forward in our understanding of precipitation prediction in a coupled modeling system. First, the techniques and methodologies developed and used in this work provide a framework for further assessing and understanding precipitation processes and the ability to replicate these processes in a coupled modeling framework. The 2-filter method used in this study support which utilizes machine-learning to identify MCSs in the NU-WRF model will be beneficial for further studies, although the method still needs additional testing and improving the accuracy and further comparison with different machine-learning methods in order to quantify the advantages and limitations (e.g., impact of sample size, regional and scale dependency) of using different methods. If this method could be widely applied in the future, it can largely improve the efficiency of MCS identifications and analysis. Similarly, the separation of local and non-local precipitation can be applied in other regions considering the important non-local weather systems not limited to MCSs and LLJs. This would provide more evidence for understanding the L-A interactions under different weather systems and climatic environment. The dry period in this study, which is found to have the least non-local impacts and stronger local L-A signal, is a better time period for analyzing local L-A interactions. The application of the method to further analysis of future drought events has promising implications.

Second, the spatial analysis in chapter 2 and the tracking of MCSs in chapter 3 state meaningful study direction in spatial monitoring and analysis to track and understand dynamic evolution of extreme events (such as droughts and severe storms) instead of their impacts in specific regions. This would be very useful in large scale and global studies when there is a large spatial expansion and/or a long-distance movement of the extreme events. With the spatial tracking, we would better understand when, where, how large and long a complete extreme event cycle is, and whether there are any similarities between different events. This not only can expand our knowledge of regional weather and climate environment, but also can provide useful information for extreme event forecasting.

Third, the impact of LLJ and L-A interaction in this study indicates that soil moisture tracking would be a good research topic for future studies. Unlike the small study region in this work, future study can use a larger domain to better represent moisture transmission, especially for days with strong winds. Alternatively, analyzing the soil moisture impact in downwind locations can also provide insights on the speed, the spatial extent and the intensity of soil moisture impact on precipitation formation under different large scale circulation patterns. Moreover, it provides a method to further understand how and to what degree the LLJ impacts local moisture transmission that contributes to cloud formation and precipitation. With a larger change of soil moisture, the moisture tracking would provide a stronger signal for moisture transport with and without LLJ impact and provide upper limits of the soil moisture contribution to precipitation formation under different environments in model simulations.

Ultimately, this work has found new insights that have the potential to improve prediction of precipitation and to improve forecasts of extreme events like droughts and floods. The timely and accurate weather forecast would provide longer lead times for decision makers to prepare and design strategies that minimize the negative influence of extreme events on society (e.g. damage to property, agriculture and life). The more accurate a model predicts precipitation, the more efficient a solution may be found with multiple plans and the lower risk and uncertainty would occur dealing with the real events. From a longtime and macro perspective, the improvement in weather forecast can also reveal a more realistic change in climate, especially from a global aspect. This would be informative for researchers understanding the global environment and the challenges we are facing to, and provide suggestions to policy makers on how we can arrange water resources and energy use more appropriately.

References

Barandiaran, D., S. Y. Wang, and K. Hilburn, 2013: Observed trends in the Great Plains low-level jet and associated precipitation changes in relation to recent droughts. *Geophys. Res. Lett.*, **40**, 6247–6251, doi:10.1002/2013GL058296.

Berg, L. K., L. D. Riihimaki, Y. Qian, H. Yan, and M. Huang, 2015: The low-level jet over the southern great plains determined from observations and reanalyses and its impact on moisture transport. *J. Clim.*, **28**, 6682–6706, doi:10.1175/JCLI-D-14-00719.1.

Betts, A. K., and J. H. Ball, 1998: FIFE Surface Climate and Site-Average Dataset 1987–89. *J. Atmos. Sci.*, **55**, 1091–1108, doi:10.1175/1520-0469(1998)055<1091:FSCASA>2.0.CO;2.

Bonner, W. D., 1968: Climatology of the Low Level Jet. *Mon. Weather Rev.*, **96**, 833–850, doi:10.1175/1520-0493(1968)096<0833:cotllj>2.0.co;2.

Brown, B., and Coauthors, 2021: The Model Evaluation Tools (MET): More than a Decade of Community-Supported Forecast Verification. *Bull. Am. Meteorol. Soc.*, **102**, E782–E807, doi:10.1175/BAMS-D-19-0093.1.

Brown, B. G., L. Holland, J. E. H. Gotway, R. Bullock, D. a. Ahijevych, E. Gilleland, and C. a. Davis, 2007: Application of the MODE object-based verification tool for the evaluation of model precipitation fields. *22nd Conf. Weather Anal. Forecast. / 18th Conf. Numer. Weather Predict.*, 8.

Burrows, D. A., C. R. Ferguson, M. A. Campbell, G. Xia, and L. F. Bosart, 2019: An objective classification and analysis of upper-level coupling to the great plains low-level jet over the twentieth century. *J. Clim.*, **32**, 7127–7152, doi:10.1175/JCLI-D-18-0891.1.

Campbell, M. A., C. R. Ferguson, D. A. Burrows, M. Beauharnois, G. Xia, and L. F. Bosart, 2019: Diurnal effects of regional soil moisture anomalies on the great plains low-level jet. *Mon. Weather Rev.*, **147**, 4611–4631, doi:10.1175/MWR-D-19-0135.1.

Carbone, R. E., and J. D. Tuttle, 2008: Rainfall occurence in the U.S. warm season: The diurnal cycle. *J. Clim.*, **21**, 4132–4146, doi:10.1175/2008JCLI2275.1.

——, ——, D. A. Ahijevych, and S. B. Trier, 2002: Inferences of predictability associated with warm season precipitation episodes. *J. Atmos. Sci.*, **59**, 2033–2056, doi:10.1175/1520-0469(2002)059<2033:IOPAWW>2.0.CO;2.

Chen, F., and J. Dudhia, 2001: Coupling an Advanced Land Surface–Hydrology Model with the Penn State–NCAR MM5 Modeling System. Part I: Model Implementation and Sensitivity. *Mon. Weather Rev.*, **129**, 569–585, doi:10.1175/1520-0493(2001)129<0569:CAALSH>2.0.CO;2.

Coniglio, M. C., J. Y. Hwang, and D. J. Stensrud, 2010: Environmental factors in the upscale growth and longevity of MCSs derived from Rapid Update Cycle analyses. *Mon. Weather Rev.*, **138**, 3514–3539, doi:10.1175/2010MWR3233.1.

Davis, C., B. G. Brown, and R. Bullock, 2006a: Object-Based Verification of Precipitation Forecasts. Part II: Application to Convective Rain Systems. *Mon. Weather Rev.*, **134**, 1785–1795, doi:10.1175/MWR3146.1.

Davis, C. A., B. G. Brown, and R. Bullock, 2006b: Object-Based Verification of Precipitation Forecasts. Part I: Methodology and Application to Mesoscale Rain Areas. *Mon. Weather Rev.*, **134**, 1772–1784, doi:10.1175/MWR3145.1.

Diro, G. T., L. Sushama, A. Martynov, D. I. Jeong, D. Verseghy, and K. Winger, 2014: Land-atmosphere coupling over North America in the fifth generation of the Candadian regional climate model (CRCM5). *J. Geophys. Res. Atmos.*, 1–29, doi:10.1002/2014JD021677.

Ek, M. B., K. E. Mitchell, Y. Lin, E. Rogers, P. Grunmann, V. Koren, G. Gayno, and J. D. Tarpley, 2003: Implementation of Noah land surface model advances in the National Centers for Environmental Prediction operational mesoscale Eta model. *J. Geophys. Res. Atmos.*, **108**, 1–16, doi:10.1029/2002jd003296.

Elguindi, N., and A. Grundstein, 2013: An integrated approach to assessing 21st century climate change over the contiguous U.S. using the NARCCAP RCM output. *Clim. Change*, **117**, 809–827, doi:10.1007/s10584-012-0552-z.

Eltahir, E. a. B., 1998: A Soil Moisture–Rainfall Feedback Mechanism: 1. Theory and observations. *Water Resour. Res.*, **34**, 765, doi:10.1029/97WR03499.

Erfanian, A., and R. Fu, 2019: The role of spring dry zonal advection in summer drought onset over the US Great Plains. *Atmos. Chem. Phys.*, **19**, 15199–15216, doi:10.5194/acp-19-15199-2019.

Feng, Z., L. R. Leung, S. Hagos, R. A. Houze, C. D. Burleyson, and K. Balaguru, 2016: More frequent intense and long-lived storms dominate the springtime trend in central US rainfall. *Nat. Commun.*, **7**, 1–8, doi:10.1038/ncomms13429. http://dx.doi.org/10.1038/ncomms13429.

——, ——, R. A. Houze, S. Hagos, J. Hardin, Q. Yang, B. Han, and J. Fan, 2018: Structure and Evolution of Mesoscale Convective Systems: Sensitivity to Cloud Microphysics in Convection-Permitting Simulations Over the United States. *J. Adv. Model. Earth Syst.*, **10**, 1470–1494, doi:10.1029/2018MS001305.

——, R. A. Houze, L. R. Leung, F. Song, J. C. Hardin, J. Wang, W. I. Gustafson, and C. R. Homeyer, 2019: Spatiotemporal characteristics and large-scale environments of mesoscale convective systems east of the rocky mountains. *J. Clim.*, **32**, 7303–7328, doi:10.1175/JCLI-D-19-0137.1.

Ferguson, C. R., and E. F. Wood, 2011: Observed Land-Atmosphere Coupling from Satellite Remote Sensing and Reanalysis. *J. Hydrometeorol.*, **12**, 1221–1254, doi:10.1175/2011JHM1380.1.

Ferguson, C. R., S. Agrawal, M. C. Beauharnois, G. Xia, D. Alex Burrows, and L. F. Bosart, 2020: Assimilation of satellite-derived soil moisture for improved forecasts of the great plains low-level jet. *Mon. Weather Rev.*, **148**, 4607–4627, doi:10.1175/MWR-D-20-0185.1.

Ferraro, R., D. Waliser, and C. Peters-Lidard, 2017: *NASA Downscaling Project Final Report*. https://trs.jpl.nasa.gov/bitstream/handle/2014/45705/17-0785.pdf?sequence=1.

Findell, K. L., and E. a. B. Eltahir, 2003a: Atmospheric Controls on Soil Moisture–Boundary Layer Interactions. Part II: Feedbacks within the Continental United States. *J. Hydrometeorol.*, **4**, 570–583, doi:10.1175/1525-7541(2003)004<0570:ACOSML>2.0.CO;2.

Findell, K. L., and E. A. B. Eltahir, 2003b: Atmospheric Controls on Soil Moisture–Boundary Layer Interactions. Part I: Framework Development. *J. Hydrometeorol.*, **4**, 552–569, doi:10.1175/1525-7541(2003)004<0552:ACOSML>2.0.CO;2.

Ford, T. W., A. D. Rapp, S. M. Quiring, and J. Blake, 2015: Soil moisture-precipitation coupling: Observations from the Oklahoma Mesonet and underlying physical mechanisms. *Hydrol. Earth Syst. Sci.*, **19**, 3617–3631, doi:10.5194/hess-19-3617-2015.

Friedman, J. H., 2001: Greedy function approximation: A gradient boosting machine. *Ann. Stat.*, **29**, 1189–1232, doi:10.1214/aos/1013203451.

Fritsch, J. M., R. J. Kane, and C. R. Chelius, 1986: The Contribution of Mesoscale Convective Weather Systems to the Warm-Season Precipitation in the United States. *J. Clim. Appl. Meteorol.*, **25**, 1333–1345, doi:10.1175/1520-0450(1986)025<1333:TCOMCW>2.0.CO;2.

Gao, Y., L. R. Leung, C. Zhao, and S. Hagos, 2017: Sensitivity of U.S. summer precipitation to model resolution and convective parameterizations across gray zone resolutions. *J. Geophys. Res. Atmos.*, **122**, 2714–2733, doi:10.1002/2016JD025896.

Gilleland, E., D. Ahijevych, B. G. Brown, B. Casati, and E. E. Ebert, 2009: Intercomparison of Spatial Forecast Verification Methods. *Weather Forecast.*, **24**, 1416–1430, doi:10.1175/2009waf2222269.1.

Giorgi, F., C. Jones, and G. R. Asrar, 2009: Addressing climate information needs at the regional level: The CORDEX framework. *World Meteorol. Organ. Bull.*, **58**, 175–183.

Grell, G. A., and D. Dévényi, 2002: A generalized approach to parameterizing convection combining ensemble and data assimilation techniques. *Geophys. Res. Lett.*, **29**, 38-1-38–4, doi:10.1029/2002GL015311. http://doi.wiley.com/10.1029/2002GL015311.

Haberlie, A. M., and W. S. Ashley, 2018a: A Method for Identifying Midlatitude Mesoscale Convective Systems in Radar Mosaics. Part II: Tracking. *J. Appl. Meteorol. Climatol.*, **57**, 1599–1621, doi:10.1175/JAMC-D-17-0294.1.

——, and ——, 2018b: A method for identifying midlatitude mesoscale convective systems in radar mosaics. Part I: Segmentation and classification. *J. Appl. Meteorol. Climatol.*, **57**, 1575–1598, doi:10.1175/JAMC-D-17-0293.1.

——, and ——, 2019: A radar-based climatology of mesoscale convective systems in the United States. *J. Clim.*, **32**, 1591–1606, doi:10.1175/JCLI-D-18-0559.1.

Han, J., and H.-L. Pan, 2011: Revision of Convection and Vertical Diffusion Schemes in the NCEP Global Forecast System. *Weather Forecast.*, **26**, 520–533, doi:10.1175/WAF-D-10-05038.1.

Hane, C. E., J. A. Haynes, D. L. Andra, and F. H. Carr, 2008: The evolution of morning convective systems over the U.S. Great plains during the warm season. Part II: A climatology and the influence of environmental factors. *Mon. Weather Rev.*, **136**, 929–944, doi:10.1175/2007MWR2016.1.

Hastie, T., R. Tibshirani, and J. Friedman, 2009: *The Elements of Statistical Learning*. 2nd ed. Springer New York, New York, NY, http://link.springer.com/10.1007/978-0-387-84858-7.

Herrera-Estrada, J. E., J. A. Martinez, F. Dominguez, K. L. Findell, E. F. Wood, and J. Sheffield, 2019: Reduced Moisture Transport Linked to Drought Propagation Across North America. *Geophys. Res. Lett.*, **46**, 5243–5253, doi:10.1029/2019GL082475.

Hirsch, A. L., J. Kala, C. C. Carouge, M. G. De Kauwe, G. Di Virgilio, A. M. Ukkola, J. P. Evans, and G. Abramowitz, 2019: Evaluation of the CABLEv2.3.4 Land Surface Model Coupled to NU-WRFv3.9.1.1 in Simulating Temperature and Precipitation Means and Extremes Over CORDEX AustralAsia Within a WRF Physics Ensemble. *J. Adv. Model. Earth Syst.*, 1–23, doi:10.1029/2019MS001845.

Hobbins, M. T., A. Wood, D. J. McEvoy, J. L. Huntington, C. Morton, M. Anderson, and C. Hain, 2016: The evaporative demand drought index. Part I: Linking drought evolution to variations in evaporative demand. *J. Hydrometeorol.*, **17**, 1745–1761, doi:10.1175/JHM-D-15-0121.1.

Houze, R. A., 2004: Mesoscale convective systems. *Rev. Geophys.*, **42**, RG4003, doi:10.1029/2004RG000150.

Hsu, H., M. H. Lo, B. P. Guillod, D. G. Miralles, and S. Kumar, 2017: Relation between precipitation location and antecedent/ subsequent soil moisture spatial patterns. *J. Geophys. Res.*, **122**, 6319–6328, doi:10.1002/2016JD026042.

Hu, H., L. R. Leung, and Z. Feng, 2021: Early warm-season mesoscale convective systems dominate soil moisture–precipitation feedback for summer rainfall in central United States. *Proc. Natl. Acad. Sci.*, **118**, e2105260118, doi:10.1073/pnas.2105260118.

Huang, C. S. Y., and N. Nakamura, 2016: Local finite-amplitude wave activity as a diagnostic of anomalous weather events. *J. Atmos. Sci.*, **73**, 211–229, doi:10.1175/JAS-D-15-0194.1.

Iguchi, T., and Coauthors, 2017: Sensitivity of CONUS Summer Rainfall to the Selection of Cumulus Parameterization Schemes in NU-WRF Seasonal Simulations. *J. Hydrometeorol.*, **18**, 1689–1706, doi:10.1175/JHM-D-16-0120.1.

Janjić, Z. I., 1990: The Step-Mountain Coordinate: Physical Package. *Mon. Weather Rev.*, **118**, 1429–1443, doi:10.1175/1520-0493(1990)118<1429:TSMCPP>2.0.CO;2.

——, 1994: The Step-Mountain Eta Coordinate Model: Further Developments of the Convection, Viscous Sublayer, and Turbulence Closure Schemes. *Mon. Weather Rev.*, **122**, 927–945, doi:10.1175/1520-0493(1994)122<0927:TSMECM>2.0.CO;2.

——, 2002: Nonsingular Implementation of the Mellor-Yamada Level 2.5 Scheme in the NCEP Meso model. *NCEP Off. Note*, **437**, 61.

Jeworrek, J., G. West, and R. Stull, 2019: Evaluation of cumulus and microphysics parameterizations in WRF across the convective gray zone. *Weather Forecast.*, **34**, 1097–1115, doi:10.1175/WAF-D-18-0178.1.

Kain, J. S., 2004: The Kain–Fritsch Convective Parameterization: An Update. *J. Appl. Meteorol.*, **43**, 170–181, doi:10.1175/1520-0450(2004)043<0170:TKCPAU>2.0.CO;2.

Kim, J., and Coauthors, 2018: Winter precipitation characteristics in western US related to atmospheric river landfalls: observations and model evaluations. *Clim. Dyn.*, **50**, 231–248, doi:10.1007/s00382-017-3601-5.

Koster, R. D., 2004: Regions of Strong Coupling Between Soil Moisture and Precipitation. *Science (80-.).*, **305**, 1138–1140, doi:10.1126/science.1100217.

——, S. D. Schubert, H. Wang, S. P. Mahanama, and A. M. Deangelis, 2019: Flash drought as captured by reanalysis data: Disentangling the contributions of precipitation deficit and excess evapotranspiration. *J. Hydrometeorol.*, **20**, 1241–1258, doi:10.1175/JHM-D-18-0242.1.

Kumar, S. V., and Coauthors, 2006: Land information system: An interoperable framework for high resolution land surface modeling. *Environ. Model. Softw.*, **21**, 1402–1415, doi:10.1016/j.envsoft.2005.07.004.

Kwon, Y. C., and S. Y. Hong, 2017: A mass-flux cumulus parameterization scheme across gray-zone resolutions. *Mon. Weather Rev.*, **145**, 583–598, doi:10.1175/MWR-D-16-0034.1.

Lavers, D. A., and G. Villarini, 2013: Atmospheric rivers and flooding over the central United States. *J. Clim.*, **26**, 7829–7836, doi:10.1175/JCLI-D-13-00212.1.

Lee, H., D. E. Waliser, R. Ferraro, T. Iguchi, C. D. Peters-Lidard, B. Tian, P. C. Loikith, and D. B. Wright, 2017: Evaluating hourly rainfall characteristics over the U.S. Great Plains in dynamically downscaled climate model simulations using NASA-Unified WRF. *J. Geophys. Res. Atmos.*, **122**, 7371–7384, doi:10.1002/2017JD026564.

Li, L., W. Li, and J. Jin, 2014: Improvements in WRF simulation skills of southeastern United States summer rainfall: physical parameterization and horizontal resolution. *Clim. Dyn.*, **43**, 2077–2091, doi:10.1007/s00382-013-2031-2.

Li, S., and A. W. Robertson, 2015: Evaluation of submonthly precipitation forecast skill from global ensemble prediction systems. *Mon. Weather Rev.*, **143**, 2871–2889, doi:10.1175/MWR-D-14-00277.1.

Lin, Y., 2011: GCIP/EOP Surface: Precipitation NCEP/EMC 4KM Gridded Data (GRIB) Stage IV Data. Version 1.0. doi:10.5065/d6pg1qdd.

Liu, C., and Coauthors, 2017: Continental-scale convection-permitting modeling of the current and future climate of North America. *Clim. Dyn.*, **49**, 71–95, doi:10.1007/s00382-016-3327-9.

Livneh, B., and M. P. Hoerling, 2016: The physics of drought in the U.S. Central Great Plains. *J. Clim.*, **29**, 6783–6804, doi:10.1175/JCLI-D-15-0697.1.

——, and A. M. Badger, 2020: Drought less predictable under declining future snowpack. *Nat. Clim. Chang.*, **10**, 452–458, doi:10.1038/s41558-020-0754-8.

Loikith, P. C., D. E. Waliser, J. Kim, and R. Ferraro, 2018: Evaluation of cool season precipitation event characteristics over the Northeast US in a suite of downscaled climate model hindcasts. *Clim. Dyn.*, doi:10.1007/s00382-017-3837-0.

Van Loon, A. F., 2015: Hydrological drought explained. *WIREs Water*, **2**, 359–392, doi:10.1002/wat2.1085.

Maraun, D., and Coauthors, 2010: Precipitation downscaling under climate change: Recent developements to bridge the gap between dynamical models and the end user. *Rev. Geophys.*, **48**, 1–38, doi:10.1029/2009RG000314.1.INTRODUCTION.

Mass, C., D. Ovens, K. Westrick, and B. Colle, 2002: Does increasing horizontal resolution produce more skillful forecast? *Bull. Am. Meteorol. Soc.*, 407–430, doi:10.1175/1520-0477(2002)083.

McKee, T. B., N. J. Doesken, and J. Kleist, 1993: The relationship of drought frequency and duration to time scales. *Eighth Conference on Applied Climatology*, 17-22 January, Anaheim, CA, American Meterological Society, 179–183.

Mearns, L., and N. Team, 2009: The North American Regional Climate Change Assessment Program (NARCCAP): Overview of Phase II results. *IOP Conf. Ser. Earth Environ. Sci.*, **6**, 022007, doi:10.1088/1755-1307/6/2/022007.

Misra, V., S. M. DiNapoli, and S. Bastola, 2013: Dynamic downscaling of the twentieth-century reanalysis over the southeastern United States. *Reg. Environ. Chang.*, **13**, 15–23, doi:10.1007/s10113-012-0372-8.

Mo, K. C., and D. P. Lettenmaier, 2015: Heat wave flash droughts in decline. *Geophys. Res. Lett.*, **42**, 2823–2829, doi:10.1002/2015GL064018.

——, and ——, 2016: Precipitation deficit flash droughts over the United States. *J. Hydrometeorol.*, **17**, 1169–1184, doi:10.1175/JHM-D-15-0158.1.

Moon, H., B. P. Guillod, L. Gudmundsson, and S. I. Seneviratne, 2019: Soil Moisture Effects on Afternoon Precipitation Occurrence in Current Climate Models. *Geophys. Res. Lett.*, **46**, 1861–1869, doi:10.1029/2018GL080879.

Otkin, J. A., M. C. Anderson, C. Hain, I. E. Mladenova, J. B. Basara, and M. Svoboda, 2013: Examining rapid onset drought development using the thermal infrared-based evaporative stress index. *J. Hydrometeorol.*, **14**, 1057–1074, doi:10.1175/JHM-D-12-0144.1.

Palmer, W. C., 1965: Meteorological Drought. *U.S. Weather Bur. Res. Pap. No. 45*, 58.

Park, C., and Coauthors, 2016: Evaluation of multiple regional climate models for summer climate extremes over East Asia. *Clim. Dyn.*, **46**, 2469–2486, doi:10.1007/s00382-015-2713-z.

Park, S., and C. S. Bretherton, 2009: The University of Washington shallow convection and moist turbulence schemes and their impact on climate simulations with the community atmosphere model. *J. Clim.*, **22**, 3449–3469, doi:10.1175/2008JCLI2557.1.

Parker, M. D., and R. H. Johnson, 2000: Organizational Modes of Midlatitude Mesoscale Convective Systems. *Mon. Weather Rev.*, **128**, 3413–3436, doi:10.1175/1520-0493(2001)129<3413:OMOMMC>2.0.CO;2.

Pei, L., N. Moore, S. Zhong, L. Luo, D. W. Hyndman, W. E. Heilman, and Z. Gao, 2014: WRF model sensitivity to land surface model and cumulus parameterization under short-term climate extremes over the Southern great plains of the United States. *J. Clim.*, **27**, 7703–7724, doi:10.1175/JCLI-D-14-00015.1.

Peters-Lidard, C. D., and Coauthors, 2015: Integrated modeling of aerosol, cloud, precipitation and land processes at satellite-resolved scales. *Environ. Model. Softw.*, **67**, 149–159, doi:10.1016/j.envsoft.2015.01.007.

Peters, J. M., and R. S. Schumacher, 2014: Objective categorization of heavy-rain-producing MCS synoptic types by rotated principal component analysis. *Mon. Weather Rev.*, **142**, 1716–1737, doi:10.1175/MWR-D-13-00295.1.

——, and ——, 2015: Mechanisms for organization and echo training in a flash-flood-producing mesoscale convective system. *Mon. Weather Rev.*, **143**, 1058–1085, doi:10.1175/MWR-D-14-00070.1.

Phillips, T. J., and S. A. Klein, 2014: Land-atmosphere coupling manifested in warm-season observations on the U.S. southern great plains. *J. Geophys. Res. Atmos.*, **119**, 509–528, doi:10.1002/2013JD020492.

Prein, A. F., and Coauthors, 2015: A review on regional convection-permitting climate modeling: Demonstrations, prospects, and challenges. *Rev. Geophys.*, **53**, 323–361, doi:10.1002/2014RG000475.

Prein, A. F., and Coauthors, 2016: Precipitation in the EURO-CORDEX 0.11° and 0.44° simulations: high resolution, high benefits? *Clim. Dyn.*, **46**, 383–412, doi:10.1007/s00382-015-2589-y.

Roundy, J. K., and J. A. Santanello, 2017: Utility of Satellite Remote Sensing for Land–Atmosphere Coupling and Drought Metrics. *J. Hydrometeorol.*, **18**, 863–877, doi:10.1175/JHM-D-16-0171.1.

De Sales, F., and Y. Xue, 2011: Assessing the dynamic-downscaling ability over South America using the intensity-scale verification technique. *Int. J. Climatol.*, **31**, 1205–1221, doi:10.1002/joc.2139.

Santanello, J. A., and Coauthors, 2018: Land-atmosphere interactions the LoCo perspective. *Bull. Am. Meteorol. Soc.*, **99**, 1253–1272, doi:10.1175/BAMS-D-17-0001.1.

Schumacher, R. S., and R. H. Johnson, 2005: Organization and Environmental Properties of Extreme-Rain-Producing Mesoscale Convective Systems. *Mon. Weather Rev.*, **133**, 961–976, doi:10.1175/MWR2899.1.

Seneviratne, S. I., and Coauthors, 2021: Weather and Climate Extreme Events in a Changing Climate. In Climate Change 2021: The Physical Science Basis. Contribution of Working Group I to the Sixth Assessment Report of the Intergovernmental Panel on Climate Change. Masson-Delmotte et al., Eds., Cambridge University Press, Cambridge, United Kingdom and New York, NY, USA.

Skamarock, W. C., and Coauthors, 2008: A Description of the Advanced Research WRF Version 3. *Tech. Rep.*, 113, doi:10.5065/D68S4MVH.

Song, H.-J., C. R. Ferguson, and J. K. Roundy, 2016: Land–Atmosphere Coupling at the Southern Great Plains Atmospheric Radiation Measurement (ARM) Field Site and Its Role in Anomalous Afternoon Peak Precipitation. *J. Hydrometeorol.*, **17**, 541–556, doi:10.1175/JHM-D-15-0045.1.

Von Storch, H., H. Langenberg, and F. Feser, 2000: A spectral nudging technique for dynamical downscaling purposes. *Mon. Weather Rev.*, **128**, 3664–3673, doi:10.1175/1520-0493(2000)128<3664:ASNTFD>2.0.CO;2.

Svoboda, M., and Coauthors, 2002: THE DROUGHT MONITOR. *Bull. Am. Meteorol. Soc.*, **83**, 1181–1190, doi:10.1175/1520-0477-83.8.1181.

Tao, W.-K., D. Wu, S. Lang, J.-D. Chern, C. Peters-Lidard, A. Fridlind, and T. Matsui, 2016: High-resolution NU-WRF simulations of a deep convective-precipitation system during MC3E: Further improvements and comparisons between Goddard microphysics schemes and observations. *J. Geophys. Res. Atmos.*, **121**, 1278–1305, doi:10.1002/2015JD023986.

Taylor, C. M., D. Jeu, a. M. Richard, F. Guichard, P. P. Harris, and W. a. Dorigo, 2012: Afternoon rain more likely over drier soils. *Nature*, **489**, 423–426, doi:10.1038/nature11377.

Taylor, K. E., 2001: Summarizing multiple aspects of model performance in a Single Diagram. *J. Geophys. Res.*, **106**, 7183–7192, doi:10.1029/2000JD900719.

Tian, B., and Coauthors, 2017a: Development of a Model Performance Metric and Its Application to Assess Summer Precipitation over the U.S. Great Plains in Downscaled Climate Simulations. *J. Hydrometeorol.*, **18**, 2781–2799, doi:10.1175/JHM-D-17-0045.1.

Tian, D., E. Wood, and X. Yuan, 2017b: CFSv2-based sub-seasonal precipitation and temperature forecast skill over the contiguous United States. *Hydrol. Earth Syst. Sci.*, **21**, 1477–1490, doi:10.5194/hess-21-1477-2017.

Torma, C., F. Giorgi, and E. Coppola, 2015: Added value of regional climate modeling over areas characterized by complex terrain-Precipitation over the Alps. *J. Geophys. Res. Atmos.*, **120**, 3957–3972, doi:10.1002/2014JD022781.

Tripathi, O. P., and F. Dominguez, 2013: Effects of spatial resolution in the simulation of daily and subdaily precipitation in the southwestern US. *J. Geophys. Res. Atmos.*, **118**, 7591–7605, doi:10.1002/jgrd.50590.

Vicente-Serrano, S. M., S. Beguería, and J. I. López-Moreno, 2010: A multiscalar drought index sensitive to global warming: The standardized precipitation evapotranspiration index. *J. Clim.*, **23**, 1696–1718, doi:10.1175/2009JCLI2909.1.

Waldron, K. M., J. Paegle, and J. D. Horel, 1996: Sensitivity of a Spectrally Filtered and Nudged Limited-Area Model to Outer Model Options. *Mon. Weather Rev.*, **124**, 529–547, doi:10.1175/1520-0493(1996)124<0529:SOASFA>2.0.CO;2.

Wang, S. Y., and T. C. Chen, 2009: The late-spring maximum of rainfall over the U.S. central plains and the role of the low-level jet. *J. Clim.*, **22**, 4696–4709, doi:10.1175/2009JCLI2719.1.

Wang, W., and N. L. Seaman, 1997: A Comparison Study of Convective Parameterization Schemes in a Mesoscale Model. *Mon. Weather Rev.*, **125**, 252–278, doi:10.1175/1520-0493(1997)125<0252:ACSOCP>2.0.CO;2.

Wei, J., H. Su, and Z. L. Yang, 2016: Impact of moisture flux convergence and soil moisture on precipitation: a case study for the southern United States with implications for the globe. *Clim. Dyn.*, **46**, 467–481, doi:10.1007/s00382-015-2593-2.

Welty, J., and X. Zeng, 2018: Does Soil Moisture Affect Warm Season Precipitation Over the Southern Great Plains? *Geophys. Res. Lett.*, **45**, 7866–7873, doi:10.1029/2018GL078598.

Whiteman, C. D., X. Bian, and S. Zhong, 1997: Low-level jet climatology from enhanced rawinsonde observations at a site in the southern Great Plains. *J. Appl. Meteorol.*, **36**, 1363–1376, doi:10.1175/1520-0450(1997)036<1363:LLJCFE>2.0.CO;2.

Wilks, D. S., 2011: *Statistical methods in the atmospheric sciences*. Third edit. Academic Press,.

Williams, I. N., 2019: Evaluating Soil Moisture Feedback on Convective Triggering: Roles of Convective and Land-Model Parameterizations. *J. Geophys. Res. Atmos.*, **124**, 317–332, doi:10.1029/2018JD029326.

Wootten, A., J. H. Bowden, R. Boyles, and A. Terando, 2016: The sensitivity of WRF downscaled precipitation in puerto rico to cumulus parameterization and interior grid nudging. *J. Appl. Meteorol. Climatol.*, **55**, 2263–2281, doi:10.1175/JAMC-D-16-0121.1.

Xu, K.-M., and D. A. Randall, 1996: A Semiempirical Cloudiness Parameterization for Use in Climate Models. *J. Atmos. Sci.*, **53**, 3084–3102, doi:10.1175/1520-0469(1996)053<3084:ASCPFU>2.0.CO;2.

Yang, Q., R. A. Houze, L. R. Leung, and Z. Feng, 2017: Environments of Long-Lived Mesoscale Convective Systems Over the Central United States in Convection Permitting Climate Simulations. *J. Geophys. Res. Atmos.*, **122**, 13,288-13,307, doi:10.1002/2017JD027033.

Yu, X., and T. Y. Lee, 2010: Role of convective parameterization in simulations of a convection band at grey-zone resolutions. *Tellus, Ser. A Dyn. Meteorol. Oceanogr.*, **62**, 617–632, doi:10.1111/j.1600-0870.2010.00470.x.

Zhang, F., Y. Qiang Sun, L. Magnusson, R. Buizza, S. J. Lin, J. H. Chen, and K. Emanuel, 2019: What is the predictability limit of midlatitude weather? *J. Atmos. Sci.*, **76**, 1077–1091, doi:10.1175/JAS-D-18-0269.1.

Zhang, Y., J. K. Roundy, and J. A. Santanello, 2021: Evaluating the impact of model resolutions and cumulus parameterization on precipitation in NU-WRF: A case study in the Central Great Plains. *Environ. Model. Softw.*, **145**, 105184, doi:10.1016/j.envsoft.2021.105184.

Zheng, Y., K. Alapaty, J. A. Herwehe, A. D. Del Genio, and D. Niyogi, 2016: Improving High-Resolution Weather Forecasts Using the Weather Research and Forecasting (WRF) Model with an Updated Kain–Fritsch Scheme. *Mon. Weather Rev.*, **144**, 833–860, doi:10.1175/MWR-D-15-0005.1.

Zhou, Y., D. Wu, W. K.-M. Lau, and W.-K. Tao, 2016: Scale Dependence of Land–Atmosphere Interactions in Wet and Dry Regions as Simulated with NU-WRF over the Southwestern and South-Central United States. *J. Hydrometeorol.*, **17**, 2121–2136, doi:10.1175/JHM-D-16-0024.1.